Advancing the BRAMS wildfire–atmosphere modelling system: application to an extreme wildfire event

Isilda Cunha Menezes[1], Luiz Flávio Rodrigues[2], Karla M. Longo[2], Mateus Ferreira e Freitas[3], Saulo R. Freitas[2], Rodrigo Braz[2], Valter Ferreira de Oliveira[4], Sílvia Coelho[1], Ana Isabel Miranda[1]

[1]Center for Environmental and Marine Studies (CESAM), Department of Environment and Planning, University of Aveiro, Campus Universitário de Santiago, 3810-193 Aveiro, Portugal.
[2]Center for Weather Forecasting and Climate Studies (CPTEC), Department of Physics, National Institute for Space Research, Cachoeira Paulista, SP, Brazil.
[3]Multiuser Laboratory of High Performance Computing (LaMCAD), UFG Innovation Agency Building, Federal University of Goiás (UFG), Samambaia Campus, 74690-631, Goiânia, GO, Brazil.
[4]Finatec, Brasília-DF, Campus Darcy Ribeiro, Brazil.

Correspondence to: Isilda C. Menezes (isildacm@ua.pt), Saulo R. Freitas (saulo.r.de.freitas@gmail.com)

Abstract. Wildfire smoke significantly perturbs atmospheric composition and radiative balance, with implications for air quality, weather, and climate. Accurately simulating smoke–radiation–convection interactions remains a scientific challenge, particularly at meso-local scales. This study presents developments in the BRAMS v6.0 modelling system, including the integration of crown fire spread into SFIRE and dynamic coupling of fire-emitted smoke fluxes. These enhancements enable physically consistent simulations of wildfire behaviour, smoke emissions, and their radiative impacts.

The model couples fire spread and heat release to compute Fire Radiative Power, which drives smoke emissions in real time. These emissions are fully integrated with aerosol–radiation interactions and atmospheric dynamics. The system was applied to the 15 October 2017 wildfire in central Portugal using high-resolution simulations.

Model performance was evaluated by comparing a diagnostic Smoke Optical Depth, computed offline from BRAMS-simulated PM2.5 using a Mie-based framework, against MERRA-2 Aerosol Optical Depth. The SOD fields reproduced the main spatial and temporal patterns of smoke transport and the wavelength-dependent optical behaviour, including extinction and absorption at 400, 550, and 700 nm.

Statistical comparison confirmed a physically consistent agreement between simulated smoke optical depth (SOD) and satellite AOD, particularly during the active fire phase. Extinction reached 67 m^{-1} at 400 nm, while absorption peaked near 5 m^{-1} at 550 nm, revealing the dominant role of organic carbon in visible-range scattering and of black carbon in shortwave absorption. Radiative heating within the plume induced upward displacements of the CIN layer by 100–200 m and partial erosion of thermal inversions, forming transient radiative lids that modulated boundary-layer stability. CAPE was locally enhanced, indicating a radiative–convective feedback between smoke heating and near-surface buoyancy. These results demonstrate that the enhanced BRAMS model can realistically capture coupled fire–atmosphere–radiation processes at high resolution,

improving both the interpretation and prediction of smoke-induced thermodynamic and radiative perturbations over complex terrain.

Graphical Abstracts.

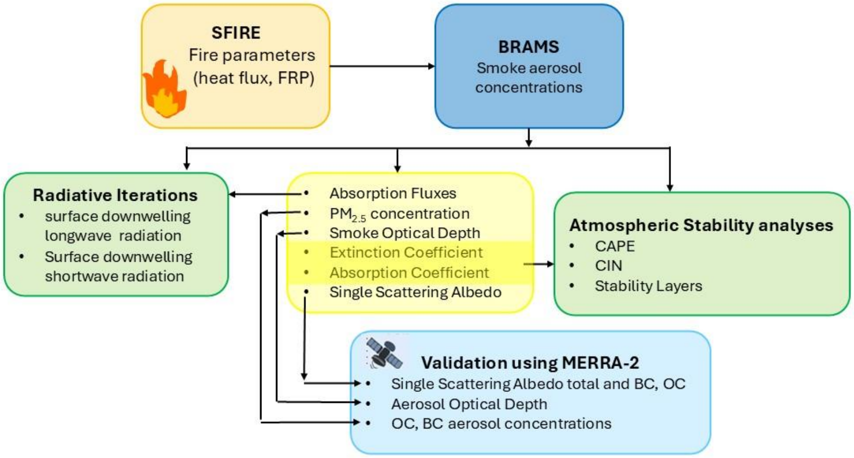

1 Introduction

Understanding wildfire emissions is essential for accurately predicting air quality (Fernandes et al., 2022) and radiative impacts, particularly in complex terrains where smoke dispersion is strongly influenced by local meteorological dynamics. Recent European case studies have shown severe urban air-quality degradation during major wildfire episodes, including the August 2021 Athens fires (Osswald et al., 2023) and the October 2017 north centre of Portugal wildfires (Lopes et al., 2023). Wildfires release large quantities of trace gases and aerosols that interact with atmospheric chemistry (Andreae et al., 2001; Jaffe et al., 2008; Monks et al., 2012), modulate radiative transfer (Clinton et al., 2006; Menezes et al., 2024), reduce visibility (Valente et al., 2007), and severely affect human health (Apte et al., 2018; Lopes et al., 2024; Miranda et al., 2010). These impacts further highlight the growing importance of high-resolution, community-based air-quality monitoring and citizen engagement initiatives (Relvas et al., 2025), which complement modelling and satellite approaches by improving local understanding and response capacity during wildfire events. These challenges are especially difficult to quantify under the rapidly changing conditions typical of wildfire episodes, requiring dynamic models capable of resolving fire–atmosphere feedback at high spatial and temporal resolutions.

Traditional approaches for estimating biomass-burning emissions in operational air-quality and climate models often rely on semi-empirical methods, including precompiled inventories such as the Global Fire Emissions Database (GFED) and satellite-derived Fire Radiative Power (FRP) products assimilated in systems like the Copernicus Atmosphere Monitoring Service – Global Fire Assimilation System (CAMS-GFAS) (CAMS (2015)). While these frameworks provide valuable large-scale emission estimates, their relatively coarse spatial resolution and simplified fire parameterizations limit their ability to capture the rapid evolution and spatial heterogeneity of active wildfires. This limitation is particularly critical in forested regions, where intense crown fires coexist with patchy surface burning and smouldering phases. As demonstrated by Oliveira et al. (2025), coarse FRP retrievals often miss or underestimate localized high-intensity combustion in complex terrain, introducing systematic biases in both the magnitude and timing of smoke emissions. While computationally efficient, these methods do not simulate fire spread or associated heat release, limiting their capacity to resolve the dynamic feedbacks that modulate local atmospheric stability and pollutant dispersion. The Brazilian Biomass Burning Emission Model (3BEM (Freitas et al (2009); Longo et al. (2010)) coupled to BRAMS (Brazilian Regional Atmospheric Modeling System) follows this approach, estimating smoke emissions based on FRP, surface type, and meteorology, but without explicit coupling to fire dynamics. This framework is suitable for regional or long-term assessments but lacks physical consistency under rapidly evolving fire conditions.

Wildland fire behaviour models developed historically within the forestry community have been primarily designed to predict two-dimensional surface fire spread rates and heat release under prescribed fuel types, slope conditions and wind fields, with a primary focus on fire danger assessment and surface fire behaviour. These operationally oriented semi-empirical models are not intended to resolve highly dynamic or plume-driven fire behaviour, nor the onset of extreme fire development beyond the incipient stage.

Fully coupled atmosphere–surface fire models, such as WRF-SFIRE (Mandel et al., 2011), CAWFE (Clark et al., 1996; Coen, 2005), or BRAMS-SFIRE (Menezes et al., 2021) and ForeFire/Meso-NH (Filippi et al., 2013), integrate a mesoscale non-hydrostatic, large-eddy numerical weather prediction core with a semi-empirical fire surface spread module (typically based on Rothermel (1972), and McArthur (1967)). In such systems, the fire and atmosphere evolve as a single dynamically coupled entity, allowing simulation of small-scale fire–atmosphere interactions, vorticity-driven dynamics, fire-induced buoyancy, and turbulence feedback. These models explicitly represent fire-generated kinetic and potential energy via resolved sensible and latent heat fluxes, and predict fire perimeter evolution, fuel consumption, fireline intensities, and rate of spread. Model initialization requires fuel load and fuel moisture content, fuel burn rate, combustion heat release, and treatment of canopy ignition when heat flux exceeds a critical threshold, in addition to terrain and local wind forcing.

Smoke aerosols strongly perturb the atmospheric energy balance through wavelength-dependent scattering and absorption, governed by their size distribution, complex refractive index, mixing state and ageing (Pueschel et al., 1988; Reid et al., 2005). These properties determine aerosol optical depth (AOD), single-scattering albedo and vertical extinction structure, thereby influencing surface heating, atmospheric stability and fire–atmosphere feedback. Curci et al. (2015) showed that neglecting aerosol mixing state can alter simulated AOD by more than a factor of two for identical aerosol mass, emphasising the need for physically based optical treatments in coupled fire–atmosphere systems. Regional studies have documented wide variability in smoke optical behaviour. Procopio et al. (2003) analysed AERONET observations over Brazil using Mie theory and validated a radiative forcing model across multiple optical thickness regimes and wavelengths. Reid and Hobbs (1998) found that Brazilian smoke exhibits about 15 % lower scattering coefficients and reduced single-scattering albedo relative to North American fires, attributed to combustion efficiency differences. Reid et al. (1999) further reported pronounced temporal variability in AOD over diurnal and multi-day cycles. Yumimoto et al. (2018) demonstrated that assimilating Himawari-8 aerosol observations improves the representation of Siberian smoke transport, correcting emission underestimations and capturing the distinctive C-shaped dispersion pattern over Japan. Finally, Ferrare et al. (1990) using NOAA-7 AVHRR data, characterized large-scale smoke transport from Canadian forest fires, with optical thickness ranging from < 0.1 to > 3.7, particle radii of 0.3–0.9 µm, and lifetimes of 15–20 days, evidence of persistent, long-range smoke layers influencing regional radiative forcing. Makar et al. (2021) additionally demonstrated that wildfire smoke can cool the surface and stabilise the lower troposphere, altering plume dynamics and atmospheric circulation.

Recent advances in operational smoke forecasting systems, such as the HRRR-Smoke model (Ahmadov, 2017; Ye et al., 2021), have improved the coupling between fire activity, emissions, and atmospheric transport. Similar developments in regional and global frameworks (Anderson et al., 2024; Kochanski et al., 2021; Kochanski et al., 2015) have enhanced the representation of plume rise, aerosol–radiation interactions, and smoke dispersion. However, these systems generally rely on semi-empirical plume-injection schemes and parameterized fire emissions, without resolving crown-fire propagation or the thermodynamic feedbacks associated with combustion heat release. Fully physically coupled fire–atmosphere models capable of simultaneously representing fuel consumption, surface- and canopy-fire spread, heat fluxes, and the resulting smoke optical effects remain rare in European wildfire contexts, particularly in complex mountainous terrain.

Addressing this gap, the present study employs a BRAMS–SFIRE configuration that explicitly resolves both surface and crown fire propagation and dynamically couples sensible and latent heat release to plume rise and vertical smoke transport. The main purpose of this paper is to describe the improvements implemented in the BRAMS-SFIRE (Freitas et al., 2017; Menezes et al., 2021; Menezes, 2015) modelling system to enhance the physical realism of wildfire representation beyond surface-fire-only approaches, by including an explicit crown–fire propagation scheme. With this explicit treatment of crown-fire propagation, the model is expected to generate a more physically consistent smoke plume evolution, particularly under high-intensity fire conditions. By resolving fire–atmosphere interactions at fine spatial scales, the resulting smoke injection height, plume structure, and downwind dispersion are anticipated to more closely resemble observed plume behaviour, thereby improving the realism of high-resolution wildfire smoke simulations. Moreover, this integration enables simulations that explicitly resolve surface and canopy fire spread, fuel consumption, and the associated release of heat and smoke over heterogeneous terrain. Fire Radiative Power (FRP) is not prescribed but internally computed from model-resolved sensible heat fluxes, allowing smoke emissions to evolve dynamically with fire intensity and meteorological conditions. The two-way coupling supports feedback between combustion processes and local thermodynamics, which are critical for reproducing vertical smoke transport and smoke–radiation–convection interactions.

Compared to the WRF-SFIRE system (Allen et al., 2021; Kochanski et al., 2021; Mandel et al., 2014; Mandel et al., 2011), BRAMS shares a similar physical coupling architecture for simulating surface fire–atmosphere interactions. BRAMS originated from the RAMS model, a globally applicable mesoscale model initially developed in the United States. Over time, RAMS was adapted with physical parameterizations better suited to represent processes relevant to tropical regions, leading to the development of BRAMS.

BRAMS has been extensively applied in South America, it remains a versatile model capable of simulating atmospheric processes across a wide range of latitudes, from tropical to mid-latitude conditions, in both hemispheres. The main differences between BRAMS and WRF lie in their physical parameterizations, vertical coordinate systems, and the way they resolve the atmospheric base state. These structural differences influence how each model represents radiation, microphysics, turbulence, and surface–atmosphere interactions, particularly under conditions of strong vertical development such as those driven by wildfires. The improved modelling system was tested through its application to the Sertã extreme wildfire of 15 October 2017 in central Portugal (Menezes et al., 2024). The event occurred in a mountainous region with strong mountain–valley circulations, which strongly modulate smoke dispersion and vertical mixing, providing a demanding yet scientifically valuable testbed for model evaluation.

Section 2 describes the modelling developments and experimental design, including the treatment of crown-fire initiation and vertical injection of emissions. Section 3 presents the simulated fire-spread behaviour, plume injection heights, PM2.5 loadings and the resulting radiative and thermodynamic impacts, highlighting the value of fully two-way fire–atmosphere coupling for advancing understanding of wildfire-induced air-quality degradation and atmospheric feedback processes.

2 Methodology

This section details the advancements made in the BRAMS model, including the integration of a crown fire spread behaviour model and the implementation of FRP calculations within SFIRE. The processes for assimilating National Fuel Fire Laboratory (NFFL) fuel behaviour models and high-resolution terrain elevation data are also described, ensuring accurate nesting of the SFIRE grid within the BRAMS grid for two-way coupling of wildfire fluxes and emissions. Furthermore, the methodology used to characterize particulate matter with an equivalent diameter less than 2.5 µm (PM2.5) released during the Sertã wildfire episode on 15 October 2017, as simulated by BRAMS, is thoroughly explained. This includes the validation and interaction of smoke with atmospheric radiation, as well as the specification of surface conditions required by SFIRE simulation. For a better understanding of the improvements that have been made, the section starts with a description of the original BRAMS-SFIRE modelling system.

2.1 The BRAMS-SFIRE modelling system

2.1.1 The BRAMS model

The BRAMS is based on the Regional Atmospheric Modeling System (RAMS) developed at Colorado State University (CSU/USA). It is free software (CC-GPL), maintained by Centre for Weather Forecasting and Climate Studies from National Institute for Space Research (CPTEC/INPE), University of São Paulo (USP), and other institutions in Brazil and abroad.

BRAMS and RAMS are versatile numerical weather prediction models, capable of simulating atmospheric circulations across a wide range of scales, from hemispheric to large eddy simulations (LES) of the planetary boundary layer. Significant improvements have been made to BRAMS to better represent key physical processes in tropical and subtropical regions, alongside integrated atmospheric chemistry and aerosol processes. It also includes a state-of-the-art model for simulating the exchange of water, energy, momentum, and biogeochemical tracers between the atmosphere and the surface (Freitas et al., 2017). BRAMS solves the compressible, non-hydrostatic atmospheric equations described by Tripoli and Cotton (1982). It uses a one-way nesting scheme to perform downscaling on computational grids with increasing spatial resolution (Freitas et al., 2017).

Additionally, BRAMS incorporates a real-time assimilation method for the CCATT, focusing on the assimilation of trace gas and aerosol emissions from biomass burning, using FRP data derived from MODIS and GOES satellite products (Pereira et al., 2022; Pereira, 2013). Although the model typically underestimates emissions by up to 25%, it successfully captures around 90% of biomass burning activity, demonstrating high potential for near real-time monitoring of gases and aerosols emitted during biomass combustion. The FRP-based method improves emission estimations by 25% compared to traditional methods, accurately capturing regional and local biomass burning patterns (Pereira, 2013).

2.1.2 The surface fire model (SFIRE)

A detailed description of the SFIRE surface-fire module, including its ignition strategy, level-set front propagation, fuel-consumption algorithms and coupling to atmospheric forcing, was originally documented in Annex C of Isilda (2015). For completeness and clarity, we provide here a concise summary of the key elements relevant to the present study.

2.1.2.1 Ignition and initial conditions

SFIRE initializes combustion from a user-specified point or line ignition. To avoid singular behavior at $t = t_0$ and to seed a finite front, the code creates an initial burned kernel (small disc/segment) around the ignition locus. The advancing fireline is represented by a level-set function $\psi(x,t)$, with $\psi < 0$ inside the burning region, $\psi = 0$ at the fireline, and $\psi > 0$ outside.

2.1.2.2 Front kinematics via level sets

The fireline evolves according to a Hamilton–Jacobi equation:

$$\frac{\partial\psi}{\partial t} + R(x,t)\|\nabla\psi\| = 0 \tag{1}$$

where R is the local rate of spread (ROS, m s^{-1}) evaluated along the outward normal to the front. Time stepping uses a two-stage Heun (second-order Runge–Kutta) scheme. Spatial derivatives are computed with upwind-consistent reconstructions (standard upwind, Godunov, ENO, or Sethian formulations), which preserve the correct upwind direction and suppress spurious oscillations. Standard reinitialization keeps ψ close to a signed-distance function, stabilizing $\|\nabla\psi\|$. At grid scale, a cell transitions to burning when ψ changes sign within the cell; hence propagation between cells is governed by the zero-crossing of ψ, not by explicit geometric "jumps".

2.1.2.3 Rate of spread and directional dependence

In the default configuration, the no-wind/no-slope ROS comes from the semi-empirical Rothermel (1972) formulation. Directional amplification by wind and slope is applied via multiplicative factors projected on the front normal. The model framework allows the user to select alternative spread formulations when appropriate for the dominant fuel type or regional fire regime. Available parameterizations include the McArthur (1966, 1967) law, commonly used for Australian forest fuels, and the Clark et al. (2004) spread formulation for chaparral and shrubland ecosystems. These options are user-defined in the configuration namelist.

2.1.2.4 Atmospheric forcing and topographic effects

The horizontal wind from the host atmosphere model is horizontally interpolated to the fire grid and vertically adjusted to mid-flame height using a logarithmic profile. Optionally, a mid-flame wind reduction factor (Baughman and Albini, 1980) is applied, conditioned on the fuel category, to represent drag within the fuelbed. Slope enters through the local terrain gradient projected onto the propagation direction, providing the Rothermel (1972) slope factor.

2.1.2.5 Fuel consumption and heat release

Each fire-grid cell carries a non-dimensional available-fuel fraction $F \in [0,1]$ that decays after ignition according to the cell's flame residence time and fuel moisture. Two consistent algorithms compute within-cell fuel loss using bilinear interpolation of ψ and ignition time at cell vertices/edges: (i) a fast algebraic approximation and (ii) a more accurate quadrature/least-squares method for partially burning cells (Fig. 1). Sensible and latent heat fluxes (W m^{-2}) are then diagnosed from the burning rate and fuel properties and coupled back to the atmosphere.

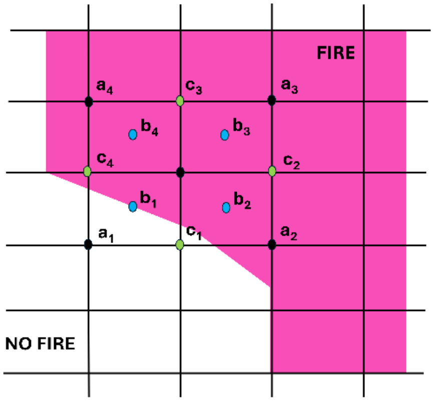

Figure 1: Schematic of fire-front propagation on the fire mesh. Black markers denote the high-resolution fire grid where the level-set function ψ and the burn time τ are advanced. Blue markers indicate bilinear interpolation of ψ and τ to the cell-center vertices using a four-point stencil. Green markers indicate bilinear interpolation of ψ and τ to the midpoints of each cell edge using a 1-D edge stencil. These interpolated values drive the fuel-consumption update (remaining-fuel calculation) at sub-cell locations. The magenta area marks cells classified as FIRE, while the white area corresponds to NO FIRE.

2.1.2.6 Fuel-moisture diagnosis

Fuel moisture responds to ambient humidity, temperature, and precipitation using established wetting/drying laws (after Van Wagner and successors), with appropriate lags for different timelag classes. Atmospheric scalars are interpolated from the host grid to the fire grid with distance-weighted schemes; precipitation and relative humidity modulate both consumption and diagnosed heat fluxes.

2.1.2.7 Why grid resolution matters and what we mean by "overpropagation."

Let Δx be the fire-grid spacing and Δt the integration step used for the level-set update. The distance a front element advances in one step is $d \approx R\Delta t$. If d becomes comparable to or exceeds Δx anywhere on the mesh, the front can traverse multiple cells in a single update, producing a numerically accelerated spread that is not physically warranted by the resolved fields. We refer to this violation of the fire-CFL condition: $R\Delta t \lesssim c\Delta x \quad (0 < c \leq 1)$ as overpropagation. The risk increases (i) when a coarse Δx is advanced with too large a Δt (e.g., if fire is stepped only at the atmospheric time step), and (ii) locally where R spikes due to strong winds projected at mid-flame height or steep terrain slopes (especially if wind reduction or terrain resolution are not consistent with the fire grid).

2.1.2.8 Numerical and physical controls to avoid overpropagation

SFIRE employs several safeguards:

- temporal subcycling of the fire solver. Within each atmospheric step, the level-set is advanced with one or more fire substeps Δt_{fire} chosen to satisfy $R\Delta t_{fire} \leq c\Delta x$ across the grid.
- Physically plausible ROS caps. Upper bounds on R per fuel type and environmental state prevent unrealistically large local advances (e.g., under transient gusts or extreme slopes).
- Level-set reinitialization. Periodic signed-distance reinitialization stabilizes $\|\nabla\psi\|$ and the speed function.
- Consistent forcing. Application of mid-flame wind reduction factors and the use of terrain data at a resolution commensurate with the fire grid mitigate artificial inflation of the wind and slope multipliers.
- Realistic ignition seeding. A finite initial burned kernel aligned with observed perimeters avoids spuriously rapid early-time expansion from a point-like ignition on coarse meshes.

Together, these measures keep front advancement physically consistent across grid sizes and explain why resolution-aware tuning (choice of subcycling, ROS caps, and forcing options) is necessary and justified.

2.1.3 BRAMS-SFIRE interface integration

BRAMS was coupled with the SFIRE model to simulate atmosphere and fire interactions (Menezes et al., 2021). The communication between the BRAMS model and the SFIRE model is facilitated through an interface program. In this process, variables from BRAMS related to the basic state of the atmosphere are assimilated through this interface with SFIRE. These variables include surface pressure, air moisture at 2 m, air temperature at 2 m, zonal and meridional wind components at the lowest vertical model levels, geopotential height, air density, microphysics, vegetation cover (including roughness and vegetation type), and heat fluxes.

When SFIRE is called for the first-time step, the driver initializes SFIRE model by reading SFIRE's parameters from a name list, configuring flags, and setting the grid spacing. The high-resolution SFIRE domain is then integrated into the BRAMS model domain by creating a grid centred on the ignition points, with a radius that encompasses the area predicted to be burned by the fire. Detailed input on fuel behaviour models and terrain height at high resolution must be provided, which are then read and interpolated onto the SFIRE grid domain. After the ignition time, SFIRE injects sensible and latent heat fluxes, along with FRP, into BRAMS, explicitly forcing the atmospheric energy and thermodynamic fields and driving the production and transport of smoke-related aerosol mass. These heat fluxes are directly coupled to the BRAMS turbulence and boundary-layer parameterizations, ensuring dynamic consistency in the representation of fire-induced buoyancy and energy transfer within the atmospheric column.

The BRAMS model offers two approaches for simulating smoke pollution, (1) the dispersion of smoke particulate matter derived from FRP, simulated by SFIRE and used as a passive tracer for atmospheric transport; and (2) a chemistry-coupled approach that integrates smoke particulate matter from SFIRE with emissions from the Biomass Burning Emission Model (3BEM), anthropogenic and biogenic inventories, and analysis data from the Copernicus Atmosphere Monitoring Service (CAMS). This latter approach is implemented through the CCATT module of BRAMS, enabling more comprehensive simulations of atmospheric composition, pollutant transport, and concentration patterns. These dual methodologies enhance the model's capability to accurately represent the complex interactions between fire emissions and atmospheric chemistry.

2.1.4 Plume-rise and vertical injection of fire emissions in BRAMS

In BRAMS, fire-emitted aerosols and gases are not injected solely at the surface. Instead, the model employs an online, physically based plume-rise scheme implemented within the CCATT-BRAMS chemistry and aerosol module (Freitas et al., 2006; Freitas et al., 2007; Freitas et al., 2010). At every model timestep, the sensible heat flux released by the fire is used to diagnose the buoyant energy that drives the plume, which determines the plume-top height dynamically by applying a 1-D time-dependent cloud model. The diagnosed injection height is then projected onto the model's σ-coordinate system, and the emitted mass is vertically distributed across multiple layers, rather than being confined to a single surface level.

Accordingly, BRAMS follows a surface emission plus dynamic plume-rise approach, in which the vertical distribution of smoke is determined interactively at runtime by the evolving fire heat release (Q), atmospheric stability, and convective turbulence, rather than by any fixed or user-defined injection layer. This ensures that the injection height and profile evolve consistently with the meteorological state and the fire intensity.

As an example, Fig. 2 shows the simulated smoke column on 15 October 2017 over complex terrain, with PM2.5 lofted well above the surface. This vertical structure is generated online by the SFIRE heat fluxes and the associated FRP-derived emissions, which determine the diagnosed plume-top height before the mass is subsequently mixed and transported by the model dynamics, turbulence, and the chemistry–aerosol processes described above.

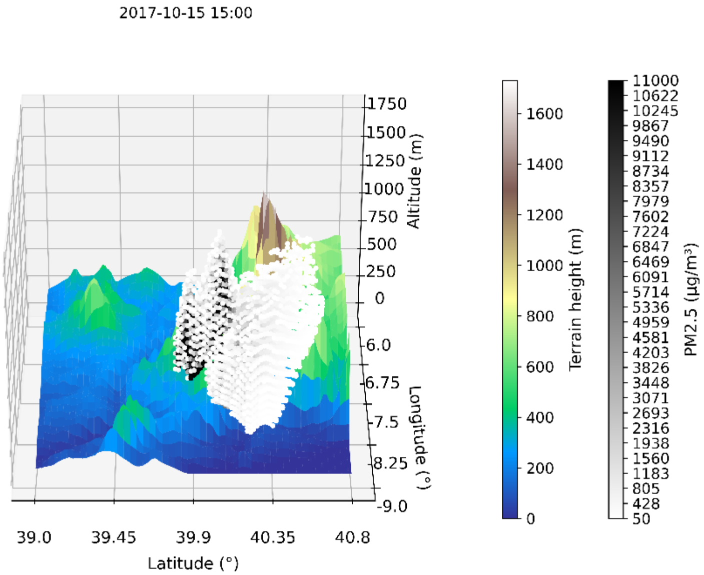

Figure 2: 3-D view of BRAMS–SFIRE smoke injection on 15 Oct 2017 (15:00 UTC); plume-top height and vertical allocation are computed online from SFIRE heat release/FRP using the CCATT-BRAMS plume-rise scheme.

2.1.5 New improvements on BRAMS-SFIRE

Several enhancements were made to this coupled BRAMS-SFIRE system. Fig. 3 schematically shows these improvements.

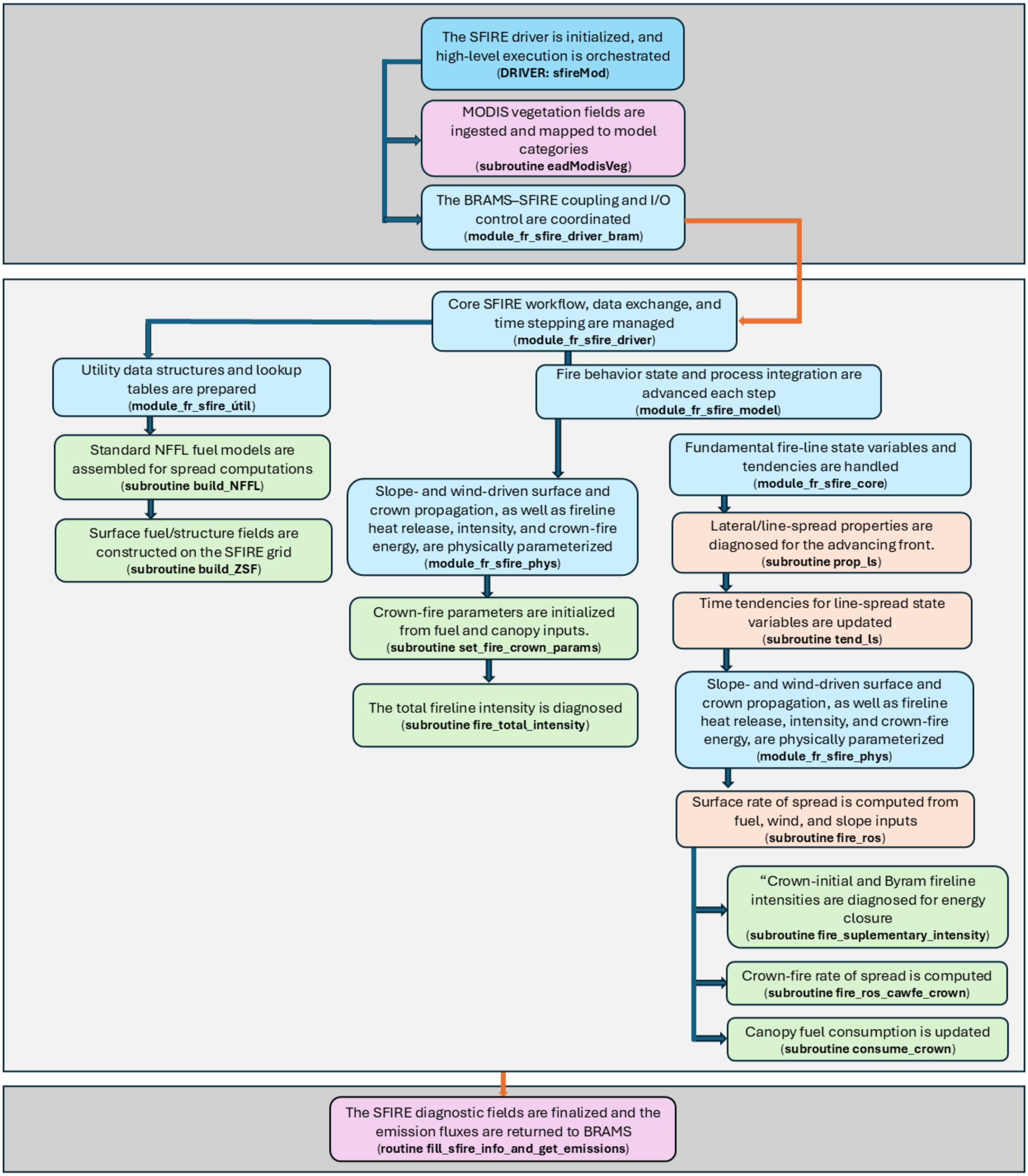
The SFIRE driver is initialized, and high-level execution is orchestrated (DRIVER: sfireMod)
MODIS vegetation fields are ingested and mapped to model categories (subroutine eadModisVeg)
The BRAMS–SFIRE coupling and I/O control are coordinated (module_fr_sfire_driver_bram)
Core SFIRE workflow, data exchange, and time stepping are managed (module_fr_sfire_driver)
Utility data structures and lookup tables are prepared (module_fr_sfire_útil)
Standard NFFL fuel models are assembled for spread computations (subroutine build_NFFL)
Surface fuel/structure fields are constructed on the SFIRE grid (subroutine build_ZSF)
Fire behavior state and process integration are advanced each step (module_fr_sfire_model)
Slope- and wind-driven surface and crown propagation, as well as fireline heat release, intensity, and crown-fire energy, are physically parameterized (module_fr_sfire_phys)
Crown-fire parameters are initialized from fuel and canopy inputs. (subroutine set_fire_crown_params)
The total fireline intensity is diagnosed (subroutine fire_total_intensity)
Fundamental fire-line state variables and tendencies are handled (module_fr_sfire_core)
Lateral/line-spread properties are diagnosed for the advancing front. (subroutine prop_ls)
Time tendencies for line-spread state variables are updated (subroutine tend_ls)
Slope- and wind-driven surface and crown propagation, as well as fireline heat release, intensity, and crown-fire energy, are physically parameterized (module_fr_sfire_phys)
Surface rate of spread is computed from fuel, wind, and slope inputs (subroutine fire_ros)
"Crown-initial and Byram fireline intensities are diagnosed for energy closure (subroutine fire_suplementary_intensity)
Crown-fire rate of spread is computed (subroutine fire_ros_cawfe_crown)
Canopy fuel consumption is updated (subroutine consume_crown)
The SFIRE diagnostic fields are finalized and the emission fluxes are returned to BRAMS (routine fill_sfire_info_and_get_emissions)

Figure 3: Diagram illustrating the structure of the SFIRE model, with newly integrated subroutines denoted in light green boxes and called within the subroutines highlighted in light orange. The light blue boxes indicate the modules where these subroutines are implemented. The light pink boxes represent the subroutines responsible for integrating the BRAMS and SFIRE models in the context of the wildfire emissions.

2.1.6 Implementation of the Crown Fire Behaviour Model

The SFIRE model (Mandel et al., 2009; Mandel et al., 2011), coupled with BRAMS (Freitas et al., 2017) by Menezes et al. (2021) and Menezes (2015), enables the analysis of surface fire behaviour, accounting for fuel bed type along with its thermal, mineral, and dendrometric characteristics, moisture content, topography, and atmospheric wind conditions. Significant improvements were made to this coupled model based on the work of Scott and Reinhardt (Scott and Reinhardt, 2001), by integrating a numerical model that predicts the spread and intensity of crown fires. This enhancement was incorporated into the SFIRE surface fire spread subroutines, as is illustrated in the scheme shown in Figure 3. The new subroutines were developed to improve the prediction of fire spread and intensity in tree canopies and to perform the interpolation of NFFL fuel behaviour models and terrain elevation onto the SFIRE grid.

In the ‘set_fire_crown_params’ subroutine, the quasi-steady rate of spread is calculated for fuel behaviour model 10, which is a standardized vegetation fuel description. This model defines the physical and chemical properties of the fuel that are essential for computing fire spread rate, intensity, and overall fire behaviour. In the 'consume_crown' subroutine, the rate of active crow fire spread and the fraction of the canopy fuels consumed are computed. To determine these parameters, the subroutine calculates the equivalent rate of spread $R_{initialization}$ (Eq. (2), concepts in Forestry Canada Fire Danger Group (1992) and Van Wagner (1977)), which depends on the critical (minimum) fireline intensity $I_{initialization}$ of the surface fire, and the heat yield of fuel release per unit area H. It is important to note that SFIRE is implemented using the International System of Units (SI).

$$R_{initialization} = \frac{60 I_{initialization}}{H} \quad (2)$$

Where 60 is a conversion factor so that the units for I reduce from kJ m^{-1} min^{-1} to kW m^{-1} , and H (Andrews and Rothermel, 1982):

$$H = I_{r_{10}} t_r \text{ (in kJ m}^{-2}\text{)} \quad (3)$$

The symbol $I_{r_{10}}$ represents the reaction intensity for NFFL fuel behaviour model 10, while t_r (Eq. (4)), represents the residence time for the same model (in minutes). The latter variable is a function of the surface-area-to-volume ratio (σ_{10}), as described below,

$$t_r = \frac{12.595}{\sigma_{10}} \tag{4}$$

The rate of active crown fire spread R_{active} (Eq. (5)), set to 40 % of the observed 6.1-meter windspeed at midflame height (Rothermel, 1991), i.e., the average height within the flaming combustion zone where wind directly influences fire behavior. This height is commonly used in fire behavior modeling for standardization, particularly in the context of surface and crown fire interactions. Active crown fire spread, varies with wind speed, but is also influenced by slope and foliar moisture content (*FMC*, measured in percent), through the foliar moisture effect (*FME*) as defined by Van Wagner (Van Wagner, 1974, 1977, 1989),

$$R_{active} = 3.34\left(\frac{FME}{FME_0}\right)(R_{10})_{40\,\%} \ \text{(in ms}^{-1}\text{)} \tag{5}$$

with,

$$FME = \frac{(1.5-0.00275FMC)^4}{460+25.9FMC} \tag{6}$$

considering the ratio of *FME* to a reference value $FME_0 = 0.0007383,$ established for a foliar moisture content (FMC) of 100 percent (Scott and Reinhardt, 2001).

Building upon the transition function concept proposed by Van Wagner (1989) that provides a scaling mechanism between surface and crown fire spread predictions, the model accounts for this process using Eq. (7).

$$R_{surface} \geq R_{initialization} + 32.8084 \ \text{(in m s}^{-1}\text{)} \tag{7}$$

CFB (Eq. (8)) is a transition function known as the crown fraction burned, representing the fraction of available canopy fuels consumed during a fire. It is used to estimate the degree of crowning (Van Wagner, 1989) and to predict the resulting spread rate in fire behaviour simulations. CFB values range from 0 for a surface fire to 1 for a fully active crown fire.

$$CFB = 1 - e^{-0.23(R_{surface}-R_{initialization})} \tag{8}$$

The ‘fire_ros’ subroutine applies criteria to determine the initiation and sustained spread of crown fires, classifying a fire as either surface fire or crown fire, without differentiating between passive and active crown fire. The approach is based on threshold criterion (Eq. (9)) involving the fireline intensity required to sustain crown fire behaviour (Classification based on Van Wagner (1977) and Alexander (1988), as described in Figure 6 of Scott and Reinhardt (2001)),

$$I_{surface} > I_{initialization} \tag{9}$$

with $I_{surface}$ representing the Byram fireline intensity which is the rate of heat release per unit length of fire front (kW m^{-1}), and $I_{initialization}$ (Van Wagner, 1977) calculated within the fire_suplementary_intensity subroutine, as defined in Eq. (10).

$$I_{initialization} = \frac{CBH(460+25.9FMC)^{3/2}}{100} \text{ (in W m}^{-1}\text{)} \tag{10}$$

where CBH represents the canopy base height. R_{10}, refers to the surface fire spread rate for fuel behaviour model 10 (Mandel et al., 2011; Rothermel, 1972), with its components calculated within the 'fire_ros_cawfe_crown' subroutine, as defined in Eq. (11).

$$R_{10} = R_{back_{10}} + R_{wind_{10}} + R_{slope_{10}} \text{ (in m s}^{-1}\text{)} \tag{11}$$

By substituting Eq. (11) into Eq. (5) from the 'consume_crown' subroutine and incorporating Eq. (8) for crown fraction burned (*CFB)* from the same subroutine, Eq. (12) can be derived to calculate the total fire spread following Van Wagner (1989, 1993) and the Forestry Canada Fire Danger Group (1992), considering Eq. (9).

$$R_{final} = \begin{cases} R_{surface} + CFB\left(R_{active} - R_{surface}\right) & with\ crown\ spread \\ R_{surface} & otherwise \end{cases} \text{ (in m s}^{-1}\text{)} \tag{12}$$

The fire_total_intensity subroutine calculates the fire energy flux (ϕ) (W m^{-2}, Mandel et al. (2011)) originating from the combustion of dried fuel, as defined in Eq. (13),

$$\phi = \frac{W_{surface}}{dt} R_{final} \left(1 - \frac{FMC}{1-FMC}\right) H_{Low} \tag{13}$$

where $W_{surface}$ represents the initial total mass of surface fuel (kg m^{-2}), and H_{Low} denotes the lower heat content of the fuel. This calculation, defined in Eq. (14), is performed to predict the fire intensity, I_{final} (Scott and Reinhardt, 2001), accounting for the integration between the shrub/herbaceous layer and the tree canopy.

$$I_{final} = \frac{(H+\phi.CFB)R_{final}}{60} \quad \text{(in W m}^{-1}\text{)} \tag{14}$$

2.1.7 Implementation of FRP in SFIRE

The following equations, implemented in module_fr_sfire_model, are used to estimate the radiative power emitted from a burning area A, based on the Stefan-Boltzmann law and the sensible-heat (calorimetry) relation. The radiative power P (Eq. (15)) is proportional to the emissivity ϵ, the Stefan-Boltzmann constant σ, the burnt area A, and the fourth power of the temperature T (K).

Alternatively, the equation can also be expressed in terms of the sensible heat flux Qs (W m^{-2}), the mass of the burned material m, and the specific heat capacity c of dry wood, as shown in Eq. (16).

$$P = 10^{-6}(\epsilon.\sigma.A.T^4) \quad \text{(in MW)} \tag{15}$$

$$P = 10^{-6}\left(\epsilon.\sigma.A.\left(\frac{Q_S}{m.c}\right)^4\right) \quad \text{(in MW)} \tag{16}$$

The parameters used in this study are as follows: an emissivity value of 0.85 (Àgueda et al., 2010; Riggan et al., 2004), a specific heat capacity for dry wood estimated as $c = 1500$ J (kg K)$^{-1}$ (Radmanović et al., 2014), and the Stefan-Boltzmann constant as $\sigma = 5.67.10^{-8}$. W (m^2 K^4)$^{-1}$.

2.1.8 Fuel Models and Terrain Data Assimilation Subroutine Implementation

The build_NFFL and build_ZSF subroutines are responsible for the integration of NFFL fuel behaviour models and high-resolution terrain elevation data into the SFIRE computational domain. This process is carried out following the procedure detailed below:

- Data Input and Configuration: The subroutines read user-provided input files, generated in accordance with the methodology described by Menezes et al. (2021) and Menezes (2015). One file contains categorical information on NFFL fuel models, while the other provides terrain elevation data. During this step, key parameters such as grid resolution, initial coordinates, geospatial constants, and the dimensions of both datasets are defined.
- Coordinate Calculation: Geodetic coordinates (latitude and longitude) corresponding to the input data grids are calculated based on the predefined cell size.

- Data Interpolation: The input fuel and terrain data are interpolated onto the SFIRE grid by identifying the nearest neighbouring grid nodes. This interpolation employs the Haversine formula to calculate geodesic distances, ensuring that the curvature of the Earth is properly accounted for in the spatial mapping.
- Result Storage: The resulting interpolated datasets are saved in binary format for efficient access and subsequent use during the simulation workflow.

2.1.9 Coupling SFIRE Outputs with the BRAMS Framework for Wildfire Emissions Simulation

The fill_sfire_info_and_get_emissions subroutine integrate the FRP generated by the SFIRE domain simulation into the coarse-resolution grid of the BRAMS model, enabling the calculation of wildfire emissions. It performs the following key tasks:

- Iterates over the SFIRE grid to identify cells with positive FRP, burned area and burn duration. These cells are classified as valid active fire points.
- Stores fire data: For each valid fire point, the corresponding information is stored in an array, indexed by geographic coordinates.
- Calls the subroutine “get_emission_in_global_brams_grid”, which:
    - Maps each fire point from the SFIRE grid onto the global BRAMS grid.
    - Associates each fire point with a vegetation type, based on land cover (COS) data provided within the BRAMS grid.
    - Calculates burned biomass and emissions of various particulate matter species (e.g., PM10, PM2.5), using emission factors and the flaming fraction, which distinguishes between flaming and smoldering phases.
- Aggregates emissions: The calculated emissions are summed into the respective BRAMS grid cells.
- Performs statistical calculations: Computes emission statistics, such as the mean and standard deviation of FRP and burned area for each BRAMS grid cell.

This workflow ensures a seamless integration between fire dynamics modelled by SFIRE and the atmospheric process represented in BRAMS, enabling accurate simulation of wildfire emissions and their atmospheric impacts. In this study, only BRAMS passive tracer dispersion capabilities are used, focusing on the transport and dispersion of tracers without engaging the full atmospheric chemistry module. This approach allows for detailed analysis of pollutant transport patterns while minimizing computational costs.

2.1.10 Fire Mesh Refinement and Coupling Strategy within the SFIRE–BRAMS Framework

In SFIRE–BRAMS, the fire module does not operate on an independent or arbitrary domain but rather on a refined computational mesh dynamically generated around the ignition point(s) specified by the user. The horizontal extent of this refined mesh is defined in degrees of latitude and longitude and determines the size of the nested fire grid within the parent BRAMS domain. The atmospheric grid resolution (typically 2–1 km down to 200 m) and an integer refinement factor (even-valued) jointly control the local fire-grid spacing, which usually ranges from 200 m to 10 m depending on factor user specifications.

Within this refined sub-domain, SFIRE resolves ignition, flame propagation, and perimeter evolution using the level-set method coupled with the Rothermel (1972) spread-rate formulation. The refinement must, however, remain physically consistent with the expected fire behaviour: excessively coarse fire meshes tend to smooth the flaming front and underestimate fire radiative power (FRP) and burned area, whereas overly fine meshes may become computationally prohibitive without a commensurate gain in accuracy.

Thus, the FRP/active-area/perimeter dynamics are not “scaled” but explicitly resolved at the SFIRE resolution inside the BRAMS parent cell. In this study we selected the refinement factor by balancing physical realism with the maximum computational user capacity allowed on the available HPC infrastructure (memory per node and MPI task limits), ensuring that SFIRE could explicitly resolve fire-front geometry while maintaining BRAMS time-step stability and tractable wall-clock cost.

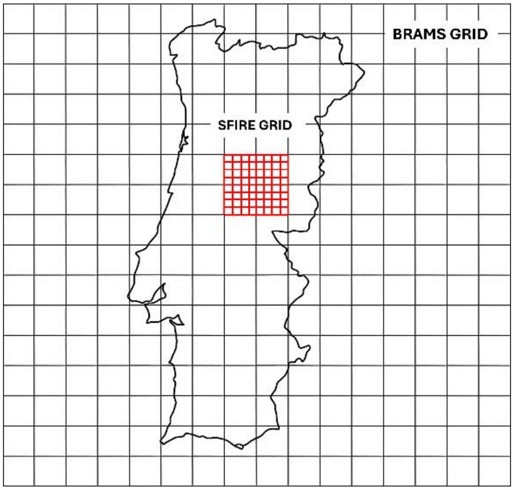

Figure 4: Schematic representation of the SFIRE–BRAMS grid nesting approach. Only for illustration a regular 14×14 coarse-resolution BRAMS grid is superimposed on the outline of mainland Portugal, illustrating the atmospheric model domain onto which the finer-resolution SFIRE fire grid can be dynamically embedded.

The simulation domains used in this study are shown in Fig. 5. The coarser domain, corresponding to the BRAMS grid, was configured with a 2 km resolution, while the inner SFIRE domain was nested at a finer resolution of 200 m.

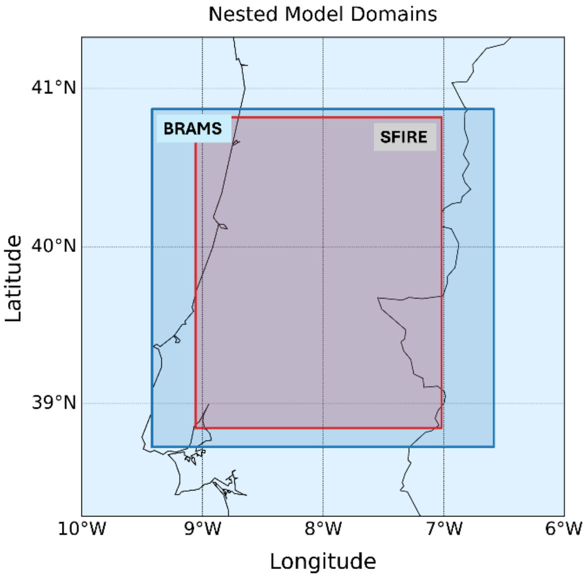

Figure 5: Nested simulation domains over central–northern Portugal. The dark-blue region represents the coarse BRAMS domain (2 km resolution), while the red–cyan region corresponds to the inner high resolution SFIRE domain (200 m resolution).

2.1.11 Radiative–Aerosol Coupling within BRAMS for Applications over the Iberian Peninsula

Given the limited spatial-temporal coverage of satellite aerosol products (e.g., MODIS, VIIRS) and reanalysis dataset such as MERRA-2, particularly under cloud, or nighttime conditions and for short-lived, small-scale agricultural burns (Oliveira et al., 2025), physically based models such as BRAMS, offers both a complementary and, when required, a fully self-contained alternative. BRAMS can ingest satellite information for constraint and evolution, but it also runs in a physically based, coupled fire–atmosphere mode that explicitly simulates fire spread from fuel properties and meteorological conditions, prognoses fire radiative power (FRP), and resolves smoke concentration fields alongside meteorological and thermodynamic variables. Although BRAMS does not directly provide aerosol optical properties, in this work, we diagnostically derive them from its prognosed aerosol mass and thermodynamic fields (e.g., temperature and relative humidity). Using Mie theory and radiative-transfer formulations, we obtain spectrally and vertically resolved extinction, scattering, and absorption coefficients, from which we compute integrated optical metrics such as aerosol optical depth (AOD), single-scattering albedo (SSA), and the asymmetry factor. This physically consistent offline radiative post-processing allows us to assess how wildfire smoke modifies radiative fluxes and lower-tropospheric thermodynamics (e.g. heating/cooling rates, static stability, boundary-layer evolution), while enabling robust comparison with satellite-retrieved AOD.

Rosário et al. (2025) developed seasonal Aerosol Spectral Optical Properties (ASOP) models for aerosol mixtures affecting the atmosphere over the Iberian Peninsula. These models were implemented within the BRAMS framework for improved optical properties of particulate material emitted by a wildfire simulation using the SFIRE model coupled to BRAMS. Based on a long-term (2003–2023) characterization of aerosol microphysical properties, optical parameters, such as spectral AOD, Angstrom Exponent (AE), SSA asymmetry parameter, and refractive indices, were derived using Mie theory applied to AERONET sun photometer data. The ASOP models represent typical regional aerosol scenarios, including smoke, dust, and background aerosol mixtures. Spatial representativeness was evaluated through monthly correlations between MERRA-2 and AERONET data, including AOD and SSA, enabling the identification of areas predominantly influenced by each model. This approach enhances aerosol–radiative transfer simulations in BRAMS over the Iberian Peninsula, improving predictions of thermodynamic profiles and surface temperatures, while reducing uncertainties in the representation of aerosol optical properties.

2.2 Data requirements

2.2.1 Surface data used as input in SFIRE

To simulate the spread of surface and crown fires using SFIRE, high-resolution Northern Forest Fire Laboratory (NFFL) fire behaviour fuel models and terrain elevation data on a regular grid are required. The NFFL fuel behaviour models are a set of 13 canonical fuel categories developed by the US Forest Service's Northern Forest Fire Laboratory (Albini, 1976; Anderson, 1982) to parameterize surface fuel characteristics for operational fire spread modelling (Rothermel, 1972). Each model specifies representative fuel properties, such as fuel load partitioned by size class, surface-area-to-volume ratio, fuelbed depth, heat content, moisture-of-extinction, and live/dead fractions, that together determine rate of spread, fireline intensity, and flame length under given wind and slope. The NFFL models provide a standardised mapping between vegetation/fuel types and the inputs required by semi-empirical fire behaviour equations; they are widely used for case studies, fire danger rating, and coupled fire–atmosphere applications. While subsequent schemes expanded and refined these categories (e.g. the 40 "standard" fuel models of Scott and Burgan (n.d.)), the original 13 NFFL models remain a common reference and are frequently denoted as NFFL 1–13 (e.g. "NFFL 10 – timber litter and understory"). . In this study, NFFL fuel model data were derived from the Portuguese National Forest Inventory 6 (Menezes et al., 2021). Additional inputs are also needed for the "namelist.fire" file, including physical, thermal, chemical, and mineral specifications of surface vegetation (Menezes et al., 2021; Menezes, 2015), as well as of tree canopy fuel within the simulation domain (such as canopy base height (CBH) and crown foliar moisture content (FMC)) for 13 NFFL fuel models.

CBH and FMC values were assigned using GIS methods by intersecting primary and secondary land data with five dominant forestry species (Table 1) and cross-referenced with the 13 NFFL fuel models. These data were part of 7,964 field plots of the 2006 National Forest Inventory, provided by the Portuguese Institute for Nature Conservation and Forests (ICNF, 2015), and adopted from the work of Menezes (Menezes, 2015) based on measurements conducted in October 2010 in the Évora district, part of the Alentejo region in southern Portugal, characterized by agro-silvopastoral landscapes known as Montado. Although FMC values from international literature were considered, they were ultimately excluded from this study, as they may not accurately represent the climatic, edaphic, and physiological conditions of Portuguese ecosystems. The FMC values presented in Table 1 were therefore used to do this classification.

Table 1: Average crown foliar moisture content (in %) for the 13 NFFL fuel models based on field data from five dominant forestry species (Alentejo, Portugal; October 2010) (Menezes, 2015)**.**

Tree species	**FMC**
Pinus pinaster Aiton	126.89
Pinus pinea L.	129.62
Eucalipto globulus Labill	118.51
Quercus rotundifolia	63.37
Quercus suber L.	72.32

Following the same methodology, CBH was determined. CBH is influenced by factors such as forest management practices, stand density, tree age, and species composition. In Portugal, CBH values can vary significantly. The specific average ranges, calculated using only the same five tree species, for each of the 13 NFFL fuel models, are detailed in Table 2.

Table 2: Average canopy base height (in meters) for the 13 NFFL fuel models based on field data from five dominant forestry species (Alentejo, Portugal; October 2010) (Menezes, 2015)**.**

Fuel Models	**CBH**
NFFL 1	6.43
NFFL 2	8.28
NFFL 3	8.11
NFFL 4	8.02
NFFL 5	10.04
NFFL 6	8.94
NFFL 7	9.67
NFFL 8	7.36
NFFL 9	7.32
NFFL 10	7.60

NFFL 11	7.02
NFFL 12	3.02
NFFL 13	0.62

2.2.2 Surface and meteorological data used as input in BRAMS

To establish the initial atmospheric state, BRAMS incorporated several datasets, including land cover type, soil type, the Normalized Difference Vegetation Index (NDVI), weekly sea surface temperatures, daily soil moisture, and soil temperature. The NDVI was derived from 15-day MODIS composite images spanning 2001 to 2002 (Moreira et al., 2013), while weekly sea surface temperature data were obtained from datasets distributed by (Reynolds et al., 2002). Daily soil moisture, an operational product of CPTEC/INPE based on rainfall estimated from TRMM (Gevaerd and Freitas, 2006), was also integrated. The initialization of soil temperature was based on air temperature values from the first level of the BRAMS atmospheric model.

Terrain elevation data with a spatial resolution of 30 arc seconds (approximately 1 km) in latitude and longitude were sourced from the United States Geological Survey's Earth Resources Observation Systems data centre (Gesch et al., 1999) and assimilated during the model initialization.

The atmospheric fields, including zonal and meridional wind, air temperature, geopotential height, and relative humidity, used for both the initialization and boundary conditions, were obtained from the ECMWF Reanalysis v5 (ERA5, 2019). These data were available at 37 vertical pressure levels and 6-hour intervals on a regular grid and were interpolated to the BRAMS grid to ensure consistency between the initial and boundary conditions.

2.2.3 Data used for model validation

Aerosol concentration, extinction coefficients, and AOD values were retrieved from the Modern-Era Retrospective analysis for Research and Applications, version 2 (MERRA-2, 2015) dataset. This dataset assimilates observations from a variety of instruments, including satellite-based radiometers, to provide global, long-term atmospheric reanalysis data.

MERRA-2 offers a spatial resolution of 0.5° × 0.625° and includes 72 hybrid-eta vertical levels extending from the surface to 0.01 hPa (Gelaro et al., 2017). Its temporal resolution is 3 hours, consistent across the various atmospheric and aerosol variables. The MERRA-2 collections used in this study were obtained from the Global Modeling and Assimilation Office (GMAO) (MERRA-2, 2015).

MERRA-2 uses the GEOS-5 model (~50 km, 72 levels) with the GOCART aerosol module and a 3-hourly aerosol analysis (GAAS). Column AOD at 550 nm is assimilated via three-dimensional variational data assimilation; the analysed AOD increments are projected to 3-D mixing-ratio increments for each species through $P_f H^T \left(H P_f H^T \right)^{-1}$ i.e., the analysis gain that maps an AOD increment into consistent black carbon (BC) and organic carbon (OC) updates by level and species, weighted by optical sensitivities and the model's background-error uncertainties. BC and OC are not observed directly; they are inferred from the AOD constraint combined with model radiation/transport and assumed optical/mixture properties (externally mixed tracers; hygroscopic growth vs RH; OPAC optics; non-spherical dust). Emissions for carbonaceous aerosols include QFED (Quick Fire Emissions Dataset, FRP-based) biomass-burning plus fossil/biofuel sources; losses include dry/wet deposition and scavenging. Oxidant fields use monthly climatology. A background-state correction and an averaging-kernel diagnostic are applied for consistency of the 3-h AOD analyses within the 6-h met cycle. In short, MERRA-2 BC/OC arise from AOD assimilation + radiative transfer with fixed assumptions on size, mixing state, vertical profiles, and emissions (Buchard et al., 2015; Buchard et al., 2016; Darmenov and da Silva, 2015; Randles et al., 2017).

2.3 Comprehensive Study of SOD and Atmospheric Properties

In this study, BRAMS simulations were used to provide aerosol mass concentration fields (e.g., PM25) associated with wildfire smoke. Since BRAMS does not explicitly calculate aerosol optical properties, these were derived off-line through additional post-processing. To link simulated aerosol mass with size distributions and optical characteristics relevant for biomass burning smoke, a set of representative assumptions and parameters was adopted, as summarized in Table 3. These choices ensure physical consistency with observed smoke properties and provide transparency and reproducibility for the optical analysis presented in the following sections.

2.3.1 Spectral SOD analysis and validation

In this study, the smoke optical depth (SOD) generated during the Sertã wildfire is characterized in terms of its magnitude, spectral dependence, and interaction with atmospheric radiation. The influence of meteorological conditions on SOD was also examined, considering variables such as temperature, relative humidity, and wind speed. SOD is defined as the vertical integral of the aerosol extinction coefficient, i.e. the sum of absorption and scattering contributions along the column (Seinfeld and Pandis, 2016). To estimate SOD from simulated wildfire smoke, we combined BRAMS PM25 concentrations with a physically based representation of particle size and hygroscopic growth.

The aerosol population is assumed to follow a lognormal size distribution characterized by a geometric mean radius and geometric standard deviation, with size evolution constrained by effective radii reported in field studies of biomass burning smoke (Reid et al., 2005). Hygroscopic growth is parameterized with the κ-Köhler approach (Petters and Kreidenweis, 2007), using κ values representative of fresh and mixed smoke conditions (Carrico et al., 2008; Engelhart et al., 2012). These parameterizations ensure consistency between modelled particle growth and observed microphysical properties reported in biomass burning studies. Under these assumptions, the extinction coefficient at wavelength λ and height z is given by Eq. (17), and the smoke optical depth follows as its vertical integral:

$$\beta_{ext}(z,\lambda) = \int_{r_{min}}^{r_{max}} Q_{ext}\left(m_{eff}(z,\lambda), r_{wet}, \lambda\right) \cdot \pi r_{wet}^2 n_{dry}\left(r_{dry}, z\right) dr_{dry} \tag{17}$$

$$SOD(\lambda) = \int_{z_0}^{z_t} \beta_{ext}(z,\lambda) dz \tag{18}$$

Where $r_{wet} = g(t, RH) r_{dry}$. Here, $\mathrm{Q_{ext}}$ is the Mie extinction efficiency (dimensionless), m_{eff} is the effective complex refractive index, r_{wet} is the physical (wet) particle radius "seen" by the light, and $n_{dry}\left(r_{dry}, z\right)$ is the differential number distribution with respect to dry radius [cm^{-4}] such that $\int n_{dry} dr_{dry} = N(z)$ [cm^{-3}]. Unit consistency is enforced internally (radii converted to a consistent length unit before evaluating πr^2). Because both $\mathrm{Q_{ext}}$ and πr^2 depend on the instantaneous particle size, all optical terms are evaluated with the wet radius r_{wet}.

2.3.2 Hygroscopic growth

Since condensation and coagulation are not explicitly modeled, hygroscopic growth is parameterized with the κ-Köhler approach (Petters and Kreidenweis, 2007):

$$g(t, RH) = \left(1 + \kappa \frac{RH}{1-RH}\right)^{\frac{1}{3}} \tag{19}$$

where κ is the hygroscopicity parameter. Literature-based ranges adopted here are:

- fresh/organic-dominated smoke: $\kappa \approx 0.06 - 0.30$ (Carrico et al., 2008).
- mixed/transitioning smoke: $\kappa \approx 0.08 - 0.30$ centered ≈ 0.2 (Engelhart et al., 2012).

κ is treated as a composition-dependent physical parameter and taken constant across the size distribution within each scenario (fresh, mixed), consistent with prior studies.

2.3.3 Size-distribution support and quadrature

The integration bounds are defined in dry-radius space as:

$$r_{dry} \in [r_{min}, r_{max}] = \left[r_g \sigma_g^{-k}, r_g \sigma_g^{k}\right] \tag{20}$$

with $k \approx 3-4$. Here r_g is the geometric mean (modal) dry radius and σ_g is the geometric standard deviation**.** Choosing $k \approx 3-4$ ensures that virtually the entire lognormal number/mass is captured (Hinds, 1999; Seinfeld and Pandis, 2016). The integral is evaluated using a logarithmic discretization of the dry-radius interval. While $n = 60-100$ bins are commonly recommended to adequately resolve lognormal size distributions for Mie calculations (Bohren and Huffman, 2008; Seinfeld and Pandis, 2016), a grid-convergence test performed here (n = 30 vs. n = 80) yielded negligible differences in bulk and spectral moments (e.g., number, extinction, SSA, AOD). We therefore adopt $n = 30$ to reduce computational costs without loss of accuracy for the present application.

$$r_j = r_{min}\left(\frac{r_{max}}{r_{min}}\right)^{\frac{j-1}{n-1}},\ j = 1, \dots, n \tag{21}$$

2.3.4 Relating r_e to (r_g, σ_g)

Most field studies report the (ambient) effective radius r_e, not (r_g, σ_g).Since a single r_e does not identify both r_g and σ_g, we (i) convert ambient r_e to dry conditions via $g(RH)$, and (ii) prescribe σ_g within literature ranges for biomass-burning fine mode ($\sigma_g \approx 1.5-1.9$, narrowing with aging; Reid et al. (2005)). The dry r_g then follows from the lognormal moment relation (Hinds, 1999; Seinfeld and Pandis, 2016):

$$\langle r^k \rangle = r_g^k exp\left(\frac{1}{2}k^2 ln^2\sigma_g\right), \qquad r_e = \frac{\langle r^3 \rangle}{\langle r^2 \rangle} = r_g exp\left(\frac{5}{2}ln^2\sigma_g\right) \tag{22}$$

Yielding,

$$r_g = \frac{r_e}{exp\left(\frac{5}{2}ln^2\sigma_g\right)} \tag{23}$$

A sensitivity analysis across plausible σ_g values quantify uncertainty in r_g and derived optics.

2.3.5 Mass-consistent normalization and mass fractions (no circularity)

Let $\tilde{n}(r)$ denote the unnormalized lognormal shape (any proportional form; the overall scale cancels in fractions). The mass fraction in bin j over $[r_j^-, r_j^+]$ is

$$f_j^{(M)} = \frac{\int_{r_j^-}^{r_j^+} r^3\tilde{n}(r)dr}{\int_{r_{min}}^{r_{max}} r^3\tilde{n}(r)dr} \tag{24}$$

so $f_j^{(M)}$ does not require N (the normalization cancels). Given bulk dry PM25 mass $C_m(t)$ in a layer, bin masses are $M_j = f_j^{(M)} C_m(t)$. If desired, bin-wise number follows from the third moment closure (Curci et al., 2015):

$$N_j = \frac{M_j}{\rho_j \frac{4}{3}\pi r_{g_j}^3 \, exp\left(\frac{9}{2} ln^2 \sigma_{g_j}\right)} \tag{25}$$

and the bin lognormal is

$$n_j(r) = \frac{N_j}{\sqrt{2\pi} r \, ln\sigma_{g_j}} exp\left[-\frac{ln^2\left(r/r_{g_j}\right)}{2ln^2\sigma_{g_j}}\right] \tag{26}$$

(Here ρ_j is the effective dry density per bin or scenario.)

2.3.6 Aging scenarios

We consider two plume-age scenarios (Andreae and Rosenfeld, 2008; Reid et al., 2005) since the studied fire lasted ~11 h and did not reach plume ages representative of aged/scattering conditions.

$$t = \{t_1\text{: fresh/absorbing}\,; t_2\text{: mixed}\}$$

These scenarios are summarized in Table 3. The smoke optical depth (SOD) was integrated hourly within each phase, with phase durations taken as ~6 h intervals.

Table 3. Classification of smoke-plume aging scenarios adopted in this study based in Reid et al., 2005

Phase	**Plume age**	**Classification**	$\boldsymbol{\sigma_g}$	$\boldsymbol{GMD}$ **(μm)**	$\boldsymbol{r_g = \frac{GMD}{2}}$ **(μm)**	$\boldsymbol{[r_{min}, r_{max}]}$ **(k=3,** $\boldsymbol{\sigma_g = 1.7}$**) (μm)**	**Notes**
t_1	0–6 h (Local time: 13:00h–19:00h)	Fresh / flaming (absorbing)	1.6–1.8 (typ. 1.7)	0.10–0.16 (centre ~0.13)	0.05–0.08 (typ. 0.065)	[0.013, 0.319] for (r_g = 0.065)	Fresh cores; very high number; rapid early growth observed.
t_2	6–12 h (Local time: 19:00h –23:00h)	Mixed / transition (incl. smouldering)	1.6–1.9 (typ. 1.7)	0.12–0.30 (most common ≈0.18)	0.06–0.15 (typ. 0.09)	[0.012, 0.442] for (r_g = 0.09)	Transition with smouldering + coagulation + some hygroscopic growth.

(Note: For a strictly lognormal distribution, the Count Median Diameter (CMD) and the Geometric Mean Diameter (GMD) are equivalent)

2.3.7 Derivation of MERRA-2 single-scattering albedo

MERRA-2 provides column-integrated aerosol optical extinction and scattering optical depths (AOD) at 550 nm, resolved by process and by species (BC, OC, and total). The single-scattering albedo (SSA) is defined as the ratio of scattering to total extinction:

$$SSA = \frac{\tau_{sca}}{\tau_{ext}} \tag{27}$$

From the MERRA-2 fields and from the model outputs, we computed species-specific SSA as:

$$SSA_{BC} = \frac{\tau_{sca}^{BC}}{\tau_{ext}^{BC}};\ \ SSA_{OC} = \frac{\tau_{sca}^{OC}}{\tau_{ext}^{OC}};\ \ SSA_{tot} = \frac{\tau_{sca}^{tot}}{\tau_{ext}^{tot}} \tag{28}$$

A combined smoke SSA representative of the fine-mode carbonaceous fraction was also derived as:

$$SSA_{BC+OC} = \frac{\tau_{sca}^{BC}+\tau_{sca}^{OC}}{\tau_{ext}^{BC}+\tau_{ext}^{OC}} \tag{29}$$

This same formulation was applied to the BRAMS–SFIRE simulations to ensure consistency with the MERRA-2 diagnostic structure and to enable a direct comparison of modelled and reanalysis optical properties.

2.3.8 Optical properties and spectral dependence of smoke aerosols

The specific extinction efficiency was computed using Mie theory as a function of particle radius, wavelength, and complex refractive index. A wavelength-dependent refractive index was prescribed following observational and review studies on biomass burning aerosols (Andreae and Gelencsér, 2006; Bond and Bergstrom, 2006; Kirchstetter et al., 2004; Reid et al., 2005). In this parameterization, the real part was held approximately constant at ~1.55, consistent with values typically reported for smoke particles, while the imaginary part was assumed to decrease with wavelength, reflecting stronger absorption in the blue due to brown carbon. The refractive indices applied in the simulations were 1.55 + 0.04i at 400 nm, 1.55 + 0.02i at 550 nm, and 1.55 + 0.01i at 700 nm. The Mie computations were used to derive the wavelength-dependent extinction and scattering efficiencies applied in the BRAMS–SFIRE radiation parameterization. However, the single-scattering albedo (SSA) itself was diagnosed from the ratio of scattering to total extinction optical depth in both the model and the MERRA-2 data, ensuring consistency between modeled and reanalysis optical properties.

This study analysed three representative wavelengths from the visible spectrum: 400 nm (blue), 550 nm (green), and 700 nm (red). Aerosol particles produced during flaming combustion and from internal combustion engines are largely composed of BC and OC, both of which affect the Earth's radiative balance by reducing visibility and surface irradiance (Bond et al., 2004). Black carbon is commonly used synonymously with soot, the major light-absorbing component of combustion aerosols in the visible spectrum (Bond and Bergstrom, 2006; Kirchstetter et al., 2004). BC consists of aggregates of nearly pure carbon spherules, with minor amounts of heteroatoms such as hydrogen and oxygen (Andreae and Gelencsér, 2006). Its microstructure is often described as onion-like, with an outer shell of disordered graphitic platelets surrounding a more amorphous carbonaceous core. Unlike crystalline graphite, the platelet layers are turbostratic, meaning that they are misaligned and wrinkled rather than parallel (Biscoe and Warren, 1942; Bond and Bergstrom, 2006). These morphological and chemical characteristics explain the nearly wavelength-independent absorption of BC across the visible spectrum.

In contrast, organic carbon, particularly in the form of brown carbon, exhibits stronger absorption at shorter wavelengths in the near-UV and blue regions, with absorption efficiency decreasing rapidly toward the visible and near-infrared (Andreae and Gelencsér, 2006; Kirchstetter and Novakov, 2004). This motivated the choice of 400 nm in the present analysis. The 550 nm band is a commonly used reference in atmospheric studies and satellite retrievals. At 700 nm, absorption by OC is already weak, while BC, with its nearly wavelength-independent absorption across the visible range, remains the dominant absorber. Although the absolute absorption by BC decreases with wavelength, its relative contribution becomes more important at longer wavelengths such as the red region (Bond and Bergstrom, 2006; Lack and Cappa, 2010).

SOD was calculated for each wavelength by vertically integrating extinction and absorption coefficients along both meridional and zonal cross-sections. The resulting SOD values were analysed in relation to thermodynamic parameters. Additionally, the influence of spectrally resolved smoke absorption on radiative transfer was examined, with emphasis on the visible to near-infrared range, to better understand the wavelength-dependent radiative impacts of smoke aerosols.

To ensure consistency with observational data, simulated SOD at 550 nm was directly compared with MERRA-2 AOD at the same wavelength. This spectral band is widely adopted as a standard reference in aerosol monitoring and ensures compatibility between model output and satellite-derived products.

Simulated SSA was compared with MERRA-2 SSA for BC and OC (Aerosol Optical Depth (AOD) at 550 nm), as well as with the total aerosol SSA from MERRA-2. Although the MERRA-2 files label BC and OC variables as Aerosol Optical Thickness (AOT), we refer to them as Aerosol Optical Depth (AOD) throughout the manuscript for consistency with the literature. Furthermore, SOD at 550 nm was evaluated against MERRA-2 BC and OC extinction AOD. Simulated PM2.5 concentrations were also compared with MERRA-2 BC and OC mass concentrations.

2.4 Gridding, Background Correction, and Sensitivity Tests

All variables were compared on the coarse BRAMS–SFIRE grid (2 km outer domain). The MERRA-2 fields were bilinearly interpolated onto the BRAMS grid to enable grid-point matching and to preserve the higher spatial detail of the model fields. This approach ensured a consistent spatial comparison while avoiding artificial smoothing that would result from regridding the model data to the coarser MERRA-2 resolution. For each variable (AOD, SSA, BC, OC, and PM2.5 concentrations), collocated grid-point pairs were extracted and used to construct bivariate scatter plots and compute standard statistical metrics. A detailed description of the analysis methodology is provided in the following subsections.

2.4.1 Apples-to-apples gridding

To ensure spatial representativeness and minimize interpolation artifacts, all comparisons were performed on the native BRAMS–SFIRE grid (2 km outer domain). MERRA-2 aerosol fields were bilinearly interpolated onto the BRAMS latitude–longitude grid within the common sub-domain (with longitudes wrapped to $[-180, 180]$). Diagnostics included Total Aerosol Extinction AOD ($AOD_{Total_{ext}}$) and Scattering AOD ($AOD_{Total_{scat}}$) at 550 nm from which the MERRA-2 single-scattering albedo was derived as:

$$SSA_{MERRA} = AOD_{Total_{scat}}/AOD_{Total_{ext}} \tag{30}$$

Where available, BC/OC extinction and scattering components were also used. Temporal pairing employed the nearest MERRA-2 timestamp to the model output.

2.4.2 Upwind/background subtraction

To isolate the fire-plume contribution and minimize background bias, an upwind background AOD field was computed on the BRAMS grid, and the adjusted plume AOD was defined as:

$$AOD' = max\left(AOD - AOD_{upwind}, 0\right) \tag{31}$$

Upwind edges were diagnosed from near-surface flow (u_{10}, v_{10}) or, when unavailable, from the median wind in the lowest five model layers (u_e, v_e). The upwind band width was set to 18 % of domain size along the inflow boundaries (W if $u > 0$, E if $u < 0$; S if $v > 0$, N if $v < 0$). Within that band, AOD_{upwind} was estimated as the median of the lower half of AOD values, ensuring robustness to residual plume contamination.

2.4.3 Phase windows vs. diagnostic scenarios (orthogonality)

The phase windows (t_1: 13–19 UTC “fresh”, t_2: 19–24 UTC “mixed”) are temporal subsets used to stratify the analysis and to assign phase-specific optical parameters (σ_g, κ, $r_{g,dry}$) The scenario labels in the statistical tables (BASE, ABSORBING, WIDE SIGMA, SMALL RG, LARGE RG) denote diagnostic post-processing optical variants applied to the Mie/closure calculator at fixed aerosol mass within each phase. Accordingly, for each simulation and for each phase (t_1/t_2), we report statistics under multiple diagnostic scenarios as described in Subsection 2.4.6.

2.4.4 Phase selection and scope

To reduce diurnal aliasing and ensure stable grid-point pairing, the main evaluation focuses on the mixed phase (19–24 local time), when the plume is less rapidly evolving and spatial gradients are weaker. This choice minimize sensitivity to sub-grid plume meandering and transient emission spikes that are more pronounced during early-afternoon hours, providing more stationary conditions for statistical comparison with the reanalysis. Domain-wide all-hours aggregates are also included for completeness.

2.4.5 Microphysical phase windows and simulation setups

To capture plausible within-plume microphysical evolution while preserving mass consistency, two temporal phase windows were defined:

- a daytime fresh-smoke period (t_1: fresh⁄absorbing, 13–19 UTS, dominated by recently emitted, BC/OC-rich smoke) and,
- an evening mixed period (t_2: mixed, 19–24 UTS, representing more aged, diluted, and partially hygroscopic smoke),

For each phase, one-at-a-time envelopes were applied to the lognormal parameters and hygroscopicity to represent conservative and lower-bound microphysical states:

- Baseline:
  t_1 - fresh⁄absorbing: $\sigma_g = 1.70, \kappa = 0.12, r_{g,dry} = 0.065\ \mu m$,
  t_2 - mixed: $\sigma_g = 1.70, \kappa = 0.20, r_{g,dry} = 0.090\ \mu m$
- Conservative (narrower/less hygroscopic):
  t_1 - fresh⁄absorbing: $\sigma_g = 1.60, \kappa = 0.08, r_{g,dry} = 0.060\ \mu m$
  t_2: mixed: $\sigma_g = 1.60, \kappa = 0.14, r_{g,dry} = 0.080\ \mu m$
- Lower envelope (most conservative bounds used):
  t_1 - fresh⁄absorbing: $\sigma_g = 1.60, \kappa = 0.06, r_{g,dry} = 0.055\ \mu m$
  t_2 - mixed: $\sigma_g = 1.60, \kappa = 0.10, r_{g,dry} = 0.070\ \mu m$

For all runs presented in the plots of SOD, SSA, and extinction or absorption coefficients, the complex refractive index was prescribed as wavelength-dependent:

m(λ)={400:1.55+0.04i;550:1.55+0.02i;700:1.55+0.01i} (32)

No additional spectral perturbation was applied beyond this baseline, and the Mie calculations were evaluated at 400, 550 and 700 nm wavelengths. The geometric integration bounds for the lognormal distribution were fixed at $k = 3$, ensuring consistent coverage (~±3 σ) coverage across all cases. Consequently, the sensitivity analysis isolates the effects of σ_g, κ and $r_{g,dry}$ witouht altering the prescribed refractive indices $m(\lambda) = n(\lambda) + ik(\lambda)$, in particular, no additional increment of the imaginary refractive part (e.g., no +0.02 at 550 nm) and no changes to the spectral slope of $k(\lambda)$ were introduced.

All statistical metrics (correlation, bias, RMSE, etc.) were derived from the same Mie-calculated optical fields, evaluated at 550 nm using the wavelength-dependent refractive index m(550)=1.55+0.02i.

2.4.6 Post-processing optical sensitivity scenarios (diagnostic only)

To explore the optical closure sensitivity at fixed aerosol mass, a set of diagnostics, one-at-a-time optical scenarios was applied in post-processing. These scenarios modify only the parameters used by the optical calculator (Mie/closure efficiencies Q_{ext}, Q_{abs}, Q_{sca}) while keeping the simulated aerosol fields unchanged.

Let σ_g, κ and $r_{g,dry}$ denote the base parameters defined for phase t (fresh or mixed). Each scenario perturbs these parameters through multiplicative scaling factors (s_g, s_κ and s_r) and/or an additive increment in the imaginary refractive index $k(\lambda)$:

- BASE: reference optics for the active phase, using the absolute microphysical parameters defined for each phase window (no additional perturbation applied).
- ABSORBING-like: increased intrinsic absorption and reduced hygroscopic growth ($k(\lambda) = +0.02$ at 550 nm; κ scaled by 0.6).
- WIDE SIGMA: implemented by increasing the lognormal width (σ_g) relative to the phase baseline, conserving column mass. The particle size grid is logarithmically spaced with $n = 30$ bins over $\left[r_g \sigma_g^{-3}, r_g \sigma_g^{3}\right]$.
- SMALL/LARGE RG: smaller or larger dry geometric radius ($r_{g,dry}$ scaled by 0.8 / 1.2), representing discrete phase-specific configurations rather than ±20 % perturbations.

The absolute optical values therefore depend on the phase-specific baseline, while the scaling factors define the relative perturbation applied in each diagnostic scenario. Percentile masks (P70–P90) were computed for exploratory statistics, while the main analysis and figures report domain-wide (all-hours) results.

2.4.7 Evaluation metrics and visualization

Model–reanalysis pairs were formed on the native BRAMS grid after bilinear interpolation of MERRA-2 and nearest-hour temporal pairing. Statistics were computed for both the raw AOD and the background-corrected field:

$$AOD' = max\left(AOD - AOD_{upwind}, 0\right) \tag{33}$$

No percentile ("in-plume") masks were applied; all valid grid-point pairs over the common domain were used.

The diagnostic set comprised means of X and Y, bias (X-Y), mean absolute error (MAE), root-mean-square error (RMSE), Pearson correlation coefficient (r) and Spearman's rank correlation coefficient (ρ), and ordinary-least-squares (OLS) linear fit $Y = aX + b$ with R^2. We evaluate $X = SOD_{550}$ against $Y \in \{AOD_{550}, AOD'_{550}\}$, and applied the same framework to SOD vs. BC/OC extinction and to SSA (model) vs SSA (MERRA-2). Hourly results were aggregated into all-hours summaries. Scatter plots were rendered as log-density hexbin diagrams to avoid overplotting, showing the 1:1 reference and the OLS fit; with key metrics (e.g., r, ρ, RMSE, bias) annotated on each panel.

2.4.8 Physical background (AOD upwind)

In this approach, the background optical depth (AOD_{bg}) is computed upwind of the smoke plume, that is, within grid cells located in the direction opposite to the plume advection, where the smoke has not yet arrived. These regions represent the true clean-air background entering the domain before interacting with the fire emissions.

Formally,

$$AOD_{bg} = mean\left(AOD_{upwind\ region}\right) \tag{34}$$

where the upwind region is defined according to the 10 m wind field or the mean flow within the mixed layer. Have the advantage be physically consistent, as it represents the incoming air mass prior to smoke influence. The limitation requires an accurate estimate of wind direction and a well-defined upwind spatial mask to exclude partially affected cells.

2.4.9 Computation of background-subtracted fields

The background flag (TRUE/FALSE) in Tables S1–S3 of supplementary material indicates whether a spatial background removal was applied before computing the statistical metrics:

- FALSE (no background subtraction):
  Statistics are computed directly from the raw fields, X= AOD, Y= SOD
- TRUE (with background subtraction):
  A background level is estimated for each hourly field to isolate the smoke-related anomaly.
  1. Background estimation:
     AOD_{bg} is s taken as the spatial median (or a low quantile, e.g. P10–P25) of "clean-air" grid cells within the domain for that hour.
     The same approach is applied to SOD_{bg} (often ≈ 0 in the model).

2. Anomaly computation:

   $AOD' = max(AOD - AOD_{bg}, 0)$

   $SOD' = max(SOD - SOD_{bg}, 0)$

3. Statistical comparison:

   The diagnostics are then computed using $X = AOD', Y = SOD'$

This procedure removes the nearly constant regional aerosol offset present in MERRA-2 but not in the simulated plume, thereby reducing bias and intercept values and typically improving correlation. In some experiments, the background may alternatively be derived from the corresponding no-fire run; the principle, using anomaly fields to represent fire-related optical depth, remains the same.

2.4.10 Quality control

Relative humidity was clipped to the physical range $[0, 0.999]$. Heights are read directly in meters or derived from geopotential divided by gravitational acceleration (g), and column thickness was verified to lie within plausible atmospheric limits. All configurable parameters, including the upwind-band width, statistical options, and sensitivity factors, were documented to ensure reproducibility.

2.5 Absorption of Solar Radiation by Smoke and Radiative Budget Impacts

The radiative balance was analysed by comparing simulations results with and without fire, specifically considering surface downwelling shortwave radiation (W m^{-2}), and surface downwelling longwave radiation (W m^{-2}). These accumulated energy fluxes are used to evaluate the radiation budget under smoke conditions at the surface. The smoke-absorbed shortwave radiation at 550 nm ($F(550\ nm)_{abs}$, W m^{-2}) was estimated based on the heating potential of the fire plume and the vertical profile of aerosol absorption using the following relation expressed in Eq. (35):

$$\tau_{abs}(550) = \int_{z_0}^{z_t} \int Q_{abs}\left(m_{eff}(z, 550), g\, r_{dry}, 550\right) \pi \left[g\, r_{dry}\right]^2 n_{dry}\left(r_{dry}, z\right) dr_{dry} dz \qquad (34)$$

$$F(550nm)_{abs} = H_{sen}\, \tau_{abs}(550) \qquad (35)$$

Where H_{sen} is the surface sensible heat flux associated with the fire.

2.6 Vertical Profiles of Aerosol Optical Properties and Atmospheric Stability

Atmospheric stability was assessed specifically within smoke-affected layers of the atmospheric column. The analysis focuses on detecting thermal inversions by examining vertical profiles of potential temperature and relative humidity in regions influenced by simulated smoke, under both fire and no-fire scenarios. A thermal inversion is identified when both potential temperature and relative humidity increase with height.

To evaluate the impact of smoke on atmospheric stability, these thermodynamic profiles were analysed in conjunction with vertical distributions of smoke extinction and absorption coefficients at 550 nm. This approach highlights the interaction between radiation and fine particulate matter (PM2.5), and the resulting effects on local temperature structure.

Furthermore, Convective Available Potential Energy (CAPE) and Convective Inhibition (CIN) were compared for smoke and non-smoke conditions. Differences in these parameters (ΔCAPE and ΔCIN) were computed and represented as vertical profiles, providing insights into how smoke alters convective dynamics and overall atmospheric stability.

3 Results and discussion

In the following sections, the burned area resulting from the wildfire episode in Sertã is compared between simulations using the BRAMS and WRF models, in order to assess fire spread performance under forested and complex topographic conditions. Simulated SOD is evaluated against MERRA-2 AOD to assess spatial and temporal coherence. Column-integrated extinction coefficients at 550 nm are also compared with extinction derived from MERRA-2 BC and OC aerosol components, in order to verify whether the simulated optical processes reflect the dominant aerosol types observed.

The simulated SSA is compared with MERRA-2 SSA, along with simulated and MERRA-2 aerosol mass concentrations, to validate whether the simulated aerosol composition, particularly the relative abundance of BC and OC, is consistent with observed radiative behaviour. This comparison also aims to verify whether the simulated mass profiles of BC, OC, and PM2.5 correspond to the resulting optical properties. Frequency distributions of particulate matter concentrations across the simulation domain are analysed to assess the spatial variability and intensity of aerosol loading. Additionally, the impact of smoke absorption on surface downwelling shortwave and longwave radiation is evaluated.

The optical effects on atmospheric stability layers are investigated through the analysis of CAPE and CIN. Vertical profiles of extinction and absorption coefficients are further examined in relation to the development of thermal inversion layers, in order to determine whether the model accurately reproduces the optical signature of smoke in radiative transfer simulations.

3.1 BRAMS and WRF model differences in burned area representation and their implications

Significant differences in the simulated burned area for the same Sertã wildfire event, as depicted in Fig. 6, were observed between BRAMS-SFIRE and the WRF-SFIRE results previously reported by Menezes et al. (2024). BRAMS-SFIRE simulated a broader westward spread, while WRF-SFIRE produced a more confined footprint, extending further north. These discrepancies arise from differences in model configuration, fire propagation schemes, and spatial resolution.

First, although WRF-SFIRE resolves fire spread at a finer horizontal resolution (20 m) than BRAMS-SFIRE (200 m), BRAMS exhibits stronger sensitivity to terrain-induced effects due to its topographic assimilation and interaction with the atmospheric fields at coarser grid scales (2 km in diagnostics). This can amplify upslope spread, especially on west-facing slopes, where heating of unburned fuels by the flame front is intensified. Additionally, BRAMS employed a default rate of spread approximately ten times greater than that used in WRF, resulting in more aggressive lateral fire expansion, particularly in regions where wind-driven constraints are weaker.

Second, resolution differences in output diagnostics further influence the apparent burned area. WRF's higher resolution (20m) output preserves more spatial detail, limiting smoothing of the burned footprint. Conversely, the BRAMS burned area (200 m resolution) was accumulated and plotted in BRAMS 2 km grid resolution, which introduces spatial averaging and may artificially enlarge the apparent extent of fire-affected regions.

Moreover, the delayed onset of burned area in BRAMS-SFIRE when using lower propagation rates is not solely due to ignition misalignment, but rather a result of the interaction between the fire spread rate and the coarser fire grid resolution (200 m). Unlike WRF-SFIRE, which operates at a much finer 20 m resolution for fire propagation, BRAMS requires the flame front to traverse larger grid cells to ignite neighbouring areas. This means that if the default rate of spread is reduced without compensating for grid size, the fire may fail to reach adjacent cells in a timely manner, leading to an underrepresentation of burned area in the early stages. Therefore, a balanced calibration is needed between the fire spread rate and grid resolution in BRAMS to ensure that the ignition front progresses consistently with observed timelines. While finer resolution in WRF (20 m) inherently provides more accurate spatial detail in fire development (Menezes et al., 2024), BRAMS relies on a more approximate representation, making it sensitive to how rate-of-spread parameters are tuned relative to its mesh scale.

In summary, while WRF-SFIRE offers finer-scale detail in fire perimeter shape, BRAMS-SFIRE exhibits stronger coupling between fire dynamics, topography, and atmospheric feedbacks. For prognostic simulations of fire spread and smoke transport in complex terrain, BRAMS-SFIRE may provide enhanced physical realism — provided its rate of spread is properly calibrated to avoid over propagation, particularly in orographically enhanced directions.

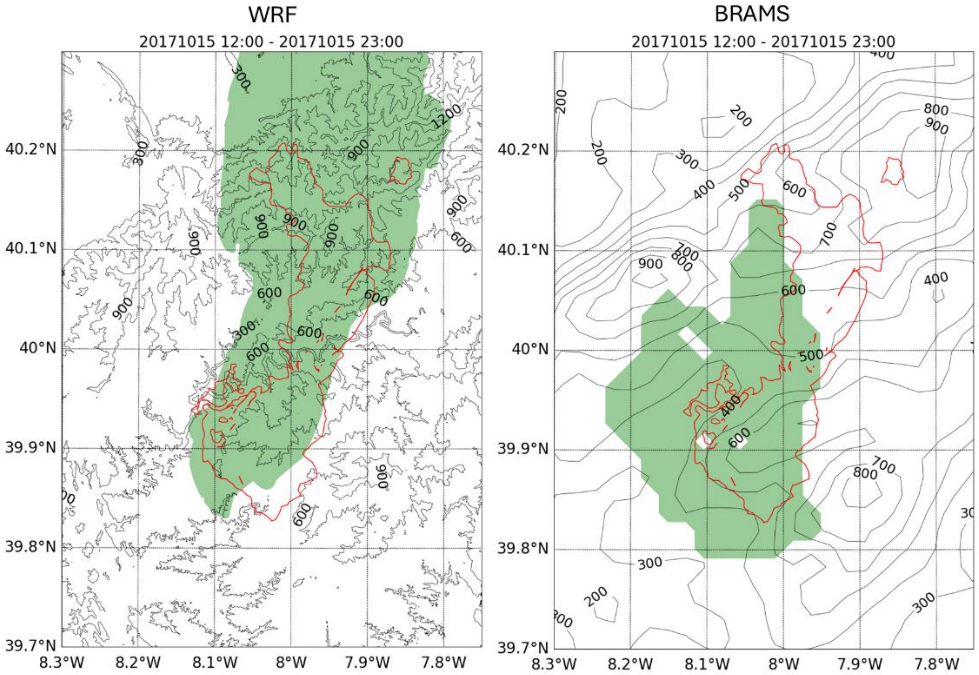

Figure 6: Comparison of simulated burned area over high-resolution topography from the (a) WRF-SFIRE and (b) BRAMS-SFIRE models for the wildfire event on 15 October 2017, accumulated between 12:00 and 23:00 UTC. Green-shaded regions represent the cumulative burned area, while red contours delineate the observed fire perimeter.

3.2 Optical properties comparison between SOD and AOD from MERRA-2

Forest fires, during their propagation, consume the available biomass as characterized by the different NFFL fire behaviour fuel models (Anderson, 1982), which represent the landscape, and release high concentrations of particles and trace gases into the atmosphere. Primary aerosols are emitted throughout combustion, during both the flaming and smouldering phases, while secondary aerosols form in the atmosphere through chemical reactions involving precursor gases. However, primary particles can serve as condensation nuclei or "seeds" for secondary particle formation through aging processes, resulting in internally mixed aerosols with complex and evolving chemical compositions as they are transported within the smoke plume. Primary particles include soot, predominantly composed of elemental carbon (BC), along with ash and mineral components derived from the burned biomass. These materials may exist as distinct particles or aggregate into larger mixed particles during combustion. Depending on their composition and surface properties, these aerosols can be hydrophilic (attracting water, enhancing growth in humid conditions) or hydrophobic (repelling water), affecting their interaction with radiation and their ability to act as cloud condensation nuclei (CCN).

As these particles are transported within the smoke plume, they undergo aging processes that alter their physical and chemical properties. These include: (1) Coagulation — collisions and merging with other particles, leading to increased size and complexity; (2) Surface reactions – interactions with atmospheric gases such as SO_2, NO_x, and volatile organic compounds (VOCs), including terpenes and isoprenes (emitted by vegetation during natural biological processes) and aromatic compounds (from biomass combustion). These reactions lead to the formation of sulfates, nitrates, and organic coatings; (3) Oxidation — particularly of BC, resulting in the acquisition of oxygen-containing functional groups that modify its optical properties and enhance hydrophilicity.

In parallel, VOCs are oxidized in the atmosphere to produce oxygenated organic compounds, such as carboxylic acids (e.g., formic acid, acetic acid) and aldehydes (e.g., formaldehyde), which contribute to the formation and growth of secondary organic aerosols (SOA). These compounds can condense onto primary particles, forming coatings that significantly modify their optical and hygroscopic properties.

Moreover, photochemical reactions involving VOCs and oxidants such as ozone (O_3) and hydroxyl radicals (OH) also lead to secondary particle formation. Not all secondary aerosols are of local fire origin; VOCs and precursor gases transported from urban pollution sources or natural vegetation in other regions may also contribute further to increasing the complexity of the smoke plume and its optical properties.

Both primary and secondary aerosols interact with solar radiation through scattering and absorption of shortwave (visible and near-infrared) radiation, reducing direct sunlight at the surface while enhancing diffuse radiation (Yamasoe et al., 2006). These particles also absorb and re-emit longwave (thermal infrared) radiation. While BC strongly contributes to absorption, sulfates and organic aerosols primarily enhance scattering, collectively influencing the atmospheric radiative energy balance (Yamasoe et al., 2006). The net result often includes local atmospheric heating, particularly in layers rich in BC.

These radiative interactions are governed by Mie theory, as most smoke particle sizes fall within the Mie regime (approximately 0.1 µm to 1 µm), where the particle diameter is comparable to the wavelength of incident radiation. Smaller particles ($\ll 0.1$ µm) scatter more efficiently at shorter wavelengths (e.g., blue light) and are better described by Rayleigh theory, which assumes particle sizes much smaller than the radiation wavelength. In contrast, larger particles exhibit non-selective scattering and remain within the Mie regime, with their radiative behaviour less dependent on wavelength.

Understanding the spectral behaviour of smoke aerosol optical properties is essential for interpreting optical depth measurements. In this context, both the simulated SOD at 550 nm and the MERRA-2 AOD at the same wavelength represent the column-integrated attenuation of solar radiation due to the presence of aerosols in the atmosphere. However, there are conceptual differences that affect their comparison. SOD corresponds specifically to the fraction of AOD attributed to smoke particles generated by wildfires and biomass burning, while MERRA-2 AOD includes all aerosol types present in the atmosphere, such as mineral dust, sulfates, nitrates, sea salt, and soot.

When $SOD \leq AOD$, it indicates that smoke aerosols constitute only a portion of the total aerosol load. In contrast, when $SOD \approx AOD$, it suggests that the majority of aerosols in the region and time analysed originate from biomass burning, which typically occurs during intense fire events with limited interference from other aerosol sources. Conversely, when $SOD \ll$

AOD, it implies a significant contribution from non-smoke aerosol sources, such as mineral dust (e.g., Saharan intrusions), industrial pollution (sulfates), or marine aerosols.

Figure 7 presents the spatial distribution of SOD under the Baseline configuration, for both dry and wet conditions, compared with MERRA-2 AOD at 550 nm at 18:00 UTC on 15 October 2017, during the t_1-fresh phase. Four fixed base classes between 0 and 4 (unitless) were defined, as this range is most representative of intense fire plumes. At this time, both SOD and AOD show a marked enhancement relative to earlier afternoon conditions, reflecting the intensification and vertical deepening of the smoke plume associated with the major wildfires over central Portugal. The dry SOD contours delineate the plume core, whereas the wet configuration extends further downwind, suggesting hygroscopic growth and enhanced optical thickness under humid conditions. Overall, the model reproduces the main spatial pattern of MERRA-2 AOD, albeit with a thinner and slightly displaced plume.

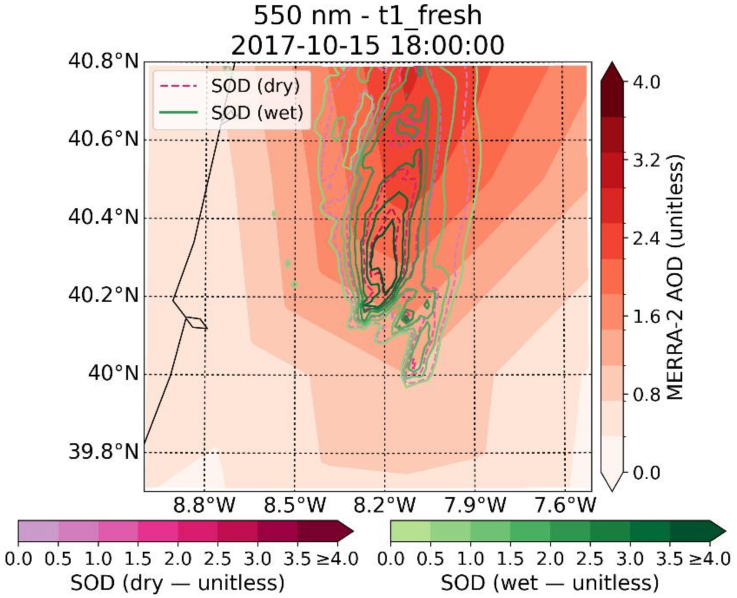

Figure 7: Spatial distribution of smoke optical depth (SOD) and MERRA-2 AOD (550 nm) over the study domain at 18:00 UTC on 15 October 2017, during the intense Sertã wildfire episode. AOD is shown as shaded colours; SOD (dry) and SOD (wet) are overlaid as dashed and solid contours, respectively.

In the Baseline configuration, between 13:00 and 17:00 UTC, a strong decoupling was found between the simulated SOD and the MERRA-2 AOD (Fig. 8a). The high regression intercepts (dry: 0.94–2.05; wet: 0.90–2.05) indicate a persistent background aerosol contribution (regional haze, dust, or pollution) captured by MERRA-2 but not associated with the simulated smoke plume. The steep slopes (dry: 1.39–3.03; wet: 0.55–2.84), together with a narrow SOD range (mostly below 0.5), reveal that

AOD varied almost independently of SOD, suggesting a spatial or temporal offset between the modeled and observed plume positions.

From 18:00 to 23:00 UTC (Fig. 8b), the coupling between both datasets improves notably. The regression slopes decrease to 0.21–0.36 (dry) and 0.19–0.34 (wet), indicating that SOD variations begin to explain part of the AOD variability, although the model still underestimates the total column optical depth, producing a thinner smoke layer. The SOD (wet) configuration provides slightly better agreement ($r \approx 0.14$) than SOD (dry) ($r \approx 0.13$), while lower intercepts (dry: 0.66–0.78; wet: 0.65–0.77) denote improved representation of smoke-related aerosols and greater spatial consistency with MERRA-2.

The Conservative (Test 2) and Lower Envelope (Test 3) configurations exhibit similar overall behavior. During the fresh phase, intercepts range between 0.89–2.05 (dry) and 0.90–2.05 (wet) for the Conservative setup, and 0.89–2.05 (dry) and 0.90–2.05 (wet) for the Lower Envelope setup. In the mixed phase, intercepts vary between 0.66–0.77 (dry) and 0.65–0.76 (wet) for the Conservative case, and 0.66–0.78 (dry) and 0.70–0.77 (wet) for the Lower Envelope case. Corresponding slopes range from 0.21–0.36 (dry) and 0.20–0.33 (wet) for the Conservative setup, and 0.21–0.36 (dry) and 0.20–0.34 (wet) for the Lower Envelope. These variations indicate that reducing κ and $r_{g,dry}$ or narrowing σ_g produces only moderate changes in the regression metrics, confirming that the optical results are relatively insensitive to plausible microphysical perturbations.

Overall, all configurations consistently reproduce the main spatial structure of the observed plume but underestimate its total optical depth. The wet runs yield the best correspondence with MERRA-2, emphasizing the importance of hygroscopic growth in reproducing observed AOD magnitudes during the plume's mature stage.

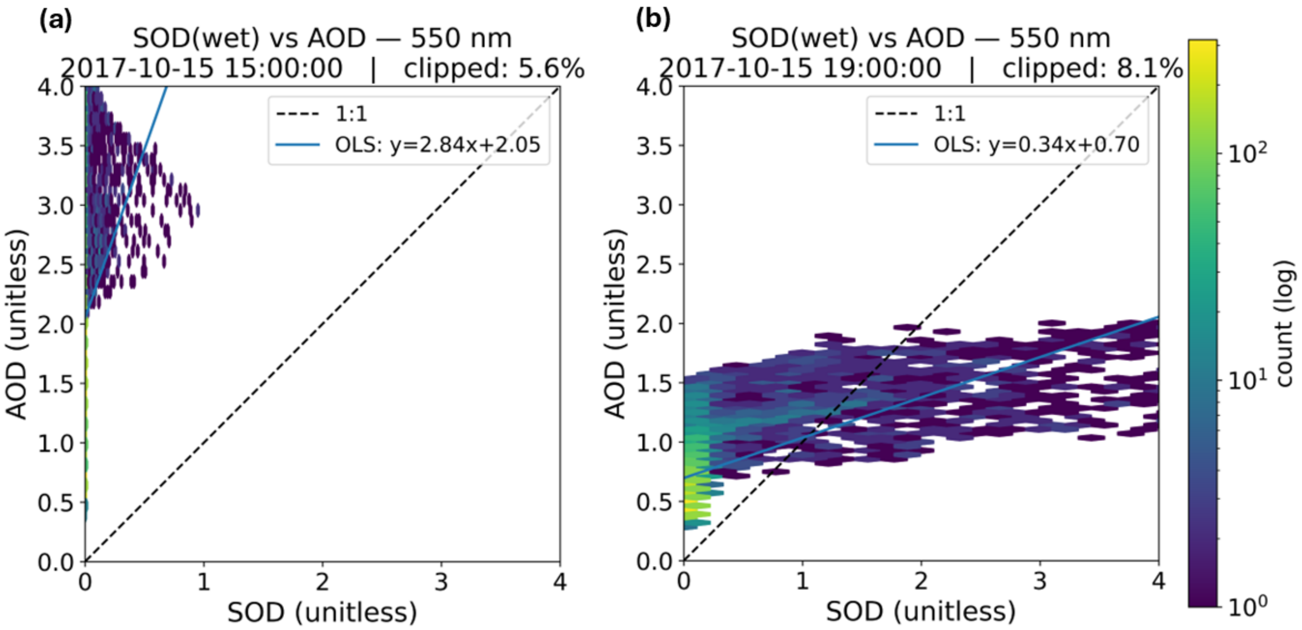

Figure 8: Scatter density plots comparing simulated SOD (wet) and MERRA-2 AOD at 550 nm for 15:00 UTC (panel a) and 19:00 UTC (panel b) on 15 October 2017. The dashed line represents the 1:1 relationship, and the solid line the ordinary least-squares (OLS) regression. Color shading denotes the logarithmic count of grid-point pairs. The clipped percentage indicates the fraction of points excluded from the plot due to exceeding the displayed SOD/AOD range (≥ 4.0).

Table 4 shows that during 13:00–17:00 UTC (fresh), the model exhibits large negative bias to SOD (−2.22 to −0.94), high MAE/RMSE (up to 2.45), and weak linear coupling ($r = 0.04$–0.56; $R^2 = 0.00$–0.31), indicating strong background dominance in AOD from MERRA-2 and limited overlap with the simulated plume as seen upper. Skill improves markedly from late afternoon into evening. At 18:00 UTC (fresh), bias is reduced (−0.74), MAE/RMSE attain their lowest values (0.83/0.92), and correlation strengthens ($r = 0.66$; $\rho = 0.93$; $R^2 = 0.44$). Around 19:00–20:00 UTC (mixed), correlations peak ($r = 0.70$–0.72; $\rho = 0.93$–0.95) with the highest R^2 (0.48–0.52); bias crosses from near-zero (−0.06 at 19:00) to slightly positive (+0.37 at 20:00), consistent with a transition from under to mild over-estimation of column optical depth. Later evening hours (21:00–23:00 UTC) maintain elevated correlations ($r = 0.57$–0.68; $\rho = 0.89$–0.93) but exhibit moderate positive bias (+0.17 to +0.30) and larger errors than at 18:00 UTC. Overall, the best trade-off between amplitude and association occurs at 18:00–20:00 UTC, with 18:00 minimizing error and 19:00–20:00 maximizing explained variance.

Table 4: Diagnostic statistics for the Sertã wildfire period, including the mean, bias, mean absolute error (MAE), root-mean-square error (RMSE), Pearson correlation coefficient (r) and Spearman's rank correlation coefficient (ρ), and coefficient of determination (R^2) of SOD and AOD.

Time (UTC)	Phase	Mean SOD	Mean AOD	Bias (SOD-AOD)	MAE	RMSE	r	ρ	R^2
13:00	fresh	0.00	0.94	-0.94	0.94	0.98	0.04	0.38	0.00
14:00	fresh	0.01	1.73	-1.73	1.73	1.85	0.12	0.72	0.02
15:00	fresh	0.03	2.24	-2.22	2.22	2.45	0.23	0.84	0.05
16:00	fresh	0.07	1.36	-1.29	1.29	1.42	0.45	0.87	0.20
17:00	fresh	0.15	1.29	-1.14	1.14	1.27	0.56	0.90	0.31
13:00	fresh	0.00	0.94	-0.94	0.94	0.98	0.04	0.38	0.00
14:00	fresh	0.01	1.73	-1.73	1.73	1.85	0.12	0.72	0.02
15:00	fresh	0.03	2.24	-2.22	2.22	2.45	0.23	0.84	0.05
16:00	fresh	0.07	1.36	-1.29	1.29	1.42	0.45	0.87	0.20
17:00	fresh	0.15	1.29	-1.14	1.14	1.27	0.56	0.90	0.31
18:00	fresh	0.35	1.09	-0.74	0.83	0.92	0.66	0.93	0.44
19:00	mixed	0.83	0.89	-0.06	0.97	1.51	0.70	0.93	0.48
20:00	mixed	1.17	0.80	0.37	1.26	2.25	0.72	0.95	0.52
21:00	mixed	1.13	0.83	0.30	1.21	2.06	0.68	0.93	0.46
22:00	mixed	1.03	0.86	0.17	1.16	1.88	0.62	0.91	0.39
23:00	mixed	0.91	0.89	0.02	1.12	1.71	0.57	0.89	0.32

The statistical diagnostics summarized in Tables S1–S3 described in the Supplementary material, quantify the effects of microphysical perturbations applied in the BASE, CONSERVATIVE, and LOWER ENVELOPE phases on the model–observation agreement during the mixed stage. Across all experiments, background subtraction (TRUE) systematically reduces both bias and error metrics, confirming that a large part of the apparent disagreement arises from regional background aerosols present in MERRA-2 rather than from deficiencies in the simulated plume. After background removal, the mean SOD and AOD become closely aligned (0.55–0.57 vs 0.46–0.57 µg m^{-3} for the ALL mask), and the bias decreases from roughly −0.6 to −0.1, while MAE and RMSE drop by 30–40 %. The correlation coefficients ($r \approx 0.15–0.17$, $\rho \approx 0.55–0.60$) remain moderate, reflecting residual spatial offsets but indicating that SOD captures the large-scale plume variability once the background signal is removed.

Focusing on percentile masks (P70–P90) reveals a clear progression with aerosol loading: as higher-AOD pixels are selected, both bias and error increase markedly, whereas correlation weakens and even becomes negative at the highest percentiles. This pattern suggests that the most optically thick parts of the MERRA-2 field include contributions from non-smoke aerosols or vertically extended layers not reproduced by the model. Regression slopes remain small ($|\text{slope}| < 0.2$), reinforcing that SOD amplitudes are much lower than AOD at plume peaks, but intercepts persistently near 1 indicate a quasi-constant background optical depth offset between datasets.

Comparing across microphysical configurations shows that the WIDE SIGMA, SMALL RG, and LARGE RG tests produce changes of less than ±0.1 in correlation and ±0.2 in MAE relative to BASE, confirming that realistic perturbations in particle size distribution width or geometric radius have limited impact on the optical diagnostics. Similarly, the ABSORBING variant slightly increases mean SOD (by ≈ 0.05–0.1) and yields marginally lower bias, consistent with stronger intrinsic absorption compensating for the model's underestimation of column optical depth. The near-identical metrics between the BASE, CONSERVATIVE, and LOWER ENVELOPE tables further demonstrate the model's robustness to plausible microphysical adjustments.

Physically, these results indicate that the residual mismatch between simulated SOD and observed AOD during the mixed phase is dominated by spatial and vertical representativeness errors rather than by uncertainties in particle hygroscopicity or size. Once the uniform background component is removed, the remaining SOD–AOD variability mainly reflects sub-grid plume displacement and MERRA-2's coarse resolution, not intrinsic optical-property biases. This reinforces the interpretation that the BRAMS-SFIRE system reproduces the evolving smoke distribution realistically in structure but underestimates its integrated optical depth, an effect only weakly sensitive to the tested microphysical perturbations.

Several structural and physical factors help explain the partial desynchronization observed between the simulated smoke optical depth (SOD) and the MERRA-2 aerosol optical depth (AOD).

The BRAMS–SFIRE runs at 2 km horizontal resolution and produce instantaneous outputs, whereas MERRA-2 provides ~0.5° × 0.625° (~50 × 70 km) hourly means centred near hh:30. This difference implies that sharp smoke gradients and localized peaks captured by the model are heavily smoothed in MERRA-2, both attenuating maximum AOD values and shifting their apparent timing relative to the simulated plume. The resulting smoothing also blends smoke with background aerosols, reducing the spatial contrast between plume and non-plume regions.

The SOD evaluated here is derived from fine-mode PM2.5 (fresh smoke), while MERRA-2 AOD represents total extinction, integrating coarse-mode dust and sea salt. In regions where coarse-mode aerosols are abundant, total AOD can diverge from, or even anticorrelate with fine-mode SOD in both space and time. This compositional difference is consistent with elevated regression intercepts, i.e. a background optical load not associated with the fire plume

MERRA-2 assimilates satellite AOD observations (e.g., MODIS, VIIRS), subject to retrieval/sampling constraints; its smoke fields depend on emission inventories and the analysis cycle. Rapid, pyro-convective injections from intense wildfires, characterized by sub-hourly variability and strong vertical transport, are difficult to capture in reanalysis products. This can produce phase shifts in both timing and vertical structure relative to the model, especially during the most active burning period (13–17 UTC).

The wet SOD uses modelled RH to allow growth in particle size and extinction efficiency. MERRA-2 may employ coarser meteorology and simplified κ parameterizations. Discrepancies in RH and κ directly affect the scattering enhancement and extinction efficiency, contributing to systematic differences in optical depth amplitude. The better agreement obtained under wet conditions supports the physical importance of this process.

The comparison pairs instantaneous model fields at H:00 with MERRA-2 hourly means representing roughly [H − 30, H + 30 min]. During periods of rapid-fire intensification or plume advection, this temporal mismatch further smooths and delays AOD peaks relative to modelled SOD maxima, manifesting as the apparent decoupling observed in the early afternoon hours.

The Mie-based SOD assumes spherical, monodisperse particles with fixed effective radius and density. Under extreme fire conditions, this simplification tends to overrepresent the number of small particles per unit mass, enhancing extinction near the fire front. This effect increases simulated SOD peaks but has minor influence on broader plume statistics, as confirmed by the microphysical sensitivity tests.

The optical diagnostics made quantify shortwave extinction, whereas wildfires emit intense longwave radiation that alters buoyancy and turbulence, promoting lofting and secondary aerosol formation. Such small-scale feedbacks are not explicitly resolved in MERRA-2, yet they modulate plume height and density and thus the spatial alignment of SOD and assimilated AOD.

The optical analysis presented above primarily concerns shortwave extinction (SOD/AOD). To place these results in context, it is essential to distinguish between the thermal radiation emitted by the fire itself and the attenuation of incoming solar radiation quantified by AOD and SOD. Fires emit thermal infrared radiation due to highly exothermic oxidation reactions involving biomass and oxygen. This thermal radiation is generated locally and contributes to atmospheric heating in the combustion zone. In contrast, AOD and SOD quantify the extinction of solar (shortwave) radiation caused by aerosol scattering and absorption and are therefore associated with changes in the atmospheric radiative balance induced by smoke particles, not with the direct release of energy from combustion.

The thermal radiation emitted by wildfires occurs primarily in the longwave (infrared) spectrum and can be expressed as a radiative flux (W m^{-2}). Although this longwave emission does not directly interact with incoming solar radiation, it significantly alters the local thermodynamic environment, enhancing plume buoyancy, promoting aerosol dispersion, and facilitating the formation of secondary aerosols. These processes indirectly influence the transmission of solar radiation by modifying the spatial and vertical distribution of scattering and absorbing aerosols. Thus, thermal radiation from fire plays a critical role in the radiative energy budget, both through its direct longwave component and through its indirect effects on shortwave radiative transfer via aerosol–radiation interactions.

Figure 9 shows the simulated PM2.5, and MERRA-2 BC, and OC mass concentrations at 19:00 UTC on 15 October 2017, corresponding to the mixed phase when the model–reanalysis agreement improved. The results reveal a strong spatial coherence between PM2.5 and its carbonaceous components, confirming that smoke particles are predominantly composed of black and organic carbon. As expected for biomass-burning emissions, OC concentrations greatly exceed BC, typically by an order of magnitude, indicating that the plume is dominated by smouldering-to-mixed combustion processes releasing large amounts of semi-volatile organic compounds that rapidly condense into fine-mode particles. These OC/BC ratios are consistent with previous field observations for Mediterranean wildfires.

The peak PM2.5 and OC concentrations are tightly co-located near the plume core, while BC shows a narrower and more confined distribution near the main fire front. This pattern reflects the combined effect of localized high temperature flaming combustion (source of BC) and broader downwind dispersion of condensable organics (source of OC). The model's 2 km horizontal resolution enables these fine-scale gradients to be resolved, unlike the coarser MERRA-2 (~50 × 70 km, hourly means), which smooths the maxima and blends plume and background air.

This structural contrast explains both the sharper peaks and stronger spatial gradients in the BRAMS–SFIRE results and the apparent desynchronization between modelled SOD and MERRA-2 AOD discussed earlier. At 19:00 UTC, however, the better spatial overlap between the simulated PM2.5, BC, and OC fields and the reanalysis aerosol load coincides with the improved optical coupling observed at this time.

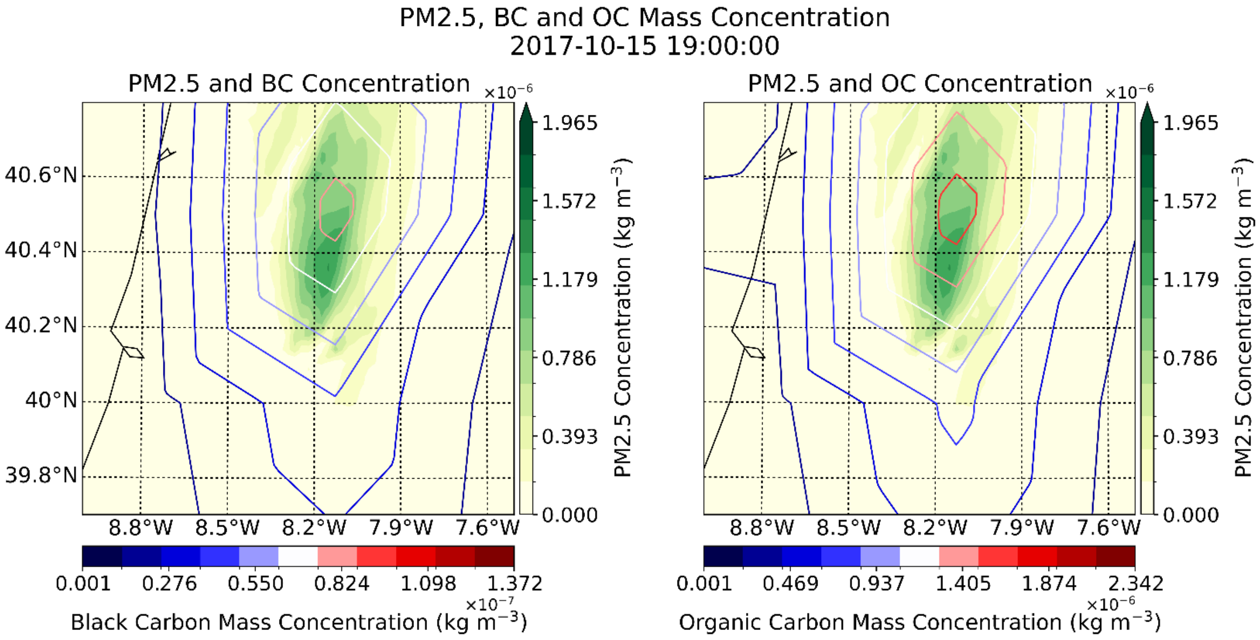

Figure 9: Spatial distribution of PM2.5concentrations (kg·m⁻³, contours) overlaid on BC (left panel) and OC (right panel) mass concentrations (kg·m⁻³, colour shading) at 19:00 UTC on 15 October 2017.

Figure 10 compares the simulated SOD at 550 nm with the MERRA-2 BC and OC extinction AOD during the mixed phase (18:00 UTC, 15 October 2017). As previously shown in Fig. 9, OC dominates the carbonaceous aerosol mass, while BC remains confined to the plume core near the main fire front. This compositional contrast is also evident in the extinction fields: OC extinction exhibits broader and stronger spatial correspondence with the simulated SOD, whereas BC extinction is weaker and more localized.

The 550 nm wavelength, commonly used in satellite retrievals, is particularly sensitive to fine-mode aerosol extinction and therefore well suited to represent the optical behaviour of the simulated smoke. The close structural agreement between SOD and OC extinction confirms that organic carbon is the principal contributor to the plume's visible-band radiative impact. In contrast, MERRA-2's coarse resolution smooths the sharp gradients resolved by BRAMS–SFIRE, attenuating peak extinction values and introducing slight spatial offsets.

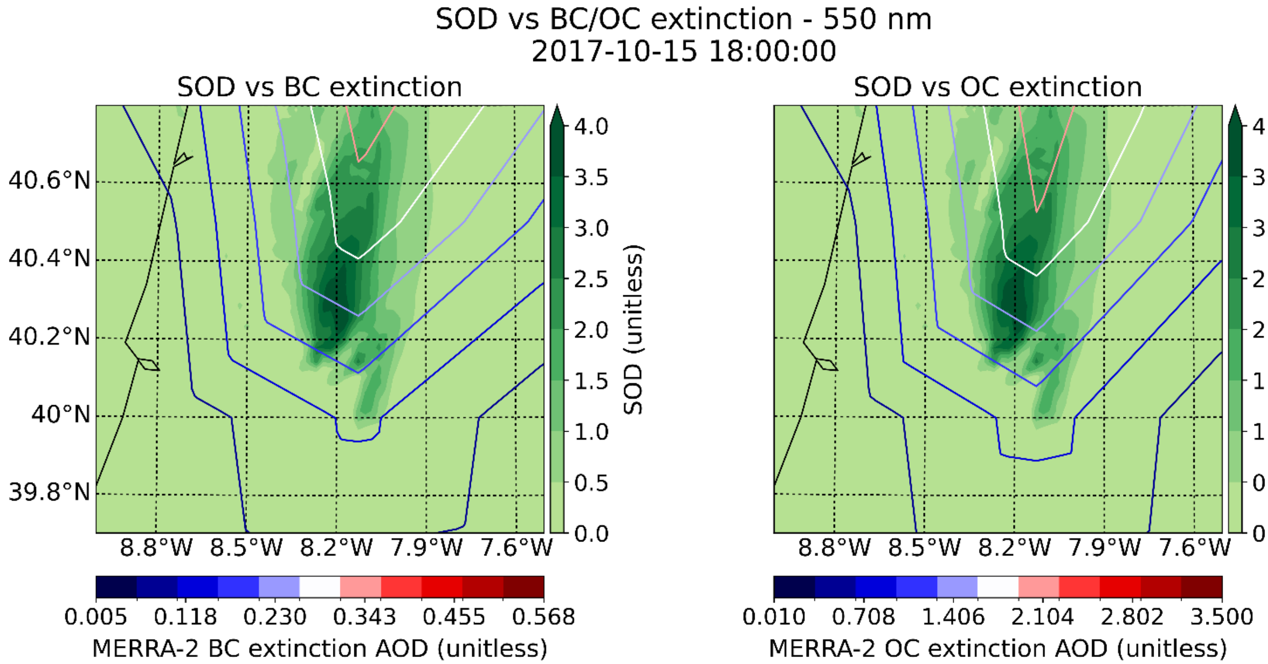

Figure 10: Comparison between simulated SOD (contours) and MERRA-2 extinction AOD at 550 nm for BC (left panel) and OC (right panel), at 18:00 UTC on 15 October 2017.

Figure 11 compares the model-diagnosed SOD with the MERRA-2 component extinction AOD at 19:00 UTC during the mixed phase: (a) BC and (b) OC. Only about 3% of the samples lie outside the plotting window (“clipped”), so truncation does not affect the conclusions.

In panel (a) (BC), the ordinary least-squares fit line blue has a very small slope (~0.07) and a positive intercept (0.03). The weak slope indicates that variability in SOD is only weakly expressed in the MERRA-2 BC extinction channel at this hour and over this domain. The positive intercept is consistent with a non-zero baseline in BC extinction (e.g., regional background and/or retrieval floor). The hexbin distribution is horizontally elongated relative to the 1:1 line, pointing to weak co-variation that can arise from species partitioning (BC being a minor contributor to total extinction in this case) and from spatial/temporal representativeness differences between the 2-km simulation and the ~50-km reanalysis.

In panel (b) (OC), the fit line blue y=0.44x+0.18 shows a much stronger sensitivity of OC extinction to SOD: for a unit increase in SOD, OC extinction increases ~6× more than BC. The sizeable intercept (~0.18) suggests a substantial background OC extinction and/or a systematic positive offset of the MERRA-2 OC channel relative to the model baseline. The upward-tilted scatter with hints of saturation at the upper end may reflect a combination of (i) dynamic-range limitations in the reanalysis OC product, (ii) sub-grid plume structure in the model that is diluted at reanalysis resolution, and (iii) differences in humidification growth or mixing-state assumptions between our κ–Köhler/Mie optical closure and MERRA-2.

Taken together, the two panels indicate a markedly stronger association between SOD and OC extinction than with BC extinction for this hour, while positive intercepts in both channels point to persistent background extinction. Any additional attribution (e.g., fire phase or cloud contamination) is not inferred here and would require independent diagnostics.

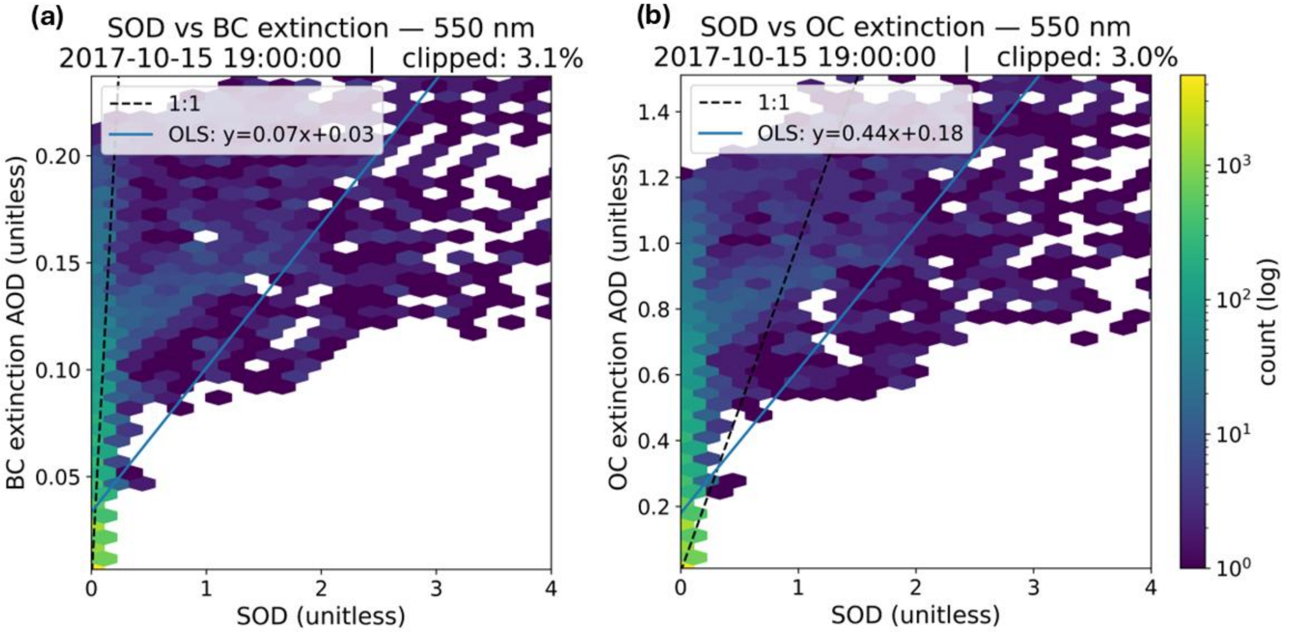

Figure 11: Scatter density plots comparing simulated SOD (wet) with MERRA-2 component extinction AOD for BC (panel a) and OC (panel b) at 550 nm, for 19:00 UTC on 15 October 2017. The dashed line represents the 1:1 relationship, and the solid line the ordinary least-squares (OLS) regression. Colour shading denotes the logarithmic density of grid-point pairs. The clipped percentage indicates the fraction of points excluded from the plot because their SOD or AOD values exceed the displayed range (≥ 4.0).

The statistical evaluation of simulated SOD against MERRA-2 component extinction AODs for black carbon (BC) and organic carbon (OC) is summarized in Table 5. The metrics quantitatively confirm the contrasting behavior already observed in Figs. 10–11, where BC exhibited weak spatial correspondence with SOD, while OC showed a much stronger and more coherent relationship.

For BC, all three microphysical configurations yield similar statistics, with mean SOD values (0.15–0.17) roughly three times higher than the corresponding MERRA-2 BC extinction (≈ 0.06). The positive bias (0.09–0.12) and moderate RMSE (0.82–0.94) reflect the weak contribution of BC to the total optical depth at 550 nm. Correlation coefficients remain low (r ≈ 0.23; ρ ≈ 0.75), and the regression slopes (~ 0.05) indicate that variations in BC extinction explain only a small fraction of the spatial variability in SOD. The small positive intercepts (~ 0.02–0.06) are consistent with a non-zero background BC extinction, likely representing regional baseline contributions and the limited dynamic range of the coarse-resolution MERRA-2 retrievals. The near-invariance of these metrics across the microphysical setups demonstrates that this weak SOD–BC linkage is structurally robust and largely insensitive to plausible variations in particle size distribution or hygroscopicity.

In contrast, the OC extinction field exhibits a markedly stronger and more proportional relationship with SOD. Mean OC extinction (~ 0.34) exceeds SOD by a factor of about two, resulting in a systematic negative bias (−0.16 to −0.18) and higher absolute errors (MAE ≈ 0.38–0.40). However, correlations are slightly higher (r ≈ 0.24–0.25; ρ ≈ 0.76), and the regression slope (~ 0.14) indicates a substantially greater sensitivity of OC extinction to SOD variability compared with BC (by almost a factor of three). The intercepts (~ 0.31–0.32) point to a persistent OC background or overestimation in MERRA-2, possibly related to climatological secondary organic aerosol loading and the coarse spatiotemporal averaging inherent to the reanalysis. The consistent slope and correlation across the three configurations further support the interpretation that OC dominates the visible-band extinction signature of the simulated plume.

The statistics corroborate that OC is the primary optical driver of the modeled smoke at 550 nm, while BC contributes only a minor, localized absorbing component. The weak dependence of both correlations on the assumed microphysical state (σ_g, κ and $r_{g,dry}$) demonstrates that compositional contrasts, rather than parameter uncertainty, control the observed behaviour. The combined results from the maps (Fig. 10) and scatter analyses (Fig. 11) thus confirm that the radiative impact of the plume is governed mainly by OC-dominated scattering, with BC absorption playing a secondary but spatially concentrated role within the fire core.

Table 5: Diagnostic statistics for all the Sertã wildfire period, including the mean, bias, mean absolute error (MAE), root-mean-square error (RMSE), Pearson correlation coefficient (r) and Spearman's rank correlation coefficient (ρ), and coefficient of determination (R^2), linear-regression slope and intercepts between SOD and BC, OC MERRA-2 extinction AOD.

Carbonaceous aerosols	Phase	Mean SOD	Mean BC/OC	Bias	MAE	RMSE	r	ρ	R^2	slope	intercept
BC	Baseline	0.16	0.06	0.10	0.19	0.85	0.23	0.75	0.05	0.022	0.056
	Concervative	0.17	0.06	0.12	0.20	0.94	0.23	0.75	0.05	0.019	0.056
	Lower envelope	0.15	0.06	0.09	0.18	0.82	0.23	0.75	0.05	0.022	0.056
OC	Baseline	0.16	0.34	-0.17	0.39	0.90	0.25	0.76	0.06	0.141	0.314
	Concervative	0.17	0.34	-0.16	0.40	0.97	0.24	0.76	0.06	0.126	0.315
	Lower envelope	0.15	0.34	-0.18	0.38	0.87	0.25	0.76	0.06	0.145	0.315

To assess the radiative implications of the simulated aerosol fields, the single scattering albedo (SSA) derived from BRAMS-SFIRE PM2.5 simulations, was compared with MERRA-2 data at 550 nm for 19:00 UTC (Fig. 12). SSA is a fundamental quantity in aerosol–radiation interaction studies, expressing the ratio of scattering to total extinction and thereby indicating the relative dominance of absorbing versus scattering components. Low SSA values denote strongly absorbing aerosols, typically associated with fresh BC-rich smoke, whereas high SSA values are characteristic of more scattering-dominated particles such as sulphates or aged organic aerosols.At 19:00 UTC, BRAMS-SFIRE simulates relatively high SSA values, ranging mostly between 0.88 and 0.90, with smoother spatial gradients across the plume region. This pattern indicates that the simulated smoke is dominated by moderately scattering aerosols, consistent with partial aging and mixing with less-absorbing species during transport. In contrast, MERRA-2 SSA derived from the BC+OC proxy (left panel) exhibits more spatial variability, including localized minima below 0.7 that suggest stronger absorption associated with freshly emitted black-carbon-rich particles.

The higher and more homogeneous SSA simulated by BRAMS-SFIRE likely results from rapid dilution and vertical mixing of the plume, as well as from simplifications in the representation of aerosol optical properties and internal mixing states.

When compared with MERRA-2 SSA derived from the total AOD (right panel), the differences between the datasets become more systematic. In this case, MERRA-2 eexhibits higher SSA values because the total AOD field includes additional aerosol components, such as sulphates and dust, that are predominantly scattering. Their inclusion enhances the overall scattering fraction in the reanalysis and smooths the horizontal gradients, yielding a more uniform spatial distribution of SSA. In contrast, the simulated field remains slightly lower and more structured, reflecting the localized influence of biomass-burning emissions. Despite these differences, both datasets consistently delineate the same general plume region, indicating that BRAMS-SFIRE realistically reproduces the spatial extent of smoke-affected areas.

These patterns are further quantified in Fig. 12, which presents scatter-density plots comparing simulated and MERRA-2 SSA for BC + OC and total aerosol components. The distributions reveal weak correlations and a narrow dynamic range, with most points concentrated near the upper SSA limit. The regression slopes strongly deviate from the 1:1 line, indicating that the model systematically overestimates SSA relative to MERRA-2, particularly for the BC + OC proxy. This behaviour reflects the combined influence of spatial-resolution differences, the coarse temporal averaging inherent to reanalysis data, and the simplified parameterization of refractive indices and mixing states in the model’s radiative module.

Taken together, Figs. 7–12 demonstrate that high-resolution fire–atmosphere models such as BRAMS-SFIRE can realistically reproduce the spatial structure and general radiative characteristics of smoke plumes. However, systematic biases in SSA magnitude and variability persist, emphasizing the need for further evaluation using temporally and spatially resolved ground-based and satellite observations to refine the model representation of aerosol optical properties and their radiative effects.

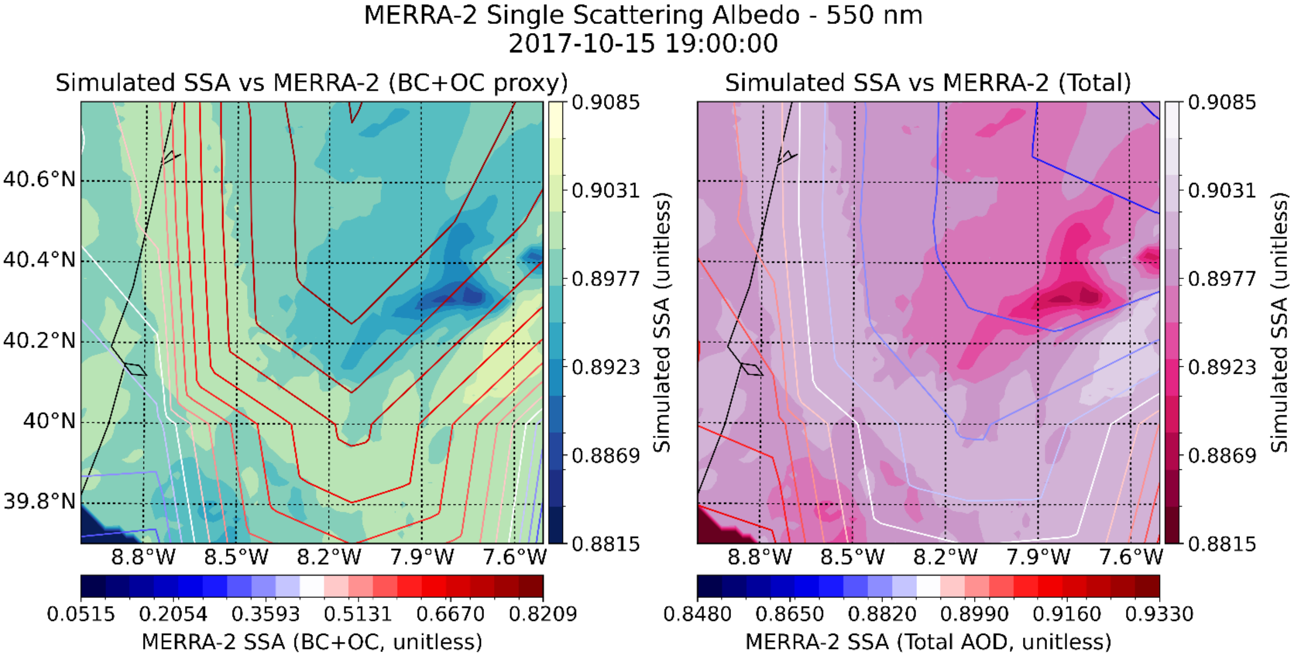

Figure 12: Spatial distribution of SSA at 550 nm derived from BRAMS-SFIRE PM2.5 simulations, overlaid with SSA contours derived from MERRA-2 reanalysis for the wildfire plume on 15 October 2017, at 19:00 UTC. Left panels show MERRA-2 SSA calculated from BC and OC AOD, while right panels represent SSA derived from total AOD (all species). 1245

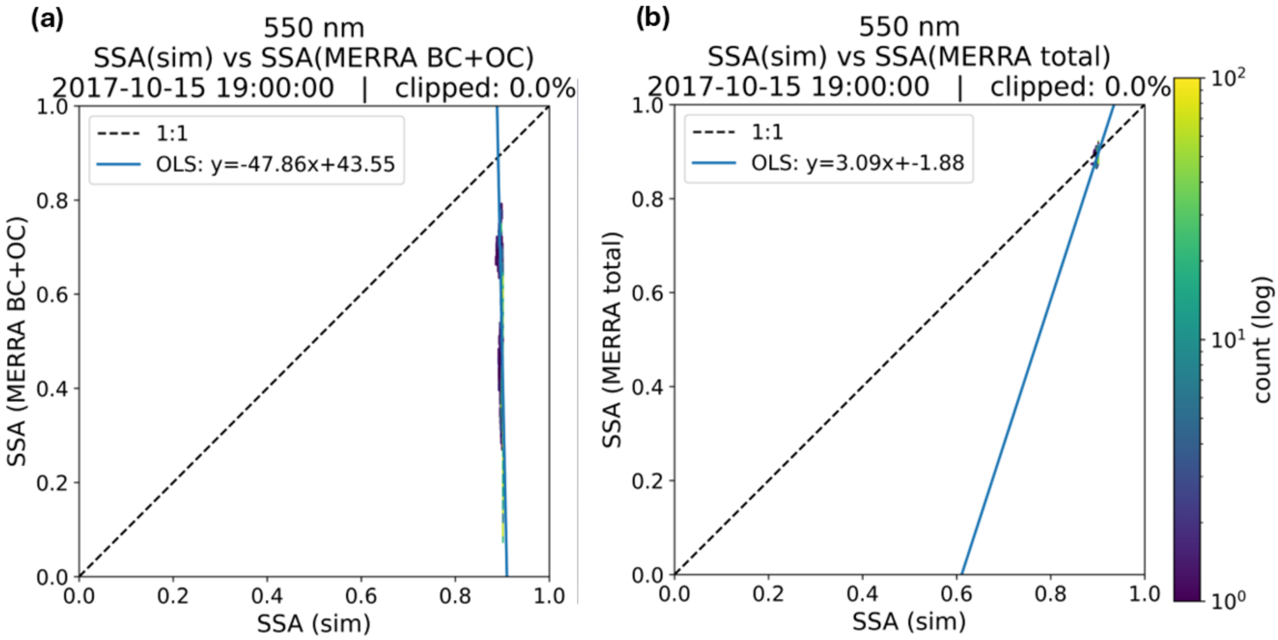

Figure 13: Scatter density plots comparing SSA derived from BRAMS-SFIRE PM2.5 simulations with MERRA-2 component AOD at 550 nm for BC + OC (panel a) and for total aerosols (panel b), at 19:00 UTC on 15 October 2017. The dashed line denotes the 1:1 relationship, while the solid line represents the ordinary least-squares (OLS) regression fit. Colour shading indicates the logarithmic density of grid-point pairs. The clipped percentage refers to the fraction of data points excluded from the plot because their SOD or AOD values exceed the displayed range (≥ 4.0).

The quantitative evaluation of SSA statistics (Table 6) corroborates the spatial patterns discussed above. When compared against MERRA-2 SSA derived from the BC + OC extinction AOD, the model exhibits a strong positive bias of ~0.36–0.37 across all microphysical configurations, indicating a substantial overestimation of the scattering fraction in the simulated smoke. The mean SSA simulated by BRAMS-SFIRE (≈ 0.90) contrasts sharply with the much lower MERRA-2 mean (≈ 0.54), consistent with the visual evidence in Figs. 12 and 14 showing that the model produces optically brighter, less absorbing plumes. The weak correlations (r ≈ –0.4 to 0.2) and near-zero regression slopes further confirm the limited point-to-point agreement, reflecting differences in spatial resolution, averaging timescales, and the simplified internal-mixing representation in the model's optical closure. The large positive intercepts (10–15) in the regression fits are purely numerical artefacts arising from the narrow SSA range and should not be interpreted physically.

In contrast, when the comparison is performed against the MERRA-2 total-aerosol SSA (all species combined), the agreement improves markedly. The bias is nearly eliminated (≈ +0.01), and the RMSE drops to ~0.02 across all configurations, while the correlations become weakly positive (r ≈ 0.3–0.5). This improvement is consistent with the inclusion in the MERRA-2 total SSA of predominantly scattering species such as sulphates and dust, which elevate the overall reanalysis SSA toward the modelled range. The close mean agreement suggests that, although BRAMS-SFIRE tends to overpredict SSA relative to the carbonaceous fraction alone, its bulk radiative behavior is broadly consistent with the multi-species aerosol environment captured by the reanalysis.

Physically, these results imply that the model reproduces the general radiative character of the plume, dominated by moderately scattering, partially aged smoke, but underrepresents the absorbing component associated with fresh BC. The consistency across the microphysical configurations (baseline, conservative, and lower envelope) indicates that these discrepancies are more structural than parametric, reflecting the inherent limitations of fixed refractive-index assumptions and unresolved sub-grid mixing processes.

Table 6: Diagnostic statistics for all the Sertã wildfire period, including the mean, bias, mean absolute error (MAE), root-mean-square error (RMSE), Pearson correlation coefficient (r) and Spearman's rank correlation coefficient (ρ), and coefficient of determination (R^2), linear-regression slope and intercepts between SSA derived from PM2.5 simulated by BRAMS–SFIRE and SSA derived from MERRA-2 extinction AODs (BC+OC and total aerosol components)

Carbonaceous aerosols	Phase	Mean simu	Mean MERRA-2	Bias	MAE	RMSE	r	ρ	R^2	slope	intercept
SSA BC+OC	Baseline	0.90	0.54	0.37	0.37	0.42	0.18	0.28	0.03	10.65	-9.07
	Concervative	0.90	0.54	0.37	0.37	0.42	-0.42	-0.25	0.18	-15.60	14.60
	Lower envelope	0.90	0.54	0.36	0.36	0.41	-0.40	-0.24	0.16	-10.83	10.24
SSA Total	Baseline	0.90	0.89	0.01	0.02	0.02	-0.31	-0.36	0.09	-1.59	2.32
	Concervative	0.90	0.89	0.01	0.02	0.02	0.47	0.33	0.22	1.58	-0.54
	Lower envelope	0.90	0.89	0.01	0.02	0.02	0.46	0.32	0.21	1.13	-0.13

3.3 Temporal Evolution and Distribution of PM2.5 Concentrations simulated

Figure 14 shows histograms of domain-wide near-surface PM2.5 concentrations (μg m^{-3}) at 13:00, 16:00, 19:00, and 22:00 UTC on 15 October 2017. The ordinate is the number of grid cells per bin on a logarithmic scale, with fixed bin edges across panels. Across all time steps, the distributions are strongly right-skewed, with a pronounced mode in the lowest bin and a persistent heavy tail reaching $\mathcal{O}(10^4)$ μg m^{-3}. The large count in the first bin indicates that most grid cells register very low concentrations (background or weakly impacted air), whereas the long upper tail shows that a comparatively small subset attains very high values. From 13:00 to 19:00 UTC the histograms broaden as counts shift from the lowest bin into intermediate and high bins ($\approx 10^2$—10^4 μg m^{-3}), evidencing increases in both spread and upper-tail occupancy. By 22:00 UTC the tail remains but the highest bins are less populated than at 19:00 UTC, while intermediate bins still retain substantial counts—consistent with partial dilution and aging rather than full clearing. In statistical terms, the fields exhibit pronounced positive skewness and persistent heavy-tailed (non-Gaussian) behavior into the evening, alongside an afternoon increase in the fraction of the domain experiencing elevated concentrations.

Scientifically, the coexistence of a dominant low-concentration mode with a persistent heavy tail indicates a smoke influence that is spatially sparse yet intense where present. The relatively limited footprint and sporadic high values at 13:00 UTC transition, by 16:00–19:00 UTC, to greater occupancy of mid-to-high bins, which is consistent with plume intensification and lateral spread associated with daytime mixing and peak fire activity. Toward evening (22:00 UTC), reduced surface heating and weaker turbulence are consistent with the partial relaxation of extremes near the surface, while the continued tail suggests that pockets of high PM2.5 persist locally. Operationally, regional exposure is governed by a small fraction of grid cells bearing very high PM2.5, whereas the majority of the area remains lightly affected, implying sharp spatial gradients and transient hotspots that evolve through the afternoon and can carry into the evening.

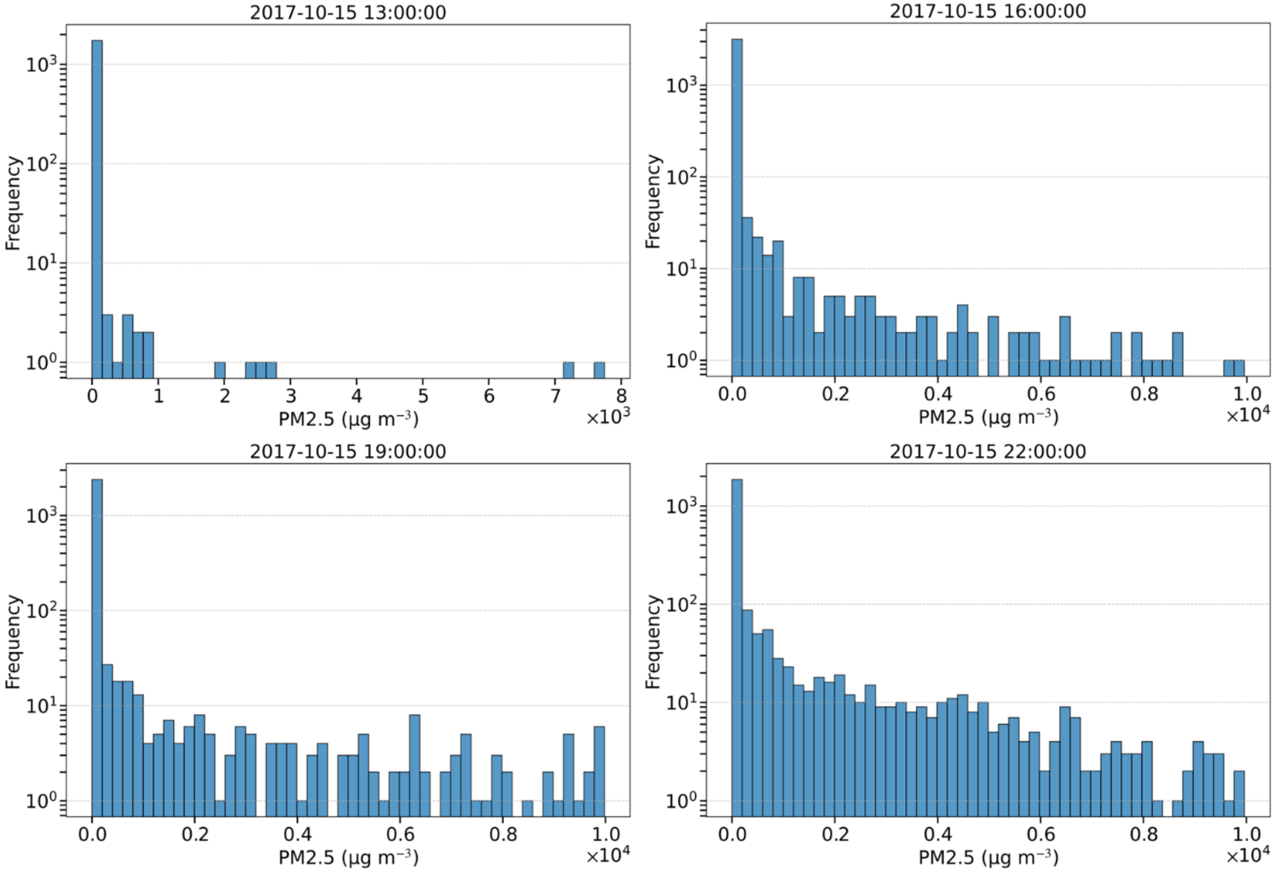

Figure 14: Frequency distribution of PM2.5 concentrations (μg/m³) across the simulation domain on 15 October 2017 at different hours (13:00, 14:00, 19:00 and 22:00 UTC). Each histogram shows the number of grid cells registering PM$_{2.5}$ values within each concentration bin. The vertical axis is plotted on a logarithmic scale to highlight rare but extreme values.

At 19:00 UTC, the histogram in Fig. 15 further emphasizes the strongly right-skewed nature of the PM2.5 distribution. After restricting the analysis to values below 10^4 μg m^{-3}, the majority of grid cells remain below 0.1 μg m^{-3}, while a small subset occupies the upper bins, forming a sparse heavy tail that approaches the imposed cutoff. The persistence of this tail under a physically motivated cap suggests localized accumulation near the fire core, while the filtering simultaneously suppresses unrealistically large extremes likely attributable to numerical artifacts. This yields a more physically interpretable depiction of the simulated PM2.5 field and clarifies that domain-wide exposure at 19:00 UTC is still governed by a small fraction of cells at the high end.

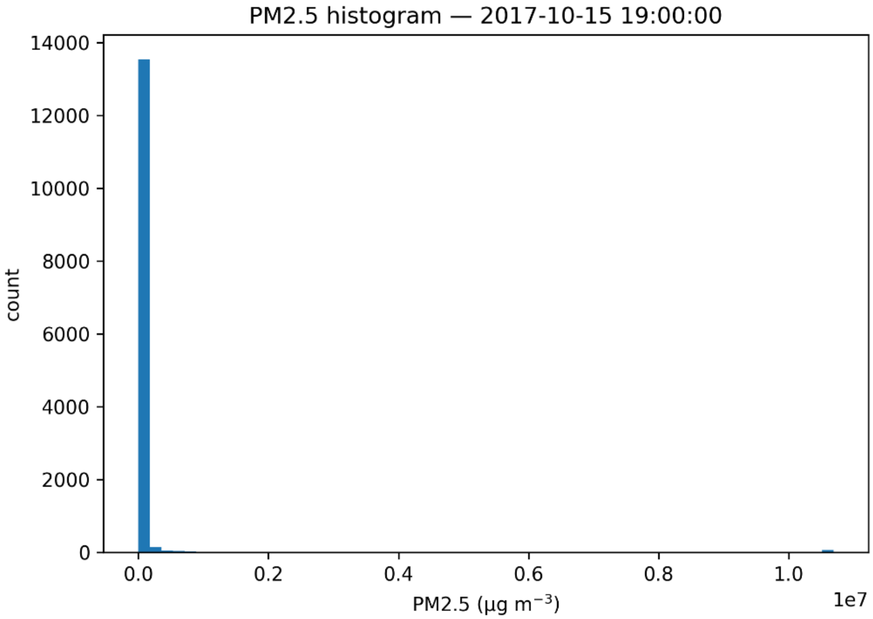

Figure 15: Histogram of PM2.5 concentration (μg/m³) across the simulation domain at 19:00 UTC on 15 October 2017.

3.4 Atmospheric Stability and Thermodynamic Modulation by Aerosol–Radiation Interactions in Wildfire Events

Atmospheric stability is primarily governed by the vertical temperature gradient, or lapse rate. The behaviour of an air parcel depends on how rapidly it cools adiabatically compared to the ambient temperature profile. If a rising parcel cools more slowly than the environment, it becomes less dense and buoyant, accelerating upward. Conversely, if it becomes denser than the surrounding air, it will descend. When vertical displacements of air parcels are amplified by buoyancy forces, the atmosphere is considered unstable, favouring convection, cloud formation, and potentially severe weather. In contrast, if the parcel is cooler and denser than its environment, vertical motion is suppressed, indicating a stable atmosphere.

Stability is evaluated by comparing the environmental lapse rate with the theoretical adiabatic lapse rates: the Dry Adiabatic Lapse Rate (DALR ≈ 9.8 K km^{-1}) and the Moist Adiabatic Lapse Rate (MALR, typically 4–7 K km^{-1}, depending on humidity). Strongly stable conditions are found during temperature inversions, where temperature increases with altitude. These often occur near the surface at night or under large-scale subsidence, resulting in a subsidence inversion typically between 1–3 km altitude. Such inversions act as barriers to vertical mixing and are crucial for air pollution accumulation.

When moist air parcels rise, they initially follow the DALR until reaching the Lifting Condensation Level (LCL), where condensation begins. The release of latent heat during condensation (an exothermic process) partially offsets adiabatic cooling, increasing the parcel's buoyancy and shifting it to follow the MALR. If sufficient energy is available, the parcel reaches the Level of Free Convection (LFC) and may continue to ascend to the Equilibrium Level (EL), near the tropopause.

The atmospheric layer closest to the surface is the Planetary Boundary Layer (PBL), where turbulence and mixing are most pronounced due to surface heating and friction. The structure and height of the PBL vary diurnally and are strongly influenced by radiative forcing and atmospheric stability. During the daytime, especially in wildfire regions, intense surface heating and smoke-induced turbulence may erode stable layers, promoting deep mixing.

These vertical motions have significant implications for aerosol dispersion. In stable conditions, especially under inversions, particulate matter accumulates near the surface due to suppressed mixing. Under unstable, convective conditions, particles are efficiently mixed and vertically transported.

CAPE quantifies the potential energy that a rising air parcel can convert into kinetic energy if lifted adiabatically. Higher CAPE values suggest stronger updrafts and a greater likelihood of convective development, enhancing vertical mixing and pollutant dispersion. CIN, on the other hand, represents the energy barrier that must be overcome for a parcel to initiate free convection. Large CIN values suppress vertical motion and contribute to the accumulation of pollutants and aerosols near the surface.

The regions impacted by these two energy terms are bounded by two key levels: the LFC and the EL. Below the LFC, the parcel is cooler than its environment, requiring energy input to rise—this energy defines the CIN. Above the LFC, the parcel is positively buoyant, contributing to CAPE. These estimates often assume pseudo-adiabatic processes (no entrainment and removal of condensed water), allowing latent heat release to maintain saturation.

In wildfire scenarios, evaluating CAPE and CIN become particularly relevant for assessing pyroconvection. Wildfires inject substantial heat and moisture into the atmosphere, potentially reducing local CIN (by warming the PBL) and allowing parcels to reach their LFC. When background CAPE is significant, this can trigger the formation of convective clouds (flammagenitus or pyrocumulus), and in extreme cases, deep convective events such as pyroCb (pyrocumulonimbus). Studies have shown that intense fire heat fluxes increase CAPE and reduce CIN, facilitating the vertical transport of smoke and the development of fire-induced storms.

In addition, turbulent fluxes generated by rising air parcels and plume dynamics influence pollutant dispersion. Parcels moving upward often carry higher aerosol concentrations, resulting in well-defined plume cores. This distribution can often be approximated by Gaussian profiles in horizontal cross-sections, in agreement with Fick's law of diffusion, where the diffusion flux is proportional to the gradient in species concentration.

The interaction of aerosol particles with radiation is governed by two fundamental optical processes: scattering and absorption. Scattering occurs when incident electromagnetic radiation is redirected by particles. In the case of Mie scattering, relevant when the particle diameter is comparable to the wavelength of the incident radiation, light penetrates the particle, and the internal refractive index gradients cause the redirection of light. OC aerosols, being efficient scatterers, predominantly affect shortwave (SW) radiation in the visible spectrum.

Absorption involves the uptake of photon energy by electrons in the atoms or molecules of the aerosol particle. The absorbed energy excites electrons to higher energy levels, and as they relax to their ground states, the energy is primarily dissipated through non-radiative processes, increasing the internal kinetic energy of the particle. This manifests macroscopically as thermal heating of the particle, i.e., the conversion of radiant energy into thermal energy. BC is a strong absorber in the visible and near-infrared spectra and significantly contributes to atmospheric heating.

While both OC and BC interact with radiation in the UV–visible range (0.3–0.7 µm), the direct radiative effect of aerosols on longwave (LW) radiation is generally weaker than that on shortwave (SW) radiation.

The absorption of SW radiation by BC-rich aerosol layers elevates local temperatures, promoting thermal stability. This may lead to or enhance thermal inversions, thereby increasing CIN and inhibiting convection and cloud formation. In contrast, OC scattering reduces incoming SW radiation, cools the surface and reducing the vertical temperature gradient. This cooling may decrease CAPE, reducing the buoyant energy available for upward motion.

This thermodynamic modulation by aerosol–radiation interactions is further illustrated in Fig. 16, which presents the differences in shortwave (SW) and longwave (LW) downwelling surface radiative fluxes between simulations with and without fire at 19:00 and 20:00 UTC on 15 October 2017. In these maps, positive values (light pink in SW and light green in LW panels) correspond to No Fire – Fire > 0, indicating a reduction in surface irradiance caused by smoke and fire. Conversely, negative LW differences (darker green areas) reflect enhanced downwelling longwave radiation in the presence of fire, largely driven by thermal re-emission from the smoke plume and, to a lesser extent, by cloud or haze formation.At 19:00 UTC (Figs. 16a–b), shortwave fluxes are markedly reduced, locally exceeding –500 W m^{-2}, over the main smoke-affected region, evidencing strong attenuation of solar radiation by dense aerosol layers. Simultaneously, an increase in downwelling LW flux of up to +60 W m^{-2} emerges near the plume core, suggesting an active radiative trapping mechanism: smoke particles absorb and re-emit thermal radiation, effectively creating a localized greenhouse effect that limits surface cooling.By 20:00 UTC (Figs. 16c–d), the magnitude of the SW deficit remains substantial but becomes spatially more confined, while the LW enhancement persists, closely aligned with areas of maximum column smoke absorption. This pattern indicates sustained radiative heating within the smoke layer and continued suppression of nocturnal cooling beneath it.

These results confirm that smoke acts simultaneously as a solar radiation attenuator and an infrared emitter. The resulting energy imbalance strengthens static stability within the boundary layer and reinforces the “radiative lid” effect previously discussed, whereby the combination of reduced shortwave input and enhanced longwave back-emission stabilizes the lower atmosphere, inhibits vertical mixing, and prolongs the persistence of smoke near the surface.

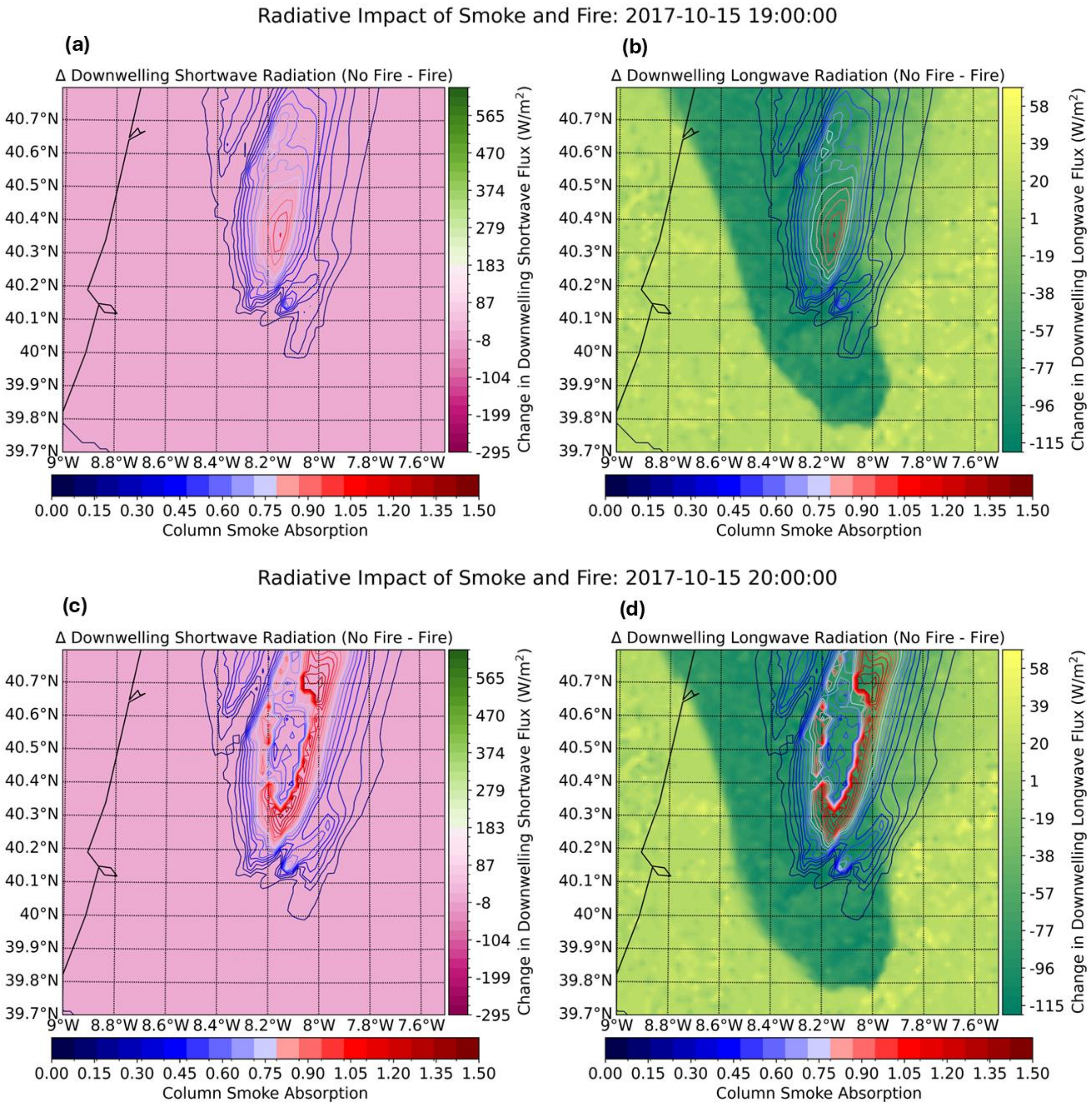

Figure 16: Difference in shortwave and longwave surface radiative fluxes between simulations with and without fire, at 19:00, and 20:00 UTC on 15 October 2017. Positive values in the shortwave and longwave flux difference maps (light pink/light green) indicate a reduction in radiation due to the presence of smoke and fire. Negative longwave values (darker green shades) suggest an increase in downward radiation, potentially associated with thermal re-emission from the smoke plume or cloud formation. Coloured contour lines represent fire-weighted smoke absorption, indicating regions where smoke exerted the strongest radiative influence.

Figs. 17–19 show longitudinal cross-sections of the smoke extinction (SEC) and absorption (SAC) coefficients at 550 nm simulated by BRAMS-SFIRE under CAPE and CIN conditions along 8.1° W, for 15 October 2017. Colour shading represents the magnitude of the extinction and absorption coefficients, while CAPE and CIN isolines are superimposed: solid black contours denote the fire simulation, and dashed red contours correspond to the no-fire case. The left-hand panels ("under CAPE conditions") depict the same optical fields but without CAPE isolines, as CAPE values were zero throughout the plotted vertical range (~0–1.2 km) and were therefore omitted for clarity.

At 15:00 UTC and 550 nm (Fig. 17), a compact and optically dense smoke layer is confined to the lowest 300–500 m. Extinction and absorption maxima are tightly collocated near ~40.0° N, indicating a freshly emitted, BC/OC-rich plume. In the CIN panels, the fire-run isolines (black) appear elevated relative to the no-fire run (red) over the plume core, evidencing a local weakening of the inversion and reduced inhibition consistent with shortwave heating by absorbing smoke.

By 19:00 UTC and 550 nm (Fig. 18), the smoke layer has deepened and become more vertically diffuse, extending intermittently up to ~1 km. Although the plume has partially dispersed, the CIN isolines in the fire run remain higher than in the no-fire case between 39.9° N and 40.1° N, confirming a persistent thermodynamic perturbation induced by radiative heating. The co-location of enhanced SEC/SAC values with elevated CIN indicates continued warming by aged, lofted smoke. The vertical expansion of the absorbing layer at this stage reflects active turbulent mixing and upward redistribution of radiative energy, which contributes to a more stable layer near the surface and reduced convective coupling above.

At 19:00 UTC and 700 nm (Fig. 19), both SEC and SAC are systematically weaker than at 550 nm, SAC decreases by roughly a factor of 2–3, and SEC by ~30–40 %, yet the vertical–meridional structure and the uplift of CIN isolines over the smoke footprint remain clearly discernible. This spectral attenuation is consistent with the reduced optical efficiency at longer wavelengths for mixed BC–OC smoke (including brown carbon) and with progressive chemical ageing and dilution of the aerosol population.At 400 nm, both extinction and absorption coefficients are substantially higher than at 550 nm and 700 nm. Peak SEC values reach approximately 3.3×10^{-2} m^{-1}, compared with ~2.3×10^{-2} m^{-1} at 550 nm, while SAC increases to nearly 6×10^{-3} m^{-1}, about twice that at 550 nm. The enhancement is concentrated within the lowest 500–800 m, coinciding with the core of the smoke layer and the region of elevated CIN in the fire simulation. This spectral behaviour is fully consistent with the optical properties of organic and brown-carbon aerosols, which exhibit stronger scattering and absorption in the UV–blue region. The higher coefficients at 400 nm highlight the enhanced radiative sensitivity of shorter wavelengths to OC-dominated smoke, underscoring the wavelength dependence of aerosol–radiation interactions and their role in modulating heating rates within the lower troposphere.

1430

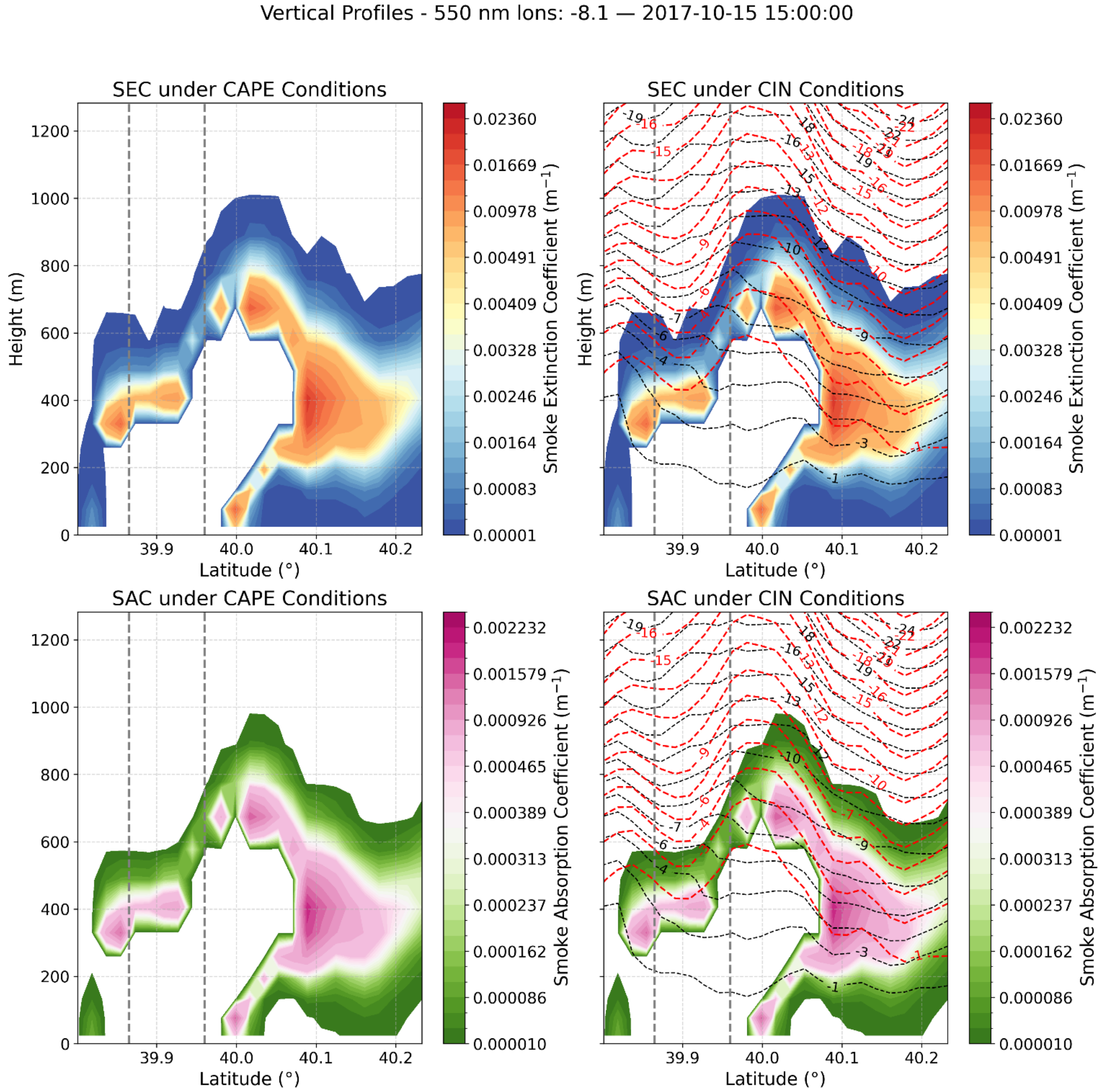
Vertical Profiles - 550 nm lons: -8.1 — 2017-10-15 15:00:00
SEC under CAPE Conditions
SEC under CIN Conditions
SAC under CAPE Conditions
SAC under CIN Conditions
Height (m)
Latitude (°)
Smoke Extinction Coefficient (m^{-1})
Smoke Absorption Coefficient (m^{-1})
0
200
400
600
800
1000
1200
39.9
40.0
40.1
40.2
0.02360
0.01669
0.00978
0.00491
0.00409
0.00328
0.00246
0.00164
0.00083
0.00001
0.002232
0.001579
0.000926
0.000465
0.000389
0.000313
0.000237
0.000162
0.000086
0.000010

Figure 17: Longitudinal cross-sections of smoke extinction and absorption coefficients at 550 nmalong 8.1° W, under CAPE and CIN conditions. Dashed black lines indicate the fire simulation, while dashed red lines represent the no-fire scenario, at 15:00 UTC on 15 October 2017. The region enclosed between the two light gray dashed vertical lines represents the observed area affected by the wildfire.

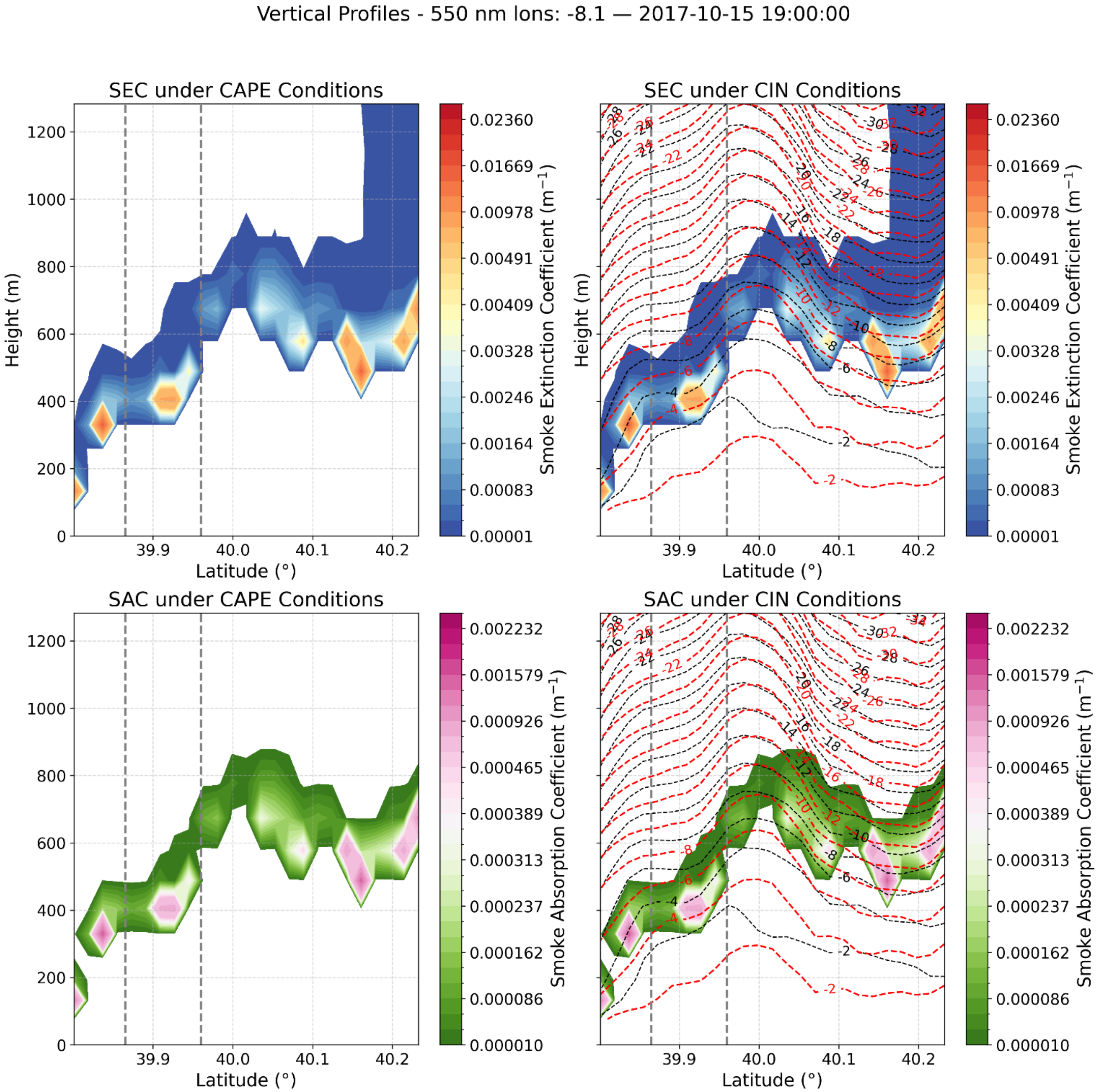

Figure 18: Longitudinal cross-sections of smoke extinction and absorption coefficients at 550 nm and 700 nm along 8.1° W, under CAPE and CIN conditions. Dashed black lines indicate the fire simulation, while dashed red lines represent the no-fire scenario, at 19:00 UTC on 15 October 2017. The region enclosed between the two light gray dashed vertical lines represents the observed area affected by the wildfire.

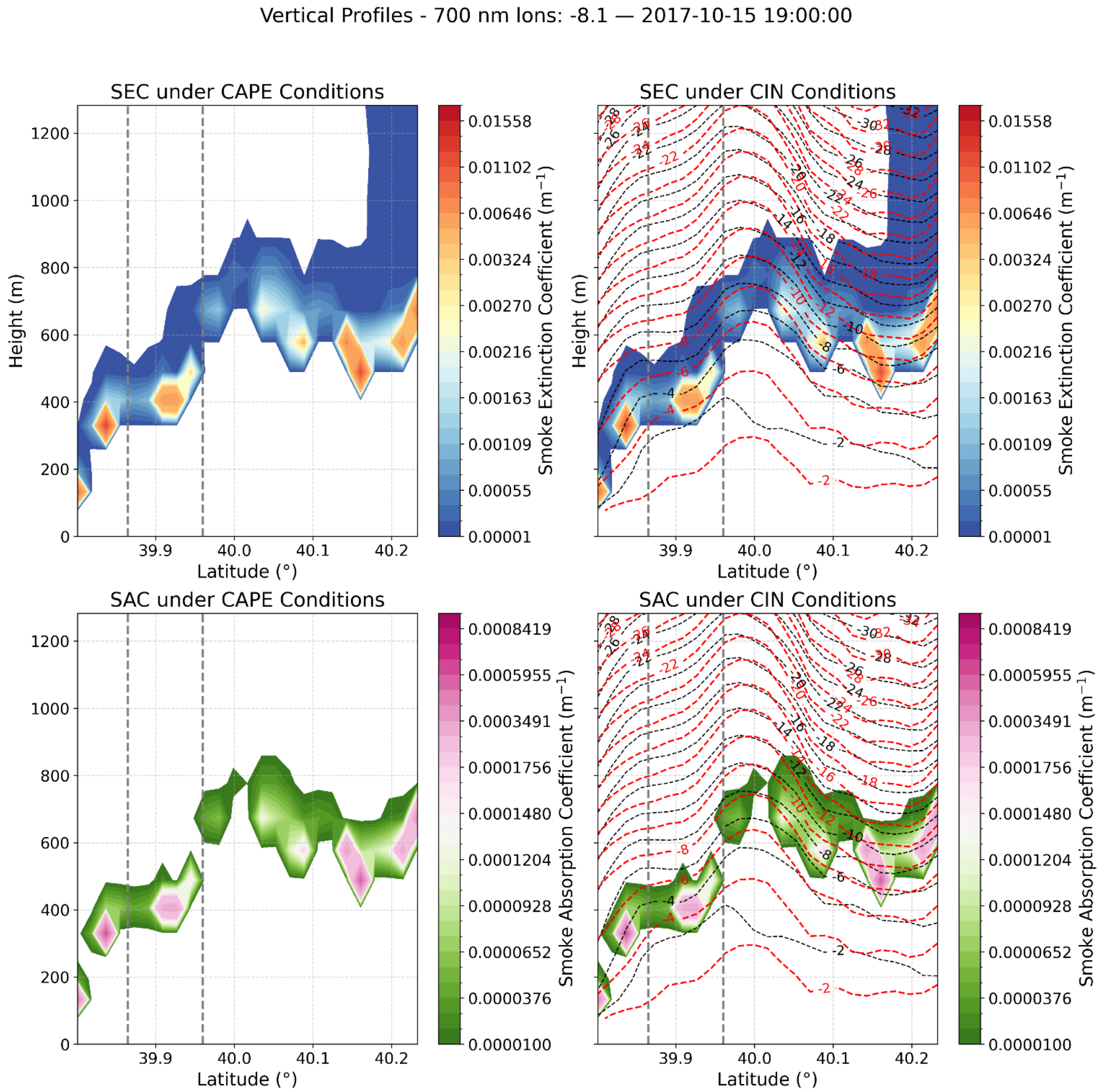

Figure 19: Longitudinal cross-sections of smoke extinction and absorption coefficients at 700 nm along 8.1° W, under CAPE and CIN conditions. Dashed black lines indicate the fire simulation, while dashed red lines represent the no-fire scenario, at 19:00 UTC on 15 October 2017. The region enclosed between the two light gray dashed vertical lines represents the observed area affected by the wildfire.

Building upon the previously described vertical redistribution of CAPE and CIN in the presence of smoke, further insights emerge from the detailed analysis of inversion-layer dynamics under varying radiative conditions. The combined evaluation of extinction and absorption coefficients with potential temperature and relative humidity fields (Fig. 20-23) demonstrates that smoke-induced radiative perturbations not only modulate static stability but also actively reshape the structure and persistence of inversion layers.

At 15:00 UTC (Fig. 20), shortly after the onset of peak fire activity, the smoke extinction and absorption coefficients at 550 nm already show clear radiative impacts near the inversion base. Localized heating beneath the inversion results in systematic lifting and partial weakening of the layer compared to the no-fire control, with displacements of roughly 100–150 m. The vertical gradient of potential temperature becomes less pronounced in smoke-affected sectors, indicating early signs of sub-inversion destabilization.

By 19:00 UTC (Fig. 21), these effects intensify: the inversion is further elevated and spatially modulated by concentrated smoke layers. Enhanced absorption coincides with regions of strong extinction near 400–700 m a.g.l., suggesting sustained radiative heating capable of eroding the inversion top and promoting vertical mixing. This restructuring supports the presence of a radiative lid mechanism in which heating beneath the inversion reduces thermal contrast while facilitating upward aerosol transport.

Comparative analysis across wavelengths at 19:00 UTC reinforces the spectral sensitivity of this process. At 400 nm, extinction and absorption maxima are more pronounced and vertically extensive, consistent with the stronger interaction of UV–blue radiation with fine-mode organic carbon aerosols. Conversely, at 700 nm, the response is more subdued, with lower coefficients and smaller vertical displacements, highlighting the reduced efficiency of longer wavelengths in modulating the inversion thermodynamics.

Collectively, these results demonstrate that smoke layers act as dynamically active radiative agents capable of altering inversion height, intensity, and continuity. The interplay between localized absorption-driven heating and weakened thermal gradients enhances entrainment at the plume–inversion interface, contributing to mesoscale thermodynamic adjustments and spatial heterogeneity in boundary-layer stability. Such radiative–dynamic coupling underscores the capacity of smoke to modify near-surface stratification and to induce feedbacks on vertical transport processes well beyond the immediate fire area.

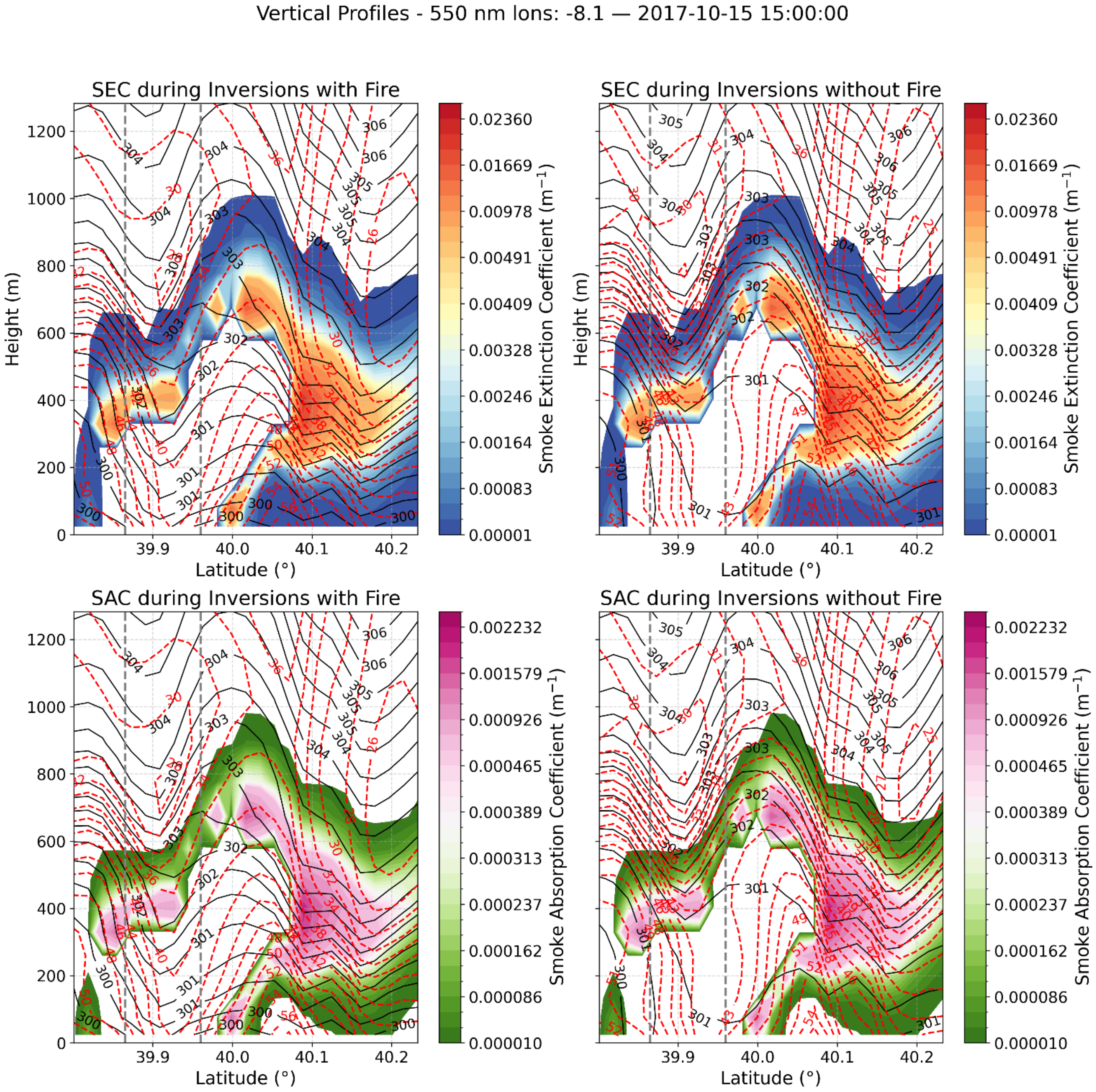
Vertical Profiles - 550 nm lons: -8.1 — 2017-10-15 15:00:00
SEC during Inversions with Fire
SEC during Inversions without Fire
SAC during Inversions with Fire
SAC during Inversions without Fire
Height (m)
Latitude (°)
Smoke Extinction Coefficient (m⁻¹)
0.02360
0.01669
0.00978
0.00491
0.00409
0.00328
0.00246
0.00164
0.00083
0.00001
Smoke Absorption Coefficient (m⁻¹)
0.002232
0.001579
0.000926
0.000465
0.000389
0.000313
0.000237
0.000162
0.000086
0.000010
0
200
400
600
800
1000
1200
39.9
40.0
40.1
40.2

Figure 20: Longitudinal cross-sections of inversion layers overlaid with smoke extinction and absorption coefficients at 550 nm along 8.1° W. Dashed red lines indicate relative humidity (%), and solid black lines represent potential temperature (K). Simulations correspond to 15:00 UTC on 15 October 2017. The region enclosed between the two light gray dashed vertical lines represents the observed area affected by the wildfire.

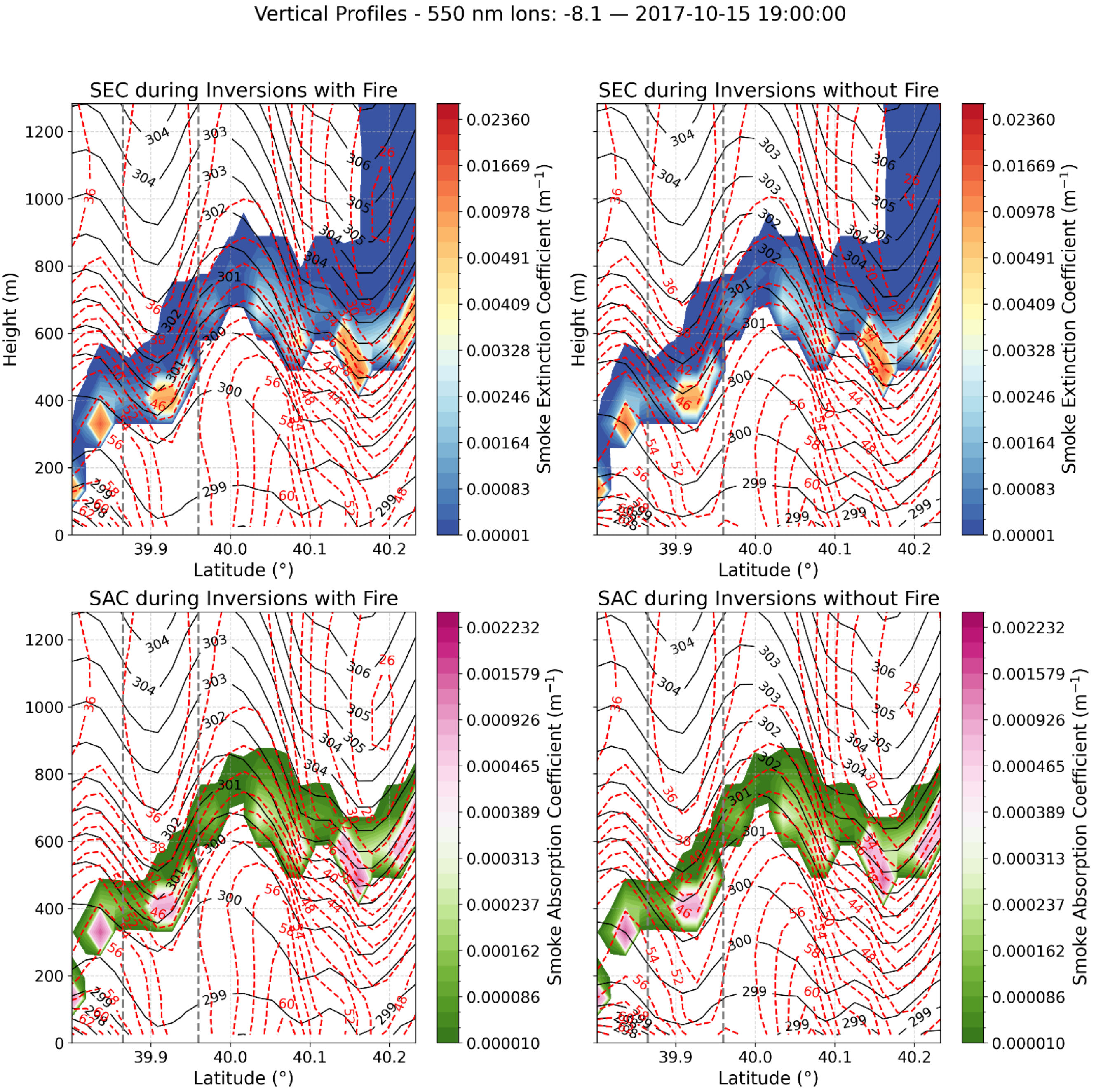

Figure 21: Longitudinal cross-sections of inversion layers overlaid with smoke extinction and absorption coefficients at 550 nm along 8.1° W. Dashed red lines indicate relative humidity (%), and solid black lines represent potential temperature (K). Simulations correspond to 19:00 UTC on 15 October 2017. The region enclosed between the two light gray dashed vertical lines represents the observed area affected by the wildfire.

4 Conclusion

The combined results demonstrate that the BRAMS–SFIRE framework, with explicit smoke–radiation coupling, successfully reproduces the coupled optical and thermodynamic responses of the atmosphere to intense wildfire emissions. The simulations for 15 October 2017 capture both the spectral behaviour and vertical thermodynamic restructuring induced by smoke. Enhanced shortwave absorption at 400–700 nm and localized longwave re-emission generated radiative caps that inhibited nocturnal cooling and displaced Convective Inhibition (CIN) layers upward by 100–200 m. Concurrently, Convective Available Potential Energy (CAPE) increased locally, indicating the onset of radiative–convective feedbacks. These features align with the observed diurnal evolution of stability and corroborate the role of smoke heating in modifying boundary-layer dynamics and inversion strength.The comparison between simulated Smoke Optical Depth (SOD) and MERRA-2 Aerosol Optical Depth (AOD) confirms that the apparent amplitude and phase differences mainly reflect the distinct spatiotemporal resolutions and underlying physical quantities of both datasets. The model resolves fine-scale and freshly emitted plumes, whereas MERRA-2 provides a smoothed composite representing multiple aerosol sources. Despite these differences, the simulations consistently reproduce the main spatial structure and timing of the observed plume, with the wet configuration yielding the most realistic optical depths, particularly during the mixed phase (18:00–20:00 UTC)..Diagnostic statistics (Tables S1–S3) show that background subtraction based on upwind AOD systematically improves agreement, reducing biases from −0.7 to −0.05 and increasing correlation coefficients ($r \approx 0.16$–0.17; $\rho \approx 0.58$). Percentile-based masks (P70–P90) isolate the plume core and confirm that microphysical perturbations, including ABSORBING-like, WIDE SIGMA, and scaled $r_{g,dry}$, produce only modest deviations, reinforcing the robustness of the optical parameterizations.

At 19:00 UTC, the spatial and spectral consistency between SOD and AOD is maximized. Composition maps and extinction profiles reveal that OC-dominated fine-mode aerosols govern the smoke optical depth at 550 nm, while BC contributes disproportionately to localized heating and inversion strengthening. The combination of hygroscopic growth, carbonaceous fine-mode dominance, and longwave trapping explains why this phase reproduces both the optical and thermodynamic structure of the plume most realistically.

Overall, the model reproduces the interlinked optical–radiative–thermodynamic feedback characteristic of large fire plumes: enhanced absorption, inversion reinforcement, CIN displacement, and CAPE modulation. These findings confirm that the implemented microphysical and radiative schemes are physically consistent and that residual discrepancies with MERRA-2 primarily arise from intrinsic resolution and smoothing differences.

The BRAMS–SFIRE coupling thus provides a physically grounded framework for diagnosing wildfire-induced radiative perturbations and their impacts on atmospheric stability. Notably, the inclusion of crown fire modelling in BRAMS offers enhanced realism in forested and mountainous regions where canopy combustion substantially increases the heat release and aerosol injection heights.

Future work will extend this approach to multi-event climatological analyses and refined aerosol aging processes, further consolidating its potential as a predictive and diagnostic tool for fire–atmosphere interactions under changing climate conditions.

Table 1—Symbols and variables used in the text.

Symbol	Definition	Unities
$R_{surface}$	Surface fire spread	m s^{-1}
$R_{initialization}$	Equivalent rate of spread	m s^{-1}
R_{active}	Active crown fire spread set to 40 % of the observed 6.1-meter windspeed at midflame height	m s^{-1}
R_{10}	Surface fire spread rate for fuel behavior model 10	m s^{-1}
$R_{back_{10}}$	backing spread for fuel behavior model 10	m s^{-1}
$R_{wind_{10}}$	Spread rate dew to wind factor for fuel behavior model 10	m s^{-1}
$R_{slope_{10}}$	Spread rate dew to slope factor for fuel behavior model 10	m s^{-1}
R_{final}	Total fire spread	m s^{-1}
$I_{initialization}$	Fireline intensity of the surface fire	W m^{-1}
$I_{r_{10}}$	Reaction intensity for NFFL fuel behaviour model 10	W m^{-1}
I_{final}	Fire intensity, accounting for the integration between the shrub/herbaceous layer and the tree canopy	W m^{-1}
ϕ	Fire energy flux	W m^{-2}
H	The heat yield of the fuel corresponds to the mass of fuel consumed in the flaming front	kJ m^{-2}
H_{Low}	Lower heat content of the fuel	kJ kg^{-1}
t_r	Residence time for the same model	
σ_{10}	Surface-area-to-volume ratio for fuel behavior model 10	
$w_{surface}$	Represents the initial total mass of surface fuel	kg m^{-2}
FMC	Foliar moisture content	%
FME	Foliar moisture effect	
FME_0	FME to a reference value established for an FMC of 100%	
CFB	Crown fraction burned	
P	Radiative power	MW

ϵ	Emissivity	
σ	Stefan-Boltzmann constant	W (m^2 K^4)$^{-1}$
A	Burnt area	m^2
T	Temperature	K
Qs	Sensible heat flux	W m^{-2}
c	Specific heat capacity for dry wood	J (kg K)$^{-1}$
m	Mass of the burned material	kg

Code availability

The version of the BRAMS model used to produce the results presented in this paper is available under the Creative Commons Attribution 4.0 International License on https://zenodo.org/records/15830137 (CPTEC/INPE, 2025), along with compilation and simulation instructions.

Author contribution

ICM and LFR developed the coupling within the BRAMS model. ICM also designed the presented experiments, performed the validation, produced the figures and analysis, and wrote the original manuscript. KML and SRF guided the conceptualisation of the coupling implementation in BRAMS. MFF supported the development by correcting conceptual coding errors and assisting with model compilation. RB, VFO, and SC created supporting files for the simulations. In addition, SC contributed to the manuscript review. AIM reviewed the manuscript and supervised the conceptualisation of the model's application.

Competing interests

The authors declare that they have no conflicts of interest associated with this publication and that no financial support has influenced the outcomes of this work.

Acknowledgements

The developments presented in this study were carried out within the FIRESMOKE project, a collaborative effort between the National Institute for Space Research (INPE), in Brazil, and the University of Aveiro, in Portugal. They include the integration of crown fire dynamics and the coupling of fire-emitted aerosols with the Coupled Chemistry Aerosol-Tracer Transport model

(CCATT) (Longo et al., 2013), allowing for detailed simulation of smoke composition and transport. These developments are being incorporated into the forthcoming BRAMS v6.0.

Financial support

The authors acknowledge the financial support of FCT – Science and Technology Portuguese Foundation, which funded the project FIRESMOKE (http://doi.org/10.54499/PTDC/CTA-MET/3392/2020), through national funds. Thanks, are also due for the financial support given to CESAM by FCT (UID Centro de Estudos do Ambiente e Mar (CESAM) + LA/P/0094/2020), through national funds.

References

Àgueda, A., Pastor, E., Pérez, Y., Planas, E.: Experimental study of the emissivity of flames resulting from the combustion of forest fuels, International Journal of Thermal Sciences, 49(3), 543–554, doi:10.1016/j.ijthermalsci.2009.09.006, 2010.

Ahmadov, R., Grell, G., James, E., Csiszar, I., Tsidulko, M., Pierce, B., McKeen, S., Benjamin, S., Alexander, C., Pereira, G., Freitas, S. and Goldberg, M.: Using VIIRS fire radiative power data to simulate biomass burning emissions, plume rise and smoke transport in a real-time air quality modeling system, International Geoscience and Remote Sensing Symposium (IGARSS), 2017-July, 2806–2808, doi:10.1109/IGARSS.2017.8127581, 2017.

Albini, F. A.: Estimating Wildfire Behavior and Effects, Department of Agriculture, Forest Service, Intermountain Forest and Range Experiment Station., 1976.

Alexander, M. E.: Help with making crown fire hazard assessments, Gen. Tech. Rep. INT-251. Ogden, UT: U.S. Department of Agriculture, Forest Service, Intermountain Forest and Range Experiment Station, 147–156, 1988.

Allen, J.S., Wang, S.Y.S., LaPlante, M.D., Yoon, J. H.: Three Western Pacific Typhoons Strengthened Fire Weather in the Recent Northwest U.S. Conflagration, Geophysical Research Letters, 48(3), 1–11, doi:10.1029/2020GL091430, 2021.

Anderson, K., Chen, J., Englefield, P., Griffin, D., Makar, P. A., Thompson, D.: The Global Forest Fire Emissions Prediction System version 1.0, Geoscientific Model Development, 17(21), 7713–7749, doi:10.5194/gmd-17-7713-2024, 2024.

Anderson, H. E.: Aids to determining fuel models for estimating fire behavior, US Department of Agriculture, Forest Service, Intermountain Forest and Range Experiment Station, 122, 1982.

Andreae, M. O., Gelencsér, A.: Black carbon or brown carbon? the nature of light-absorbing carbonaceous aerosols, Atmospheric Chemistry and Physics, 6(10), 3131–3148, doi:10.5194/acp-6-3131-2006, 2006.

Andreae, M. O., Merlet, P.: [Ca Because of the carbon to permits, , 15(4), 955–966, 2001.

Andreae, M. O. and Rosenfeld, D.: Aerosol-cloud-precipitation interactions. Part 1. The nature and sources of cloud-active aerosols, Earth-Science Reviews, 89(1–2), 13–41, doi:10.1016/j.earscirev.2008.03.001, 2008.

Andrews, P. L., Rothermel, R. C.: Charts for interpreting wildland fire behavior characteristics, Gen. Tech. Rep. INT-131.

Ogden, UT: U.S. Department of Agriculture, Forest Service, Intermountain Forest and Range Experiment Station, 21p, 1982.

Apte, J. S., Brauer, M., Cohen, A. J., Ezzati, M., Pope, C. A.: Ambient PM2.5 Reduces Global and Regional Life Expectancy, Environmental Science and Technology Letters, 5(9), 546–551, doi:10.1021/acs.estlett.8b00360, 2018.

Baughman, R. G., Albini, F. A.: Estimating Midflame Windspeeds. in: Proceedings. Sixth Conference on Fire and Forest Meteorology, Sixth Conference on Fire and Forest Meteorology, Society of Americal Foresters, Washington, DC., 88–92, 1980.

Biscoe, J. ,Warren, B. E.: An X-Ray Study of Carbon Black, Journal of Applied Physics, 13(6), 364–371, 1942.

Bohren, C. F., Huffman, D. R.: Absorption and scattering of light by small particles, John Wiley & Sons, Ltd., 2008.

Bond, T. C., Bergstrom, R. W.: Light absorption by carbonaceous particles: An investigative review, Aerosol Science and Technology, 40(1), 27–67, doi:10.1080/02786820500421521, 2006.

Bond, T. C., Streets, D. G., Yarber, K. F., Nelson, S. M., Woo, J. H., Klimont, Z.: A technology-based global inventory of black and organic carbon emissions from combustion, Journal of Geophysical Research: Atmospheres, 109(14), 1–43, doi:10.1029/2003JD003697, 2004.

Buchard, V., Da Silva, A. M., Colarco, P. R., Darmenov, A., Randles, C. A., Govindaraju, R., Torres, O., Campbell, J., Spurr, R.: Using the OMI aerosol index and absorption aerosol optical depth to evaluate the NASA MERRA Aerosol Reanalysis, Atmospheric Chemistry and Physics, 15(10), 5743–5760, doi:10.5194/acp-15-5743-2015, 2015.

Buchard, V., da Silva, A. M., Randles, C. A., Colarco, P., Ferrare, R., Hair, J., Hostetler, C., Tackett, J., Winker, D.: Evaluation of the surface PM2.5 in Version 1 of the NASA MERRA Aerosol Reanalysis over the United States, Atmospheric Environment, 125, 100–111, doi:10.1016/j.atmosenv.2015.11.004, 2016.

CAMS: Copernicus Atmosphere Monitoring Service., [online] Available from: https://atmosphere.copernicus.eu/, 2015.

Carrico, Chr. M., Petters, M. D., Kreidenweiss, S. M., Collett, J. L., E., Guenter, Malm, W. C.: Aerosol hygroscopicity and cloud droplet activation of extracts of filters from biomass burning experiments, Journal of Geophysical Research Atmospheres, 113(8), 1–9, doi:10.1029/2007JD009274, 2008.

Clark, . L., Jenkins, M. A., Coen, J. L.; Packham, D. R.: A coupled atmosphere-fire model: Role of the convective froude number and dynamic fingering at the fireline, International Journal of Wildland Fire, 6(4), 177–190, doi:10.1071/WF9960177, 1996.

Clark, T.L., Coen, J., Latham, D.: Description of a coupled atmosphere-fire model, International Journal of Wildland Fire, 13, 49–63, doi:https://doi.org/10.1071/WF03043, 2004.

Clinton, N. E., Gong, P., Scott, K.: Quantification of pollutants emitted from very large wildland fires in Southern California, USA, Atmospheric Environment, 40(20), 3686–3695, doi:10.1016/j.atmosenv.2006.02.016, 2006.

Coen, J. L.: Simulation of the Big Elk Fire using coupled atmosphere–fire modeling, International Journal of Wildland Fire, 14, 49–59, doi:https://doi.org/10.1071/WF04047, 2005.

Curci, G., Hogrefe, C., Bianconi, R., Im, U., Balzarini, A., Baró, R., Brunner, D., Forkel, R., Giordano, L., Hirtl, M., Honzak, L., Jiménez-Guerrero, P., Knote, C., Langer, M., Makar, P. A., Pirovano, G., Pérez, J. L., San José, R., Syrakov, D., Tuccella, S.: Uncertainties of simulated aerosol optical properties induced by assumptions on aerosol physical and chemical properties: An AQMEII-2 perspective, Atmospheric Environment, 115, 541–552, doi:10.1016/j.atmosenv.2014.09.009, 2015.

Darmenov, A. S., da Silva, A.: The Quick Fire Emissions Dataset (QFED)—Documentation of versions 2.1, 2.2 and 2.4., NASA//TM-2015-104606, NASA Global Modeling and Assimilation Office, 38, 183 p, 2015.

Engelhart, G. J., Hennigan, C. J., Miracolo, M. A., Robinson, A. L., Pandis, S. N.: Cloud condensation nuclei activity of fresh primary and aged biomass burning aerosol, Atmospheric Chemistry and Physics, 12(15), 7285–7293, doi:10.5194/acp-12-7285-2012, 2012.

ERA5: Fifth generation ECMWF reanalysis for the global climate and weather, [online] Available from: https://www.ecmwf.int/en/forecasts/dataset/ecmwf-reanalysis-v5 (Accessed 5 March 2025), 2019.

Fernandes, A. P., Lopes, D., Sorte, S., Monteiro, A., Gama, C., Reis, J., Menezes, I., Osswald, T., Borrego, C., Almeida, M., Ribeiro, L. M., Viegas, D. X. and Miranda, A. I.: Smoke emissions from the extreme wildfire events in central Portugal in October 2017, International Journal of Wildland Fire, (October 2017), 1–13, doi:10.1071/WF21097, 2022.

Ferrare, R. A., Fraser, R. S., Kaufman, Y. J.: Satellite measurements of large-scale air pollution: Measurements of forest fire smoke., Journal of Geophysical Research: Atmospheres, 95(D7), 9911–9925, 1990.

Filippi, J. B., Pialat, X., Clements, C. B.: Assessment of ForeFire/Meso-NH for wildland fire/atmosphere coupled simulation of the FireFlux experiment, Proceedings of the Combustion Institute, 34(2), 2633–2640, doi:10.1016/j.proci.2012.07.022, 2013.

Forestry Canada Fire Danger Group: Development and structure of the Canadian Forest Fire Behavior Prediction System, Inf. Rep. ST-X-3, 63p, 1992.

Freitas, S. R., Longo, K. M., and Andreae, M. O.: Impact of including the plume rise of vegetation fires in numerical simulations of associated atmospheric pollutants, Geophysical Research Letters, 33, L17808, doi:10.1029/2006GL026608, 2006.

Freitas, S. R., Longo, K. M., Chatfield, R., Latham, D., Silva Dias, M.A.F., Andreae, M. O., Prins, E., Santos, J. C., Gielow, R., and Carvalho Jr., J. A.: Including the sub-grid scale plume rise of vegetation fires in low resolution atmospheric transport models, Atmospheric Chemistry and Physics, 7, 3385–3398, doi:10.5194/acp-7-3385-2007, 2007.

Freitas, S. R., Longo, K. M., Trentmann, J., and Latham, D.: Technical Note: Sensitivity of 1-D smoke plume rise models to the inclusion of environmental wind drag, Atmospheric Chemistry and Physics, 10, 585–594, doi:10.5194/acp-10-585-2010, 2010.

Freitas, S. R., Longo, K. M. and Silva Dias, M. A. F., Chatfield, R., Dias, P. Silva, Artaxo, P., Andreae, M. O., Grell, G., Rodrigues, L. F., Fazenda, A., Panetta, J.: The coupled aerosol and tracer transport model to the Brazilian developments on the regional atmospheric modeling system (CATT-BRAMS)-Part 1: Model description and evaluation, Atmospheric Chemistry and Physics, 9(8), 2843–2861, doi:10.5194/acp-9-2843-2009, 2009.

Freitas, S. R., Panetta, J., Longo, K. M., Rodrigues, L. F., Moreira, D. S., Rosário, N. E., Silva Dias, P. L., Silva Dias, M. A. F., Souza, E. P., Freitas, E .D., Longo, M., Frassoni, A., Fazenda, A. L., Santos e Silva, C. M., Pavani, C. A. B., Eiras, d., D.

A.: The Brazilian developments on the Regional Atmospheric Modeling System (BRAMS 5.2): An integrated environmental model tuned for tropical areas, Geoscientific Model Development, 10, 189–222, doi:10.5194/gmd-10-189-2017, 2017.

Gelaro, R., McCarty, W., Suárez, M. J., Todling, R., Molod, A., Takacs, L., Randles, C. A., Darmenov, A., Bosilovich, M. G., Reichle, R., Wargan, K., Coy, L., Cullather, R., Draper, C., Akella, S., Buchard, V., Conaty, A., da Silva, A. M., Gu, W., Kim, G., R., Merkova, D., Nielsen, J. E., Partyka, G., Pawson, S., Putman, W., Rienecker, M., Schubert, S. D., Sienkiewicz, M. and Zhao, B.: The modern-era retrospective analysis for research and applications, version 2 (MERRA-2), Journal of Climate, 30(14), 5419–5454, doi:10.1175/JCLI-D-16-0758.1, 2017.

Gesch, D. B., Verdin, K. L., Greenlee, S. K.: New land surface digital elevation model covers the earth, EOS Transactions American. Geophysical Union, 80(6), 69–70, doi:10.1029/99EO00050, 1999.

Gevaerd, R., Freitas, S.: Estimativa operacional da umidade do solo para iniciação de modelos de previsão numérica da atmosfera Parte I: Descrição da metodologia e validação, Revista Brasileira de Meteorologia, 21(January), 59–73, 2006.

Hinds, W. C.: Aerosol Technology: Properties, Behavior, and Measurement of Airborne Particles, Wiley-Interscience, New York., 1999.

ICNF: Portuguese National Forest Inventory 6, Statistics and Cartography. Abundance, State and Condition of National Forest Resources [online] Available from: http://www.icnf.pt/portal/florestas/ifn, 2015.

Jaffe, D., Chand, D., Hafner, W., Westerling, A., Spracklen, D.: Influence of fires on O3 concentrations in the western U.S., Environmental Science and Technology, 42(16), 5885–5891, doi:10.1021/es800084k, 2008.

Kirchstetter, Th. W., Novakov, T.: Evidence that the spectral dependence of light absorption by aerosols is affected by organic carbon, Journal of Geophysical Research D: Atmospheres, 109(21), 1–12, doi:10.1029/2004JD004999, 2004.

Kochanski, A. K., Herron-Thorpe, F., Mallia, D. V., Mandel, J., Vaughan, J. K.: Integration of a Coupled Fire-Atmosphere Model Into a Regional Air Quality Forecasting System for Wildfire Events, Frontiers in Forests and Global Change, 4(November), 1–14, doi:10.3389/ffgc.2021.728726, 2021.

Kochanski, A. K., Jenkins, M. A., Yedinak, K., Mandel, J., Beezley, J., Lamb, B.: Toward an integrated system for fire, smoke and air quality simulations., International Journal of Wildland Fire, 25(5), 534–546, 2015.

Lack, D. A., Cappa, C. D.: Impact of brown and clear carbon on light absorption enhancement, single scatter albedo and absorption wavelength dependence of black carbon, Atmospheric Chemistry and Physics, 10(9), 4207–4220, doi:10.5194/acp-10-4207-2010, 2010.

Longo, K. M., Freitas, S. R., Pirre, M., Marécal, V., Rodrigues, L. F., Panetta, J., Alonso, M. F., Rosário, N. E., Moreira, D. S., Gácita, M. S., Arteta, J., Fonseca, R., Stockler, R., Katsurayama, D. M., Fazenda, A. and Bela, M.: The Chemistry CATT-BRAMS model (CCATT-BRAMS 4.5): A regional atmospheric model system for integrated air quality and weather forecasting and research, Geoscientific Model Development, 6(5), 1389–1405, doi:10.5194/gmd-6-1389-2013, 2013.

Longo, K. M., Freitas, S. R. and Andreae, M. O., Setzer, A., Prins, E., Artaxo, P.: The coupled aerosol and tracer transport model to the brazilian developments on the regional atmospheric modeling system (catt-brams)-part 2: Model sensitivity to the biomass burning inventories, Atmospheric Chemistry and Physics, 10(13), 5785–5795, doi:10.5194/acp-10-5785-2010, 2010.

Lopes, D., Menezes, I., Reis, J., Coelho, S., Almeida, S., Borrego, C., Miranda, A. I.: Short-term impacts of extreme wildfire events on human health and visibility, Submitted to Fire journal, 2023.

Lopes, D., Menezes, I. C., Reis, J., Coelho, S., Almeida, M., Viegas, D. X., Borrego, C., Miranda, A. I.: The Short-Term Impacts of the 2017 Portuguese Wildfires on Human Health and Visibility: A Case Study, Fire, 7(10), doi:10.3390/fire7100342, 2024.

Makar, P. A., Akingunola, A., Chen, J., Pabla, B., Gong, W., Stroud, C., Sioris, Ch., Anderson, K., Cheung, Ph., Zhang, J., Milbrandt, J.: Forest-fire aerosol-weather feedbacks over western North America using a high-resolution, online coupled air-quality model, Atmospheric Chemistry and Physics, 21(13), 10557–10587, doi:10.5194/acp-21-10557-2021, 2021.

Mandel, J., Amram, S., Beezley, J.D., Kelman, G., Kochanski, A.K., Kondratenko, V.Y., Lynn, B.H., Regev, B., Vejmelka, M.: Recent advances and applications of WRF–SFIRE, Natural Hazards and Earth System Sciences, 14(10), 2829–2845, doi:10.5194/nhess-14-2829-2014, 2014.

Mandel, J., Beezley, J. D., Coen, J. L., Kim, M.: Data assimilation for wildland fires: Ensemble Kalman filters in coupled atmosphere-surface models, IEEE Control Systems Magazine, (June), 47–65, doi:10.1109/MCS.2009.932224, 2009.

Mandel, J., Beezley, J. D., Kochanski, A. K.: Coupled atmosphere-wildland fire modeling with WRF 3.3 and SFIRE 2011, Geoscientific Model Development, 4(3), 591–610, doi:10.5194/gmd-4-591-2011, 2011.

McArthur, A. G.: Weather and grassland fire behaviour, Leaflet. Forestry Timber Bureau Australia, 100, 23, 1966.

McArthur, A. G.: Fire behaviour in Eucalypt forests, Leaflet. Forestry Timber Bureau Australia, 9th Commonw. For. Conf., New Delhi, 107, 25p, 1967.

Menezes, I. C., Freitas, S. R., Lima, R. S., Fonseca, R. M., Oliveira, V., Braz, R., Dias, S., Surový, P., Ribeiro, N. A.: Application of the coupled brams-sfire atmospheric and fire interactions models to the south of portugal, Revista Brasileira de Meteorologia, 36(3), 423–440, doi:10.1590/0102-77863630101, 2021.

Menezes, I. C., Lopes, D., Fernandes, A. P., Borrego, C., Viegas, D. X., Miranda, A. I.: Atmospheric dynamics and fire-induced phenomena: Insights from a comprehensive analysis of the Sertã wildfire event, Atmospheric Research, 310(April), doi:10.1016/j.atmosres.2024.107649, 2024.

Menezes, I. .: Construção de um Modelo de Interacção Atmosfera/fogo Aplicado à Gestão Florestal e Avaliação de Risco de fogos Florestais no Alentejo., Doctoral Thesis from University of Évora., 2015.

MERRA-2: Global Modeling and Assimilation Office (GMAO), inst3_3d_asm_Cp: MERRA-2 3D IAU State, Meteorology Instantaneous 3-hourly (p-coord, 0.625x0.5L42), version 5.12.4, , doi:10.5067/VJAFPLI1CSIV, 2015.

Miranda, A. I., Martins, V., Cascão, P., Amorim, J. H., Valente, J., Tavares, R., Borrego, C., Tchepel, O., Ferreira, A. J., Cordeiro, C. R., Viegas, D. X., Ribeiro, L. M., Pita, L. P.: Monitoring of firefighters exposure to smoke during fire experiments in Portugal, Environment International, 36(7), 736–745, doi:10.1016/j.envint.2010.05.009, 2010.

Monks, S. A., Arnold, S. R., Chipperfield, M. P.: Evidence for El Niño-Southern Oscillation (ENSO) influence on Arctic CO interannual variability through biomass burning emissions, Geophysical Research Letters, 39(14), 1–6, doi:10.1029/2012GL052512, 2012.

Moreira, D. S., Freitas, S. R., Bonatti, J. P., Mercado, L. M., Rosário, N. M. É., Longo, K. M., Miller, J. B., Gloor, M., Gatti, L. V.: Coupling between the JULES land-surface scheme and the CCATT-BRAMS atmospheric chemistry model (JULES-CCATT-BRAMS1.0): Applications to numerical weather forecasting and the CO2 budget in South America, Geoscientific Model Development, 6, 1243–1259, doi:10.5194/gmd-6-1243-2013, 2013.

Oliveira, E. R., Silva, B. T., Lopes, D., Corticeiro, S., Alves, F. L., Disperati, L., Gama, C.: The Detection of Small-Scale Open-Burning Agriculture Fires Through Remote Sensing, Remote Sensing, 17(1), 1–21, doi:10.3390/rs17010051, 2025.

Osswald, T., Gama, C., Fernandes, A. P., Lopes D., M. A. I.: Effects of the wildfires in August 2021 on the air quality of Athens through a numerical simulation, International Journal of Wildland Fire, (August 2021), 1633–1645, doi:10.1071/WF22148, 2023.

Pereira, G., Longo, K. M., Freitas, S. R., Mataveli, G., Oliveira, V. J., Santos, P. R., Rodrigues, L. F., Cardozo, F. S.: Improving the south America wildfires smoke estimates: Integration of polar-orbiting and geostationary satellite fire products in the Brazilian biomass burning emission model (3BEM), Atmospheric Environment, 273(January), 118954, doi:10.1016/j.atmosenv.2022.118954, 2022.

Pereira, G.: Estimativa e assimilação das emissões de gases traços e aerossóis de queimadas em modelos de química atmosférica., Tese de DoutoradoInstituto Nacional de Pesquisas Espaciais (INPE)., 2013.

Petters, M. D., Kreidenweis, S. M.: A single parameter representation of hygroscopic growth and cloud condensation nucleus activity, Atmospheric Chemistry and Physics, 7, 1061–1971, doi:10.5194/acp-7-1961-2007, 2007.

Procopio, A. S., Remer, L. A., Artaxo, P., Kaufman, Y. J., Holben, B. N.: Modeled spectral optical properties for smoke aerosols in Amazonia, Geophysical Research Letters, 30(24), 1–5, doi:10.1029/2003GL018063, 2003.

Pueschel, R. F., Livingston, J. M., Russell, P. B., Colburn, D. A., Ackerman, T. P., Allen, D. A., Einfeld, W.: Smoke optical depths: Magnitude, variability, and wavelength dependence., Journal of Geophysical Research: Atmospheres, 93(D7), 8388–8402, 1988.

Radmanović, K., Dukić, I., Pervan, S.: Specifični toplinski kapacitet drva, Drvna Industrija, 65(2), 151–157, doi:10.5552/drind.2014.1333, 2014.

Randles, C. A., da Silva, A. M., Buchard, V., Colarco, P. R., Darmenov, A., Govindaraju, R., Smirnov, A., Holben, B., Ferrare, R., Hair, J., Shinozuka, Y., Flynn, C. J.: The MERRA-2 aerosol reanalysis, 1980 onward. Part I: System description and data assimilation evaluation, Journal of Climate, 30(17), 6823–6850, doi:10.1175/JCLI-D-16-0609.1, 2017.

Reid, J. S., Eck, T. F., Christopher, S. A., Hobbs, P. V., Holben, B.: Use of the Ångstrom exponent to estimate the variability of optical and physical properties of aging smoke particles in Brazil, Journal of Geophysical Research Atmospheres, 104(D22), 27473–27489, doi:10.1029/1999JD900833, 1999.

Reid, J. S., Hobbs, P. V.: Physical and optical properties of young smoke from individual biomass fires in Brazil., Journal of Geophysical Research, 103(D24), 32013–32030, 1998.

Reid, J. S., Eck, T. F., Christopher, S. A., Koppman, R., Dubovik, O., Eleuterio, D. P., Holben, B. N., Reid, E. A. and Zhang, J.: A review of biomass burning emissions part II: Intensive optical properties of biomass burning particles, Atmospheric Chemistry and Physics, 5(3), 827–849, doi:10.5194/acp-5-827-2005, 2005.

Relvas, H., Lopes, D., Armengol, J. M.: Empowering communities: Advancements in air quality monitoring and citizen engagement, Urban Climate, 60, doi:10.1016/j.uclim.2025.102344, 2025.

Reynolds, R. W.; Rayner, N. A.; Smith, T. M.; Stokes, D.C.; Wang, W.: An improved in situ and satellite SST analysis for climate, Journal of Climate, 15(13), 1609–1625, doi:10.1175/1520-0442(2002)015<1609:AIISAS>2.0.CO;2, 2002.

Riggan, P. J., Tissell, R. G., Lockwood, R. N., Brass, J. A., Pereira, J. A. R., Miranda, H. S., Miranda, A. C., Campos, T., Higgins, R.: Remote measurement of energy and carbon flux from wildfires in Brazil, Ecological Applications, 14(3), 855–872, doi:10.1890/02-5162, 2004.

Rosário, N. E., Longo, K. M., Toso, P. H., Freitas, S. R., Yamasoe, M. A., Flávio, L., Medeiros, O., Campos Velho, H., Menezes, I. C., Miranda, A. I.: Machine learning-driven characterization and prescription of 1 aerosol optical properties for atmospheric models., Journal of Geoscientific Model Development, 2025.

Rothermel, R. C.: A Mathematical Model for Predicting Fire Spread in Wildland Fuels, US Department of Agriculture, Forest Service, Intermountain Research Station, 115, 1972.

Rothermel, R. C.: Predicting behavior and size of crown fires in the northern Rocky Mountains, USDA Forest Service, Intermountain Research Station, Research Paper, (January), 46, 1991.

Scott, J. H., Burgan, R. E.: comprehensive set of standard fire behavior fuel models for use with Rothermel's surface fire spread model, Gen. Tech. Rep. RMRS-GTR-153. Fort Collins, CO: US Department of Agriculture, Forest Service, Rocky Mountain Research Station, n.d.

Scott, J. H., Reinhardt, E. D.: Assessing crown fire potential by linking models of surface and crown fire behavior., Forest Service, Rocky Mountain Research Station, (September), 2001.

Seinfeld, J. H., Pandis, S. N.: Atmospheric chemistry and physics: from air pollution to climate change, John Wiley & Sons, Ltd., 2016.

Valente, J., Miranda, A. I., Lopes, A. G., Borrego, C., Viegas, D. X., Lopes, M.: Local-scale modelling system to simulate smoke dispersion., International Journal of Wildland Fire, 16, 196–203, 2007.

Van Wagner, C. E.: A spread index for crown fires in spring., Canadian Forest Service, Petawawa Nat. For. Inst, Inf. Rep., 1974.

Van Wagner, C. E.: Conditions for the start and spread of crown fire, Canadian Journal of Forest Research, 7, 23–34, 1977.

Van Wagner, C. E.: Prediction of crown fire behavior in conifer stands., in In: D. C. MacIver, D. C.; Auld, H.; Whitewood, R., eds. Proceedings of the 10th conference of fire and forest meteorology, pp. 207–212., 1989.

Van Wagner, C. E.: Prediction of crown fire behavior in two stands of jack pine, Canadian Journal of Forest Research, (23), 442–449, 1993.

Yamasoe, M. A., Von Randow, C., Manzi, A. O., Schafer, J. S., Eck,, T. F., Holben, B. N.: Effect of smoke and clouds on the transmissivity of photosynthetically active radiation inside the canopy., Atmospheric Chemistry and Physics, 6, 1645–1656, 2006.

Ye, X., Arab, P., Ahmadov, R., James, E., Grell, G. A., Pierce, B., Kumar, A., Makar, P., Chen, J., Davignon, D., Carmichael, G. R., Ferrada, G., Mcqueen, J., Huang, J., Kumar, R., Emmons, L., Herron-Thorpe, F. L., Parrington, M., Engelen, R., Peuch, V. H, D. M. and Saide, P. E.: Evaluation and intercomparison of wildfire smoke forecasts from multiple modeling systems for the 2019 Williams Flats fire, Atmospheric Chemistry and Physics, 21(18), 14427–14469, doi:10.5194/acp-21-14427-2021, 2021.

Yumimoto, K., Tanaka, T. Y., Yoshida, M., Kikuchi, M., Nagao, T. M., Murakami, H., Maki, T.: Assimilation and forecasting experiment for heavy Siberian wildfire smoke in May 2016 with Himawari-8 aerosol optical thickness., Journal of the Meteorological Society of Japan, II, 2018.